Kinetics Analyses of Interactions between Oncogenic and Tumor Suppressor Proteins by Quantitative High Resolution Microscopy Methods

by

SHU-FEN TSENG

Presented to the Faculty of the Graduate School of

The University of Texas at Arlington in Partial Fulfillment

of the Requirements

for the Degree of

DOCTOR OF PHILOSOPHY

THE UNIVERSITY OF TEXAS AT ARLINGTON

May 2013

ACKNOWLEDGEMENTS

First of all, I am heartily thankful for my major advisor, Dr. George Alexandrakis, who constantly provided supervision, guidance, support, and encouragement from the initial to the final step in my dissertation research. Particularly, I would like to thank him for teaching me the research methodology. Under the guidance of his expertise, I not only learned how to do design the experiment but also grasped the spirit of the whole experiment. Again, I am very thankful for his valuable advice. This dissertation would not have been successful without him.

Secondly, I would like to express my sincere gratitude to my co-advisor, Dr. Jer-Tsong Hsieh, for his guidance, caring, patience, and support in this dissertation research. Without his support on this joint-program project, I would never have been able to finish this study. More importantly, his wisdom, humor, and knowledge always inspired and motivated me throughout my doctoral study career.

I am also thankful to have the other three professors Dr. Digant Dave, Dr. Debebrata Saha and Dr. Baohong Yuan as my dissertation committee members. Their support and feedback definitely enhance the rigor of my dissertation research.

In addition, I would like to acknowledge Rey-Chen Pong, who always offered me immense support and encouragement. Also, I would like to thank my colleagues for their significant assistance throughout the whole project. Their company was truly a blessing to me especially during the difficult times in my student life.

Finally, I am indebted to my family, especially my parents, who always gave me the encouragement and love I needed. I could never finish this project and earn this degree without their support.

April 17, 2013

ABSTRACT

Kinetics Analyses of Interactions between Oncogenic and Tumor Suppressor Proteins by Quantitative High Resolution Microscopy Methods

Shu-Fen Tseng, PhD

The University of Texas at Arlington, 2013

Supervising Professor: George Alexandrakis

DAB2IP is correlated to the risk of aggressive prostate cancer and loss of DAB2IP not only leads to epithelial-to-mesenchymal transition (EMT), but also makes cells radioresistant. These observations support the notion that improved knowledge of DAB2IP involvement in cellular pathways could be of help to cancer therapy. The goal of this work was to enable the study of how DAB2IP and some of its known key molecular partners interact in the cell by a combination of molecular biology techniques and recently reported quantitative fluorescence microscopy methods.

The first part of this work was dedicated on investigating the interaction of DAB2IP with the androgen receptor (AR). AR functions as a transcriptional factor, but how DAB2IP influences AR transcriptional activity remains unclear. In this work, the results revealed that AR transcriptional activity can be inhibited by DAB2IP by preventing AR nuclear translocation. Furthermore, AR nucleocytoplasmic kinetics was shown to be associated with the level of

Dihydrotestosterone (DHT) by use of Number & Brightness (N&B) analysis that measures molecular concentration.

The second part of this work was dedicated on investigating changes in the kinetics of the DBA2IP protein after exposure to ionizing irradiation (IR). Whether DAB2IP was involved in DNA repair pathways remains unknown. Our results showed that DAB2IP can repress radiation-induced autophagy to prevent cancer cells from death. DAB2IP in combination with NU7441, a DNA-PKcs inhibitor, was verified to enhance the radiation effect by suppressing autophagy. Furthermore, upon radiation treatment co-localization of DAB2IP and γH2AX, a DSB marker, was not observed. Also, DAB2IP foci in PC-3 and C4-2 D2 cells could not be measured post IR-induction. Although DAB2IP may not directly relocate at DNA DSB sites, post radiation-induction of DAB2IP-EGFP nuclear levels were gradually seen to increase with time.

The last part of this work focused on the development of novel quantitative microscopy method to improve quantification of kinetics of proteins related to DAB2IP. The method relies on the use of photoactivatable GFP (PA-GFP) to enable control of the fluorescent protein concentration in the cell to improve the quantification of molecular diffusion coefficients by Raster Image Correlation Spectroscopy (RICS). The results showed that the accuracy of measuring the PA-GFP diffusion coefficient (23.5 $\mu m^2/s$) was 30% higher than with standard EGFP expression at any time post-transfection. Subsequently, this method was applied to quantifying the kinetics of PA-GFP tagged Skp2, a protein that regulates the degradation of DAB2IP. The free diffusion coefficient of PA-GFP-Skp2 (16.8 $\mu m^2/s$) could be attained at the estimated value, which was 40-60% higher than the value obtained for EGFP-Skp2 at any time post-transfection, because this method could reduce the contaminating contribution from slowly moving or immobile proteins to the RICS data. The combination of quantitative fluorescence microscopy methods with photoactivation could be used in the future play for the improved quantification of the kinetics of other cellular proteins of interest.

TABLE OF CONTENTS

LIST OF ILLUSTRATIONS

CHAPTER 1

INTRODUCTION

Prostate cancer is the second leading cause for mortality in American males (Jemal et al, 2005). The major cause of death is metastatic disease due to the development of castration resistant prostate cancer. DAB2 interacting protein (DAB2IP), a potential prognostic marker, is associated with the risk of aggressive prostate cancer (Chen et al, 2003), and loss of DAB2IP causes epithelial-to-mesenchymal transition (EMT) to drive prostate cancer metastasis and promote tumor growth (Xie et al, 2010). In addition, loss of DAB2IP in prostate cancer cells also leads to resistance to ionizing radiation (IR). However, the current understanding on the functional role of DAB2IP is not completely discovered. The main theme of this thesis was to use a combination of quantitative fluorescence microscopy and traditional molecular biology techniques to help expand the current knowledge on some aspects of DAB2IP function in the cell after radiation exposure and the vital oncogenic proteins associated with DAB2IP. All the relevant microscopy and molecular biology methods used in this work are described in Chapter 2.

Chapter 3 focused on investigating the effect of DAB2IP on the intracellular kinetics of the androgen receptor (AR), a key oncogenic protein that associates with DAB2IP. Both development of the prostate gland and prostate cancer growth are associated with AR and its signaling (Chen et al, 2008). In contrast to the expression of DAB2IP that decreases in aggressive prostate cancer, overexpression of AR and increased intracellular activity are observed in castration resistant prostate cancer (Dehm et al, 2008; Edwards et al, 2003). Whether the function of DAB2IP is involved in AR signaling has attracted a lot of attention. In this work, immunofluorescence and Number and Brightness (N&B) analysis, a quantitative

fluorescence microscopy method (Digman et al, 2008), were performed to investigate the relationship between AR and DAB2IP and AR nucleocytoplasmic kinetics, respectively.

Chapter 4 was dedicated on exploring the possible role of DAB2IP on the repair of DNA double strand breaks (DSBs) after IR exposure. These studies were motivated by reports that loss of DAB2IP can cause prostate cancer cells to be more radioresistant, whereas prostate cancer cells expressing DAB2IP become radiosensitive due to slower DNA DSB repair kinetics (Kong et al, 2010b). However, whether DAB2IP was involved in DNA repair pathways remains unknown. This work investigated if there were any changes in the cytoplasmic versus the nuclear concentrations of DAB2IP as a function of time post IR-induction. The possible co-localization of DAB2IP with γH2X, a DSB marker, was also investigated. The expectation was that if these studies would yield positive results they would indicate the mechanism for the involvement of DAB2IP in DSB repair.

While Chapters 3 and 4 were focused on the study of biological mechanisms of proteins involved in prostate cancer, Chapter 5 was focused on the development of a novel quantitative fluorescence microscopy approach for the improved quantification of the cellular kinetics of such proteins. Specifically, a photoactivation approach was developed to control the fluorescent molecule concentration in the cell, which in turn was shown to improve the accuracy of the diffusion coefficient of these proteins as measured by Raster Image Correlation spectroscopy (RICS). After this newly developed technique was validated by expressing photoactivatable GFP (PA-GFP) in cells, the method was tested on prostate cancer relevant proteins that were fluorescently tagged with PA-GFP. Unfortunately, initial experiments on a PAGFP-DAB2IP protein were not successful in determining the diffusion of DAB2IP in the cell as most of the fluorescent protein may be immobile. Subsequent experiments were focused on the kinetics of PA-GFP tagged S-phase kinase-associated protein 2 (Skp2), a E3 ubiquitin ligase, that can modulate cell cycle progression by ubiquitin-mediated degradation (Carrano et al, 1999). Elevated expression of Skp2 is correlated with tumor grade (Yang et al, 2002) and conversely

loss of DAB2IP is correlated with tumor grade (Min et al, 2010). In addition, DAB2IP can be down-regulated by Skp2-mediated ubiquitin degradation according to Dr. Hsieh's unpublished results. In this work, the use of PA-GFP as a tool to tune the photoactivated fluorophore concentration was successfully used to improve the accuracy of the measured diffusion coefficient of Skp2. The developed method can potentially be applied to any other protein of interest that has a freely diffusing population fraction in the cell.

Finally, in the Conclusions section the salient findings of this work as well as the unsuccessful studies performed in this work are discussed and future experiments to improve on the latter are proposed.

1.1 Oncogenic and Tumor Suppressor Proteins

1.1.1 The Functional Role of DAB2IP

Prostate cancer is the most prevalent non-cutaneous diagnosed cancer in American males, second only to lung cancer in the causes of cancer mortality (Jemal et al, 2005; Siegel et al, 2011). Radical prostatectomy and radiation are the main forms of therapy for localized and low stage tumors (Capasso, 2005). However, prostate tumors recur in 20 to 40 % of patients after radical prostatectomy. Androgen deprivation therapy (ADT) is a standard treatment method for patients with high stage tumors (≥T3). Unfortunately, malignancies in these patients will eventually cease responding to ADT and develop into a more aggressive and lethal castration resistant prostate cancer. The major mortal cause of castration resistant prostate cancer is metastasis-related disease (Sadar, 2011). The mechanisms that drive metastasis and progression are poorly understood. However, growing evidence suggests that EMT should be associated with cancer metastasis and therapeutic resistance (Baritaki et al, 2009).

DAB2IP, a member of the RAS-GTPase activating protein family, is a protein that has been associated with EMT and treatment resistant prostate cancer. DAB2IP expression is

suppressed by aberrant methylation, which has been shown to be associated with prostate, breast, lung, and gastrointestinal tumors (Chen et al, 2005; Dote et al, 2005; Dote et al, 2004; Yano et al, 2005). Decreased DAB2IP expression has been observed in the majority of prostatic intraepithelial neoplasia (PIN) and adenocarcinomas and its expression is inversely correlated with Gleason grade (Min et al, 2010). Moreover, loss of DAB2IP leads to EMT transition, which results in down-regulation of epithelial marker, E-cadherin, and up-regulation of the mesenchymal marker vimentin, which promote tumor growth *in vivo* (Xie et al, 2010).

This latter finding by Xie et al. shows that DAB2IP can modulate the switch between β-catenin's transcriptional and adhesive functions and subsequently regulate EMT. Except for the enhancement of the cell-cell adhesion in adherent junctions of the cell membrane, β-catenin functions as a transcriptional co-activator by associating with T-cell factor/lymphoid enhancer factor (TCF/LEF) transcription-factor complexes, and consequently induces the expression of Slug or Twist, both transcription factors and oncogenic EMT inducers, which repress E-cadherin expression (Bolos et al, 2003; Yang et al, 2004) and contribute to EMT (Eger et al, 2000; Thuault et al, 2008). Therefore, nuclear β-catenin/TCF transcriptional activity is crucial for the induction of target genes associated with EMT. Also, DAB2IP can modulate cell survival and apoptosis via phosphatidylinositide 3-kinases (PI3K)-Akt signaling. Thus, the loss of DAB2IP results in the transcriptional reprogramming of abnormal survival signals and further induces EMT (Xie et al, 2009). Deep understanding of the function of DAB2IP and the relationship between DAB2IP and oncogenic proteins in the lethal form of this disease will provide therapeutic potential and biomarkers for the prevention of castration resistant prostate cancer.

1.1.2 The function of AR and Relationship between AR and DAB2IP

AR, a nuclear hormone receptor, plays a critical role for the development of either male reproductive organs or prostate cancer (Brinkmann & Trapman, 2000; Cunha & Young, 1991; Donjacour & Cunha, 1993). The main function of AR is as a ligand-dependent transcription

factor that regulates the expression of target genes associated with cell proliferation, cell survival, and differentiated cell function (Mooradian et al, 1987). Once AR is bound to androgen, AR is dissociated from heat shock proteins as a result of a conformational change, and then AR dimers translocate from the cytoplasm to the nucleus in order to bind the androgen response elements (ARE) (Heemers & Tindall, 2007).

Therefore, ADT becomes the main treatment of prostate cancer. Most patients will respond to this therapy, that initially reduces circulating prostate specific antigen (PSA) and tumor burden (Seruga & Tannock, 2008). However, patients eventually develop androgen-insensitive prostate tumors after global androgen suppression and cease to respond to the androgen deprivation treatment if receiving continuous ADT. In contrast, several studies show that intermittent ADT can postpone the time to develop CRPC, and also reduce the risk of side effects associated with continuous ADT (Akakura et al, 1993; Saigal et al, 2007; Thompson et al, 2003).

Importantly, much evidence shows that the expression of AR is commonly elevated in castration resistant prostate cancer (Bubendorf et al, 1999; de Vere White et al, 1997; Edwards et al, 2003; Ford et al, 2003; Koivisto et al, 1997; Lapointe et al, 2004; Linja et al, 2001; Yu et al, 2004), and the transcriptional activities of AR also increase in 80% of castration resistant prostate cancer cases. The increased AR activity results from constitutively active AR splice variants in castration resistant prostate cancer (Dehm et al, 2008; Hu et al, 2009), the gain-of-function mutations of AR in 10-30% of tumors such as increased AR sensitivity to androgen (Gregory et al, 2001), and AR activation through crosstalk with other signaling pathways (Wen et al, 2000). Another molecular mechanism for increased AR activity is the expression of androgen synthetic enzymes up-regulated by tumor tissue (Locke et al, 2008; Stanbrough et al, 2006). These observations suggest that the development of castration resistant prostate cancer is highly correlative with genetic modification in order to compensate for low levels of androgen.

Specifically, one of the mechanisms for AR signaling activity is that AR can become an androgen-independent receptor activated by PI3K-Akt signaling (Wang et al, 2007). In the absence of androgen, Akt, activated by HER-2/neu signaling though PI3K can phosphorylate AR at serine 213 and 791, resulting in nuclear translocation of AR in order to induce AR target genes (Wang et al, 2007; Wen et al, 2000). In contrast, DAB2IP is able to negatively regulate PI3K-Akt signaling via its individual binding domain in order to modulate cell apoptosis and proliferation. In addition, recent research shows that the expression of EZH2, a histone methyltransferase, is frequently elevated in castration resistant prostate cancer and can be negatively regulated through AR when androgen is induced in hormone-refractory cell lines (Bohrer et al, 2010). Consequently, androgen-induced inhibition of EZH2 expression results in the increased expression of its target genes, such as DAB2IP and E-cadherin in hormone-refractory cell lines (Bohrer et al, 2010). Considering the conceptual association between AR and DAB2IP, the AR activity is highly related to DAB2IP in castration resistant prostate cancer cases. Moreover, these two proteins can serve as unique biomarkers or potential targets for treatment in the development of castration resistant prostate cancer. However, the impact of the interaction between DAB2IP and AR in the development of castration resistant prostate cancer has not yet been carefully examined. To further investigate this interaction, quantitative fluorescence microscopy combined with molecular biology methods were used in this study.

1.1.3 Radiation Therapy Combined with Targeted Genetic Therapy of DAB2IP

Although ADT which mainly modulates AR signaling activity is the standard therapy for advanced prostate tumors with >T3 stage, most patients undergoing therapy eventually develop lethal androgen resistant prostate cancer. In medical application of treatments, radiation therapy also plays an important role as a treatment modality of advanced prostate cancer with T1-T3 stage, in addition to androgen depletion therapy (Kaprealian et al, 2012; Schmitz et al, 2010). However, the appropriate dose of radiation, limited to < 80 Gy because of the increased risk of

toxicity, commonly results in either radiation resistant prostate cancers after treatment or radio-recurrent prostate cancer repopulating the irradiated site. Specifically, patients undergoing long-term hormone therapy could have higher biochemical failure rates after radiation treatment (Wu et al, 2007). In addition, clinical evidence shows that less than 80% of patients have distant metastasis-free 5 year survival after radiation therapy (Pollack et al, 2000; Pollack et al, 2002; Rosen et al, 1999). Compared with radiotherapy alone, clinical observations reveal that radiation therapy in combination with androgen depletion therapy, immunotherapy or gene therapy could exert enhanced antitumor activity and enhanced efficacy of therapies for preventing treatment failure (D'Amico, 2002; Finkelstein & Fishman, 2012; Freytag et al, 2003; Lee, 2006). Moreover, abnormalities of several genes, such as p53, Bcl-2, PTEN and DAB2IP, are highly correlated with radiation-resistant prostate cancer (Cowen et al, 2000; Kong et al, 2010b; Scherr et al, 1999; Tomioka et al, 2008), and therefore can be potential target genes for a combination therapy with radiation.

Most importantly, previous observation reveals that loss of DAB2IP frequently occurs in advanced prostate cancer, and enhances the resistance of prostate cancer cells to ionizing radiation (IR) because of faster DNA double strand break (DSB) repair kinetics, robust G_2-M checkpoint control and reduction of IR-induced apoptosis (Kong et al, 2010b). The co-localization of histone 2A family member X (H2AX) phosphorylatiion and tumor suppressor p53-binding protein 1 (53BP1), which function as a scaffold for recruiting DNA repair proteins (DiTullio et al, 2002; Fernandez-Capetillo et al, 2002; Markova et al, 2007), occurs at sites of DNA DSBs upon IR-induction. Fluorescently tagged forms of these proteins are typically used as indicators of DNA DSB repair kinetics as they both accumulate in high numbers at DSBs to form foci, or ‘hot spots’, that are easily discernible in microscopy images (Schultz et al, 2000). The finding in Kong et al. (2010) reveals that the DSB repair rate in DAB2IP-deficient cells is significantly faster than in control cells according to the number of remaining co-localized foci formed by γH2AX and 53BP1 post IR-induction. Also, a robust G_2-M checkpoint in DAB2IP-

deficient cells post IR induction is determined using histone H3 phosphorylation staining by flow cytometric analysis. Then, DAB2IP-deficient cells undergoing apoptosis at 48 hours post IR induction are detected by using Annexin V/7-AAD staining (Kong et al, 2010b). In addition, DAB2IP can modulate cell survival, apoptosis and proliferation by coordinating the PI3K-Akt pathway and loss of DAB2IP expression in prostate cancer cells can cause resistance to stress-induced apoptosis (Xie et al, 2009). According to these observations, we speculate that DAB2IP can be a possible prognostic marker to improve tumor cure and control in selecting patients with IR resistant prostate cancer. Furthermore a potential peptide therapy of DAB2IP in combination with radiotherapy could be developed to enhance the radiation-sensitizing effect in advanced prostate cancer However, the mechanism by which DAB2IP-deficient prostate cancer cells become radiation resistant remains poorly understood. To interrogate this mechanism, further experiments are needed to elucidate the functional role and kinetics of DAB2IP after radiation treatment.

1.1.4 The Function of Skp2 and Relationship between Skp2 and DAB2IP

Skp2, a member of the F-box protein family, constitutes one of the four subunits of the ubiquitin ligase complex (Skp1-Cullin1-F-box). Skp2 has been reported to regulate cell proliferation and cell cycle progression by ubiquitin-mediated degradation of its substrates, such as p27 and p21 (Carrano et al, 1999; Yu et al, 1998). Previous studies show that p27 degradation is regulated by Skp2-mediated nuclear ubiquitination (Lee & Kay, 2008), and Skp2-mediated ubiquitinating Nijmegen breakage syndrome (NBS1) is required for ATM recruitment to the DNA foci upon DSBs (Wu et al, 2012). Moreover, a recent study shows that development of prostate cancer is restricted by triggering cellular senescence due to the increase of p21 and p27 expression in Skp2 deficient cells (Lin et al, 2010). The increased expression of Skp2 has been detected in prostate cancer tissues, and an increase in its expression is correlated with higher tumor stage, grade and recurrence after radical prostatectomy (Yang et al, 2002). The

observations mentioned above suggest that the DAB2IP expression levels trend in the opposite direction relative to Skp2 ones in prostate cancer *in vivo.* DAB2IP contains several potential functional domains, including PH, C2, GAP, PER, LZ and PR domains (Xie et al, 2009). Previous study reports that the PR domain of DAB2IP can bind to PI3K and further inactivate Akt, a regulatory protein that controls cell growth and apoptosis (Xie et al, 2009). Interestingly, a previous study shows that the decrease in the phosphorylation of Akt1 can result in the down-regulation of Skp2 (van Duijn & Trapman, 2006), because phosphorylation of Skp2 at Ser-72 by activated Akt1 weakens APC-Cdh1-mediated degradation of Skp2 and leads to Skp2 cytoplasmic translocation (Gao et al, 2009). Furthermore, the C2 domain of DAB2IP is capable of binding to protein phosphatase 2 (PP2A) which can regulate β-catenin phosphorylation and degradation (Zhang et al, 2009), and glycogen synthase kinase 3 beta (GSK-3β), which can regulate β-catenin degradation (Akiyama, 2000), and further form a complex, leading to the inhibition of nuclear β-catenin/TCF transcriptional activity (Xie et al, 2010). In contrast, β-catenin or TCF can bind to a Skp2 promoter sequence causing the up-regulation of Skp2 (Tang et al, 2009). Considering these observations, we speculate that DAB2IP could suppress the expression of Skp2 via PI3K-Akt activity signaling or β-catenin/TCF activity signaling.

On the other hand, Skp2 can degrade DAB2IP through an ubiquitin-proteasome mechanism according to Dr. Hsieh's unpublished results. Skp2 can interact with DAB2IP to form a complex defined by co-immunoprecipitation (Co-IP), in which an antibody against a specific protein of interest is used to precipitate protein complexes formed by the protein in cell lysate. Taken together, these findings suggest that the reciprocally causal relationship between Skp2 and DAB2IP could possibly exist in prostate cancer cells. Most importantly, abnormal expressions of Skp2 (Yang et al, 2002) and DAB2IP (Chen et al, 2003) frequently occur at the development of aggressive prostate cancer, and these two proteins could be used as either prognostic biomarkers for the personalized treatment of prostate cancer, or as therapeutic targets to enhance treatment effects. Therefore, these observations strongly suggest that deep

understanding of the functional role of Skp2 and its signaling activity in either DAB2IP-deficient prostate cancer cells or even control cells could help improve the treatment of advanced prostate cancer.

1.2 Quantitative High Resolution Microscopy Methods Applied to Living Cells

1.2.1 Fluorescent Probes for Studying Protein Dynamics in Living Cells

In recent decades, fluorescence microcopy has been widely used in biochemistry and biophysics, and fluorescent proteins have been used as tags to enable the study of the structure and function of live cell systems in a broad range of applications. Moreover, the development of new fluorescent probes and the constant development of new equipment drive a rapid evolution in fluorescence microscopy methodologies. A growing body of literature about fluorescence microscopy strongly suggests that deep understanding of the photophysical properties of fluorescent proteins and of fluorescence microscopy instrumentation is a prerequisite for the further development of methods that are of value to biologists and clinicians.

1.2.1.1 The Florescence Principle

Fluorescence originates from a molecule that absorbs excitation light and re-emits a portion of the absorbed radiant energy as light at a longer wavelength. This phenomenon is named Stokes shift, which was first observed by Sir. George Gabriel Stokes at the University of Cambridge in 1852. Another useful approach, Jablonski diagrams named after Professor Alexander Jablonski, is used to depict the processes occurring between the emission and excitation (Fig.1.1) (Lichtman & Conchello, 2005). Light emission typically results from the electronic transition from an excited singlet state to the ground state. The typical emission rate of fluorescence is in the neighborhood of nanoseconds (ns) with typical fluorescence lifetime in the 1-10 ns range.

In Fig. 1, S_0, S_1, and S_2 belong to a singlet state and T_1 belongs to a triplet state. Singlet state means that a pair of electrons with opposite spins resides in a single electronic orbital.

Triplet state means that a pair of electrons can occupy two separate electronic orbitals with spins parallel to each other as this is allowed by Pauli's exclusion principle. S_1 and S_2 are excited states where the energy in the excited state S_2 is higher than that in excited state S_1. After a fluorescent molecule is excited, an electron will transit from the ground state to either excited state S_1 or excited state S_2 and the electron will most rapidly relax to the lowest excited state S_1. This process is called internal conversion and results in partial loss of the absorbed light energy as heat to the environment. Subsequently, the electron returns to ground state and at the same time a fluorescence photon is emitted. The partial energy loss is the reason why the emitted fluorescence photon has a longer wavelength than the absorbed one. Additionally, intersystem crossing can also occur occasionally through a non-radiative transition. During intersystem crossing, electrons in excited state S_1 undergo a spin conversion to the first triplet state T_1. However, the descent from T1 to the ground state is a forbidden transition and the emission rate is very low (to -) compared to fluorescence. The longer lifetime emission of light from T_1 to S_0 is known as phosphorescence.

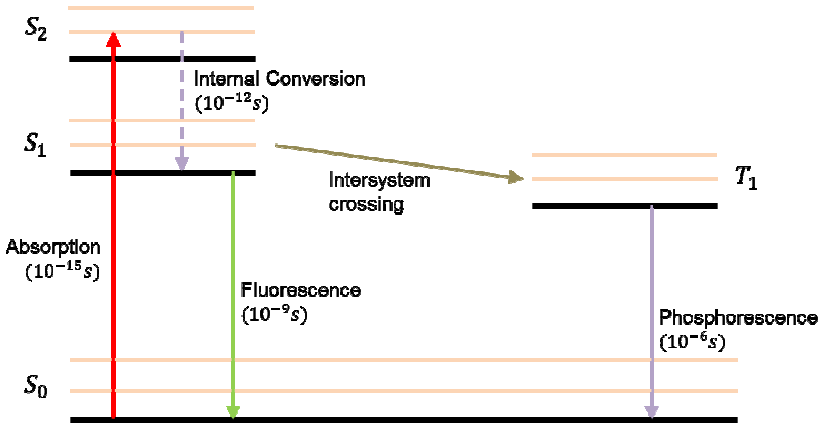

Figure 1.1 Jablonski diagram

1.2.1.2 Optimal Florescent Protein Selection for Microscopy Applications

Typically, the characterization of the best available fluorescent proteins is determined by six factors: Efficiency of maturation, brightness, sufficient photostability, monomeric fusion

tag, less environmental sensitivity, and minimal crosstalk between excitation and emission (Shaner et al, 2005). The detected brightness of fluorescent proteins is dependent on both their intrinsic brightness and the properties of the optical setup. The intrinsic brightness of proteins depends on their quantum yield, extinction coefficient and maturation efficiency. These properties cannot be changed, and therefore the selection of the fluorescent protein indicator for an experiment should be performed before genetically tagging it to a protein of interest (Chudakov et al, 2010; Shaner et al, 2005). Importantly, a comparison of brightness among fluorescent proteins from different literature reports should take into consideration any differences between optical setups, including excitation intensity, excitation wavelength, dichroic mirrors and emission filters, and light detectors used.

Photostability is a critical parameter for quantitative fluorescence microscopy. However, it is very difficult to directly compare the reported photostability between fluorescent proteins used in different studies because there are details such, as the cellular environment that may be different in each study. To determine photostability in practice, cells expressing fluorescent proteins are photobleached with continuous illumination and continuous images are recorded to provide a photobleaching intensity curve.

Maintaining protein function after fluorescent tagging is also a critical consideration. Specifically, many fluorescent proteins are inherently dimeric or tetrameric, which could cause aggregation of proteins inside cells and affect the localization of proteins of interest after tagging.

Finally, to investigate the interaction of proteins, the crosstalk in emission spectra between fluorescent proteins is a main concern. The crosstalk in the emission spectra can be reduced by using a proper optical setup, which would include appropriate emission filter and dichroic mirror selections.

In addition to selecting fluorescent proteins with optimal photophysical properties for a specific microscopy application, researchers now also have the capacity to use fluorescent proteins that can be turned on from a dark initial state. Such proteins have found use in super-

resolution microscopy (Bates et al, 2008), and of more interest to this work, have been used as a means of controlling fluorescent molecule concentration (Hess et al, 2006). Among the currently available photoactivatable protein variants, the photoactivatable green fluorescent protein (PA-GFP), a GFP variant, has attracted a lot of attention (Annibale et al, 2011; Bates et al, 2008; Hess et al, 2006; Runions et al, 2006). PA-GFP can be turned onto a fluorescent state by UV-blue light and then excited for fluorescence emission at 488 nm, which is the same as GFP. The original wild type GFP (WT-GFP) has a major absorbance peak at 375 nm and a minor absorbance peak at 488 nm (Patterson & Lippincott-Schwartz, 2004). Replacing threonine at position 203 in the amino-acid chain of WT-GFP with histidine gives rise to a variant, photoactivatable form of GFP, called the PA-GFP with a single absorbance peak at 397 nm (Patterson & Lippincott-Schwartz, 2002). Upon illumination of the protein with 405 nm light, the absorbance peak of PA-GFP irreversibly switches from 397 nm to 488 nm so that the fluorescence at 488 nm excitation dramatically increases after photoactivation (Henderson et al, 2009) as shown in Fig. 1.2. Therefore, the concentration of proteins tagged with PA-GFP becomes adjustable to yield higher signal amplitudes and better signal-to-noise (Vorvis et al, 2008). In this work, the control of fluorescent molecule concentration has been studied as a possible means of improving the quantification of molecular kinetics.

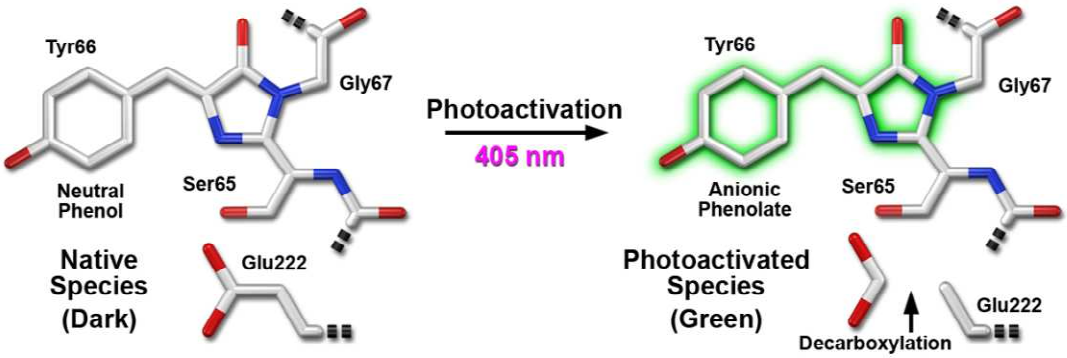

Figure 1.2 Mechanism of photoactivation fluorescent protein (Shaner et al, 2007)

1.2.2 High Spatial Resolution Fluorescence Microscopy Methods

1.2.2.1 Confocal Microscopy

A typical high spatial resolution fluorescence microscopy setup contains an inverted microscope, excitation lasers, a high numerical aperture (NA) (>1) objective lens, appropriate dichroic mirrors, emission filters and light detectors. Of important role to the spatial resolution of measurements is to have the smallest possible diffraction limited spot, created by overfilling of the back aperture of the objective using a beam expander. A higher NA objective also helps increase the spatial resolution and improve excitation and collection efficiency. To improve sensitivity of signal collection versus reducing sources of background signal, an anti-reflection coating is used as part of the objective design to reduce signal loses due to reflection as well as reduce the background from the back-scattered light. Sensitivity of signal collection is also affected by appropriate choice of dichroic mirror and emission filters to be placed in front of the detectors. Photon counting mode light detectors, such as avalanche photodiodes (APD), or sensitive low-noise photomultipliers (PMTs) need to be used to provide better rejection of noise. Finally, an x-y galvanometer-driven scanner provides the focal-point positioning during raster scanning the excitation beam to form a pixel-by-pixel fluorescence image. Confocal microscopy is used to improve the resolution and contrast of fluorescence images by elimination of unwanted light using a pinhole in front of the detector (Stephens & Allan, 2003). The first commercial confocal microscopy system was built in the early 1990s. To avoid the out-of-focus fluorescence reaching the detector, a pinhole is designed to have a size that is approximately the diameter of the diffraction-limited spot, after taking into account the magnification of all collecting optics in the fluorescence path. Additionally, the size of pinhole is used to determine the thickness of optical sectioning, limited by the axial length of point spread function (PSF). For a small pinhole, the PSF is assumed to approximate a 3D Gaussian profile at the focus, which can be mathematically expressed as follows (Chen et al, 1999):

$$I(x,y,z) = \exp\left[\frac{-2(x^2+y^2)}{\omega_0^2} - \frac{-2z^2}{\omega_z^2}\right] \quad (1)$$

, where ω_0^2 and ω_z^2 are the $1/e^2$ radial and axial radii of the beam waist.

1.2.2.2 Two-Photon Microscopy

In contrast to confocal microscopy, two-photon microscopy provides larger depth penetration and confocal axial resolution without a pinhole due to the inherent optical sectioning nature of the excitation process (Fitzpatrick & Lillemeier, 2011) as shown as in Fig. 4. Maria Goeppert-Mayer predicted in her doctoral dissertation that a multiphoton excitation processes could exist by which a fluorophore could be excited by multiple photons of lower energy adding up coherently, rather than by one photon of higher energy (So et al, 2000). Experimental verification of a two-photon excitation process first came from Kaiser and Garret (Kaier W, 1961). The two-photon excitation process occurs on a fluorophore that simultaneously absorbs two photons, each with one-half of the excitation energy as that used for one photon excitation. Two-photon excitation is a nonlinear process and the emission of a fluorophore is proportional to the quadratic excitation power. In addition, this process can only be achieved by using high power pulsed lasers, such as Ti:Sapphire laser, which can provide extremely high light intensity over very short (femtosecond) time intervals. The two-photon excitation application in the biological sciences combined with laser scanning microscopy was first published by Denk et al. in 1990 (Denk et al, 1990). Most importantly, the probability of simultaneous absorption of two photons outside of the focal plane is significantly lower than that at the focal plane (Fig. 1.3). Therefore, two-photon microscopy naturally creates the property of optical sectioning and also reduces the photodamage and photobleaching occurring outside of the focal plane. In cellular applications, two-photon microscopy is more suitable due to the reduction of photodamage and photobleaching. However, it is not prevailing because of its high cost and maintenance requirements.

An important parameter for efficient fluorescence excitation in two-photon microscopy is the two-photon absorption cross-section of the fluorophore, which indicates the probability of the simultaneous absorption of two photons (Drobizhev et al, 2011). Two-photon absorption cross-sections are typically in the order of 10^{-50} (m^4 s), and therefore a short-pulse lasers is required to produce the high light fluxes needed for efficient two-photon excitation (Diaspro et al, 2005). The unit of two-photon absorption cross-section is called as Goeppert-Mayer, and 1 GM is equal to 10^{-50} (m^4 s/photon) (Drobizhev et al, 2011). Importantly, for minimizing the effect of thermal damage inside the cells a fluorophore with high value of two-photon absorption cross-section is required due to the high ratio of the energy absorbed to the input energy (Albota et al, 1998). The spectra for two-photon absorption cross-sections cannot be directly predicted from the corresponding one-photon absorption cross-sections (Diaspro et al, 2005). There are typically two peaks in two-photon absorption cross-section spectra. One peak of the two-photon absorption cross-section occurs at the wavelength around twice that need for one-photon absorption, and another one occurs at much shorter than that needed for one-photon absorption, where the one-photon absorption cross-section is comparatively weak. Most importantly, the two-photon absorption spectra typically span the near-infrared wavelength range, which is distant enough to facilitate spectral separation from the fluorophore emission spectra as well as from any autofluorescence background. A short-pass dichroic mirror in combination with a band-pass emission filter can easily filter out the excitation light and Raman scattering, and also minimize the loss of emission intensity (So et al, 2000). In contrast, one-photon excitation spectra are much closer to their emission spectra and a dichroic mirror with long-pass and a band-pass emission filter could be used to filter out excitation light at the cost of also eliminating a fraction of the emission light. Furthermore, for a thick specimen the fluorescence photon trajectories can be changed by multiple scattering Signal attenuation from thick tissues is a bigger problem for confocal microscopy as the emission pinhole used to reject the out-of-focus light will also reject a lot of the scattered light that nevertheless had originated from the focal

volume. Conversely, fluorescence signal loss is minimized in two-photon microscopy due to natural property of optical sectioning that obviates the need for a pinhole thus enabling improved collection of scattered light. In addition, the excitation volume is approximated assumed by a Guassian-Lorentzian shape, which can be mathematically expression as follows (Chen et al, 1999):

$$I(x,y,z)=\frac{\omega_0^2}{\omega(z)^2}\exp\left[\frac{-2(x^2+y^2)}{\omega(z)^2}\right] \quad (2)$$

$$\omega(z)^2=\omega_0^2\left[1+\left(\frac{z}{\left(\frac{\pi\omega_0^2}{\lambda}\right)}\right)^2\right] \quad (3)$$

,where ω_0^2 is the radial e^{-1} value of the beam waist, and λ is the excitation wavelength.

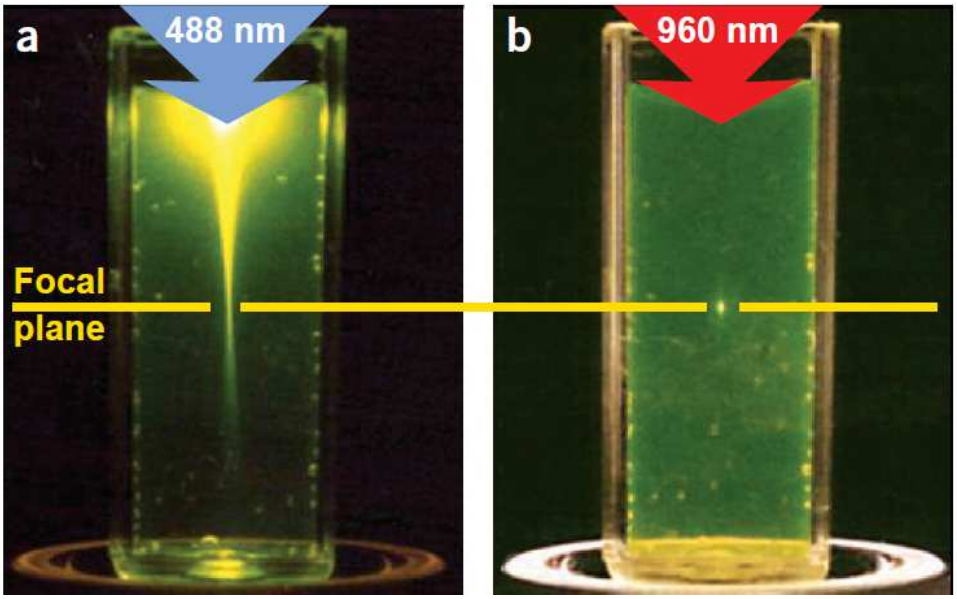

Figure 1.3 The location of fluorescence excitation volume created by (a) one-photon excitation, and (b) two-photon excitation (Zipfel et al, 2003)

1.2.3 Fluorescence Correlation Spectroscopy (FCS)

Fluorescence Correlation Spectroscopy (FCS) is a technique that provides information on protein concentration, dynamics and protein interactions under real-time conditions (Rossow et al, 2010). The diffusion of fluorescently tagged proteins through the defined illumination volume results in fluorescent fluctuations, which are detected and recorded within 10-50 second intervals. The recorded time-series are then processed by the autocorrelation function G(τ):

$$G(\tau)=\frac{<\delta F(t)\delta F(t+\tau)>}{<F(t)>^2} \quad (4)$$

, where F(t) is the intensity of fluorescence measured at time t, < F(t) > is the average fluorescence intensity, and δF(t) is the difference between the two (δF(t)=F(t)-<F(t)>). F(t+τ) is the fluorescence intensity measured at time t+τ, where τ is a delayed time point. The fluorescence intensity is proportional to brightness, detector efficiency, excitation intensity and molecular concentration (Palmer & Thompson, 1987), as shown in Eq. 5:.

$$\delta F(t)=F(t)-<F(t)>=B_r \int CEF(r)I^2(r)\delta C(r,t)dV \quad (5)$$

In Eq. 5 the fluctuation of fluorescence intensity is proportional to four parameters which are brightness of fluorescence B_r, the function of collection efficiency equipment CEF(r), excitation intensity I(r) and local concentration at time t, δC(r,t). In addition, two-photon excitation is a nonlinear absorption process that is the simultaneous absorption of two photons; therefore the fluorescence intensity is proportional to the square of excitation intensity I(r). Furthermore, the fluctuation δC(r,t) depends on the biophysical model describing the underlying kinetics. The simplest and most popular model assumed is that of pure diffusion for a single molecular species (Magde et al, 1974). The resulting solution to the diffusion equation for δC(r,t) results in the autocorrelation function described in Eq. 6 (Haustein & Schwille, 2003).

$$G(\tau)=G(0)\left(1+\frac{\tau}{\tau_d}\right)^{-1}\left(1+\frac{K^2\tau}{\tau_d}\right)^{-1/2} \quad (6)$$

, where τ_d is the characteristic diffusion time ($\tau_d = \frac{\omega_r^2}{4D}$), K is dimension ratio of the confocal volume principal axes ($K^2 = \frac{\omega_r}{\omega_z}$), r_0 is the radial dimension; z_0 is the axial dimension, and D is the molecular diffusion coefficient. The characteristic diffusion time can be calculated by $\tau_d = \frac{\omega_r^2}{4D}$ when using one photon excitation, and $\tau_d = \frac{\omega_r^2}{8D}$ when using two-photon excitation according to the corresponding shape of the illumination volume. The experimentally derived correlation curves are then fitted to Eq. 6 above by the Levenberg–Marquadt non-linear least squares algorithm where D and N are the fitting parameters (Fitzpatrick & Lillemeier, 2011). As the FCS signal amplitude, G(0), is proportional to 1/N, lower fluorophore concentrations lead to higher signal amplitudes. In this work we devised a strategy in which photoactivatable green fluorescence protein (PA-GFP) was used, alone or fused to the proteins of interest, to control the signal amplitude in FCS, as well as the signal amplitude in related quantitative fluorescence microscopy methods described further below, which we show leads to more accurate quantification of D.

In live cell experiments a fraction of the fluorescently tagged protein interacts with other proteins or cellular structures and is therefore of lower mobility. Though there have been attempts to infer the detailed binding-unbinding dynamics of proteins by FCS (Roche et al, 2008) most of these studies have been performed in vitro. In practical reality the heterogeneity of the living cell environment makes it hard to resolve binding kinetics from other competing biophysical models, and most researchers default to using a simple two-component diffusion model where the second, slower, component reflects the interacting protein fraction. This two-component diffusion autocorrelation model is expressed as follows (Bacia & Schwille, 2003; Brazda et al, 2011) in Eq. 7:

$$G(t) = \frac{\gamma}{N}\left[\left(1+\frac{\tau}{\tau_{d1}}\right)^{-1}\left(1+\frac{K^2\tau}{\tau_{d1}}\right)^{-1/2} + \frac{1}{\rho}\left(1+\frac{\tau}{\tau_{d2}}\right)^{-1}\left(1+\frac{K^2\tau}{\tau_{d2}}\right)^{-1/2}\right] \quad (7)$$

, where N is the total number of molecules in the PSF , ρ is the concentration ratio of the two components, τ_{d1} is the characteristic diffusion time of the first (fast) component ($\tau_{d1}=\frac{\omega_r^2}{4D_1}$) usually representative of protein monomers, and τ_{d2} is the characteristic diffusion time of the second (slow) component ($\tau_{d2}=\frac{\omega_r^2}{4D_2}$) that is usually representative of bound or interacting protein.

1.2.4 Raster Image Correlation Spectroscopy (RICS)

Although point FCS is a powerful method for quantifying protein concentration and molecular mobility in solution, it is not robust to the spatial variability of protein dynamics inside the cell. To overcome this limitation while still inheriting the merits of FCS, an alternative method, Raster Image Correlation Spectroscopy (RICS), is ideal for obtaining temporal and spatial information about protein interaction dynamics simultaneously through repeated raster-scanning of a laser beam (Digman et al, 2005). The basis of the RICS approach is that the fluorescence fluctuation signal from successive pixels is partially correlated due to the motion of fluorescently tagged molecules as shown in Fig. 1.4. The spatial correlation computed from the experimental data is then fitted to appropriate biophysical models that predict this fluorescence correlation signal under molecular diffusion and/or binding conditions. The shape of the spatial correlation curve relies on the rate of diffusion and binding-unbinding, the spatial overlap of the excitation volume between successive scanning positions (the size of pixel) and the time interval between pixels and lines (Digman & Gratton, 2009). The sampling time among these parameters plays a critical role in determining the range of diffusion coefficients or other binding constants that are detectable. Therefore a suitable pixel dwell time needs to be selected in order to detect, for example, fast or slow diffusion. For this study, RICS analysis was applied for describing two-component diffusion via fitting the appropriate autocorrelation functions

accounting for these phenomena (Digman et al, 2009). There are two terms in the fitting equation for RICS analysis, as shown below:

$$G(\xi,\psi)=G_D(\xi,\psi)\cdot S(\xi,\psi) \quad (8)$$

, where $G_D(\xi,\psi)$ describes the fluorescence signal correlation due to diffusion, $S(\xi,\psi)$ describes the signal correlation due to raster scanning, and ξ and ψ are spatial increments in the x and y directions. Each term can be represented as below:

$$G_D(\xi,\psi)=\frac{\gamma}{N}\left(1+\frac{4D(\tau_p\xi+\tau_l\psi)}{\omega_0^2}\right)^{-1}\left(1+\frac{4D(\tau_p\xi+\tau_l\psi)}{\omega_0^2}\right)^{-1/2} \quad (9)$$

$$S(\xi,\psi)=\exp\left(-\frac{\left(\frac{\delta\gamma}{\omega_0}\right)^2(\xi^2+\psi^2)}{1+\frac{4D(\tau_p\xi+\tau_l\psi)}{{\omega_0}^2}}\right) \quad (10)$$

, where γ is a factor needed for the calculation of a 3D Gaussian shape illumination volume, N is the number of molecules inside the focal volume, τ_p is the pixel dwell time, τ_l is the scan time between two lines, $\delta\gamma$ is the pixel size, D is the diffusion coefficient, and ω_0 is the beam waist (Rossow et al, 2010). The term 4D in this equation becomes 8D in two-photon system due to the different shape of observation volume compared to the one photon system (Brown et al, 2008).

In reality, it is a rare event that the functional protein of interest contains only one species of diffusion coefficient, because it can interact to other proteins or DNA and also form a complex with the cytoskeleton. As a result, the two-component diffusion autocorrelation function fits the RICS data better and it has been the model of choice for all live cell data in this work. There are four terms in the fitting equation for RICS analysis in a two-component model, as shown below (Bacia & Schwille, 2003):

$$G(\xi,\psi)=G_{D1}(\xi,\psi)S_1(\xi,\psi)+G_{D2}(\xi,\psi)S_2(\xi,\psi) \quad (11)$$

, where $G_{D1}(\xi,\psi)$ and $G_{D2}(\xi,\psi)$ describe the fluorescence signal correlation due to diffusion, $S_1(\xi,\psi)$ and $S_2(\xi,\psi)$ describe the signal correlation due to raster scanning, and ξ and ψ are spatial increments in the x and y directions. Each term can be represented as below:

$$G_{D1}(\xi,\psi)=\frac{\gamma}{N_1}\left(1+\frac{4D_1(\tau_p\xi+\tau_l\psi)}{\omega_0^2}\right)^{-1}\left(1+\frac{4D_1(\tau_p\xi+\tau_l\psi)}{\omega_0^2}\right)^{-1/2} \quad (12)$$

$$G_{D2}(\xi,\psi)=\frac{\gamma}{N_2}\left(1+\frac{4D_2(\tau_p\xi+\tau_l\psi)}{\omega_0^2}\right)^{-1}\left(1+\frac{4D_2(\tau_p\xi+\tau_l\psi)}{\omega_0^2}\right)^{-1/2} \quad (13)$$

$$S_1(\xi,\psi)=\exp\left(-\frac{\left(\frac{\delta\gamma}{\omega_0}\right)^2(\xi^2+\psi^2)}{1+\frac{4D_1(\tau_p\xi+\tau_l\psi)}{{\omega_0}^2}}\right) \quad (14)$$

$$S_2(\xi,\psi)=\exp\left(-\frac{\left(\frac{\delta\gamma}{\omega_0}\right)^2(\xi^2+\psi^2)}{1+\frac{4D_2(\tau_p\xi+\tau_l\psi)}{{\omega_0}^2}}\right) \quad (15)$$

, where γ, τ_p, τ_l, ω_0, δr are consistent with their prior definitions above.

However, in reality fast molecular kinetics cannot be directly extracted from the above equations because the spatial autocorrelation function can be masked by an immobile or very slowly moving protein component originating from slow cell movement. Therefore, subtraction algorithms including immobile subtraction and moving average subtraction were applied in RICS analysis for eliminating the contribution of immobile background or slow moving features (Digman et al, 2005). In the immobile subtraction algorithm, each image frame of a stack is subtracted from the average intensity of the entire image stack, which has been shown to remove the spatial correlation contributed from the protein immobile fraction (Brown et al, 2008). To avoid negative intensities in pixels after subtraction, each image frame of a stack needs the average stack intensity added back to each individual image frame. In the moving average subtraction algorithm, for the case of a 10-frame moving average analysis, the average intensity of frame 5 would be subtracted from the average intensity of frames 1-10, frame 6 would be

subtracted from average intensity of frames 2-11 and so forth, as the moving average subtraction window slides forward through entire image stack. The first 5 and last 5 frames of an image stack are ignored in this analysis. In this work, the 10-frame moving average subtraction was applied to all data sets because cell movement occurred very often during RICS measurements.

In addition, the instrument settings, such as pixel dwell time, pixel size and ROI size, was very important for RICS measurement. The pixel dwell time is known to depend on the magnitude of the diffusion coefficient and on the signal to noise ratio, and the maximum value of pixel dwell time should less than $\frac{\omega_0^2}{4D}$, where ω_0 is the beam waist and D is diffusion coefficient (Rossow et al, 2010). The pixel size should be set at 4-5 times smaller than the focal volume size, which means that the focal volume corresponding to an image pixel partially overlaps with the focal volume corresponding to neighboring pixels (Rossow et al, 2010). In addition, the precision and accuracy of the diffusion coefficient depends of ROI size and the number of frames acquired, which should be at least 128x128 pixels and 50 frames, respectively (Brown et al, 2008). All RICS measurements in this work were acquired for 50 frames at a pixel dwell time of 10 µs and an ROI size of 256x256 pixels. The experimentally derived correlation curves were then fitted to the one-component diffusion model using Eqs. 8, 9 and 10, or the two-component diffusion model using Eqs. 11, 12, 13, 14 and 15 described above as coded in the Globals software (SimFCS program; Laboratory for Fluorescence Dynamic). In these data fits the diffusion coefficient and concentration were the free variables, while the axial and radial values of the Gaussian focal volume were assumed, based on prior calibration experiments using fluorescent nanobeads. Specifically, the beam waist.ω_0 was calibrated by performing RICS measurements in 10 nM fluorescent bead solutions, and subsequently fitting data using the Globals software while assuming the diffusion coefficient of the beads, based on their hydrodynamic radius, and their concentration, based on their known stock concentration (see Methods section 2.8.1). These calibration measurements were performed every time prior to

RICS measurements to take into account any daily drifts in the equipment setup. In this work RICS analysis was used in combination with PA-GFP to tune the fluorescent protein concentration in the cell to improve quantification of the molecular diffusion coefficient, as described in Chapter 5 below.

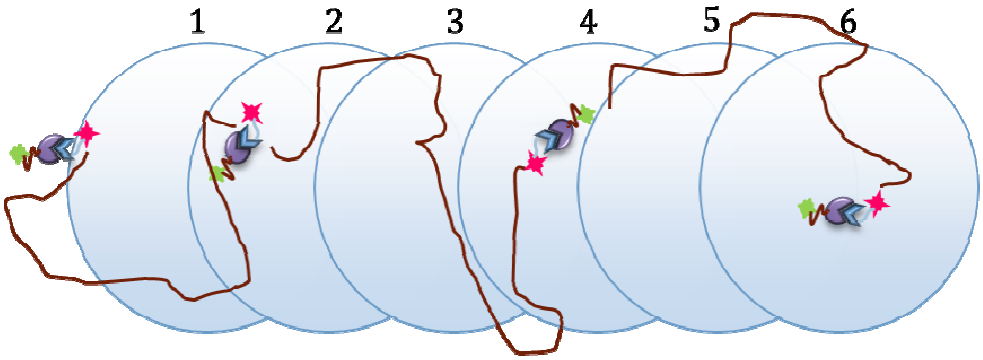

Figure 1.4 The basis of the RICS approach: As the focused beam is raster scanned the same molecule may enter it multiple times, which results in time-series fluctuation data that are analyzed by appropriate biophysical models to derive the underlying diffusion coefficient for each molecular population fraction.

1.2.5 Number and Brightness (N&B) Analysis

Although RICS analysis can provide concentration estimates for each diffusing component, the moving average removal and immobile fraction removal algorithms are applied in RICS analysis affect the accuracy of quantification of molecular concentrations (Brown et al, 2008; Digman et al, 2005). In practice, it is impossible that a cell will be completely still during a RICS measurement, and any statistical analysis process attempting to correct for large signal variations due to spatial heterogeneity, such as moving average, will also inevitably subtract some of the true signal. N&B analysis is a more robust method for the estimation of molecular concentration and brightness because it attains estimates of these quantities through use of simple statistical metrics, such the mean and variance of the detected fluorescence signal, as

opposed to signal autocorrelation that is more sensitive on background heterogeneity.

Specifically, the variance of intensity from N&B measurements contains two terms, the variance caused by the fluctuations in the number of particles in the observation volume and the variance caused by shot noise of the detector (Ossato et al, 2010). The variance is related to brightness and number of particles through the following expressions:

$$\sigma_p^2=\varepsilon^2 n \quad (16)$$

$$\sigma_d^2=\varepsilon n \quad (17)$$

$$<k>=\varepsilon n \quad (18)$$

, where ε indicates the number of photons emitted per molecule per second, and n represents the average number of molecules in the focal volume. The variance σ_p^2 due to fluctuation in the number of particles inside the focal volume and the variance σ_d^2 due to shot noise of the detector are both proportional to the brightness and number of particles and so is the average intensity $< k >$. The apparent brightness B is defined as the ratio of variance to average intensity and the apparent number of particles, N, is defined as the ratio of quadratic intensity to variance expressed as shown below (Digman et al, 2008):

$$B=\frac{\sigma^2}{<k>}=\varepsilon+1 \quad (19)$$

$$N=\frac{<k>^2}{\sigma^2}=\frac{\varepsilon n}{\varepsilon+1} \quad (20)$$

When the apparent brightness B is equal to 1, there is no variance of intensity because of no mobile molecules crossing the observation volume. Therefore in the pixel-wise map of B, the pixels with values close 1 can be used to identify the spatial distribution of the immobile fraction of molecules in the image. In addition, the degree of aggregation can be represented by the histogram of B values versus intensity. The above equations can be rewritten to extract the molecular concentration, n, and the molecular brightness, ε, by following expressions (Digman et al, 2008):

$$n = \frac{\langle k \rangle^2}{\sigma^2 - \langle k \rangle} \quad (21)$$

$$\varepsilon = \frac{\sigma^2 - \langle k \rangle}{\langle k \rangle} \quad (22)$$

Using Eq. 19 and Eq. 20 the degree of aggregation and molecular brightness maps in a cell can be obtained by analyzing the variance of intensity and average intensity pixel by pixel through a stack of acquired image frames (see Methods for details). As was the case for the RICS approach, in N&B analysis the pixel dwell time cannot be larger than the molecular transit time through the focal volume. If the time for a fluorophore crossing the illumination spot is shorter than the pixel dwell time, a reduction of variance and an increase in average intensity will occur which will bias the measured signal (Digman et al, 2008; Ossato et al, 2010). In this work, N&B analysis was used to determine the concentration of fluorescent proteins in the cell for a variety of experimental conditions and cell lines (see Methods section).

CHAPTER 2

Materials and Methods

Methods separate to two categories: molecular biology techniques and quantitative fluorescence fluctuation microscopy techniques. Molecular biology techniques include Western blot analysis, immunofluorescence, transfection, plasmid construction and generation of recombinant proteins. Quantitative fluorescence fluctuation microscopy techniques include Fluorescence Correlation Spectroscopy (FCS), Raster Image Correlation Spectroscopy (RICS) and Number and Brightness (N&B) analysis. These techniques involved the use of confocal and two-photon microscopy and calibration of focal volume size. For the case of RICS a new methodology had to be developed for determining optimal photoactivation concentration for protein diffusion coefficient quantification. The molecular biology techniques were primarily used in two projects, the interaction of AR and DAB2IP (Chapter 3) and the role of DAB2IP in DNA repair pathways (Chapter 4). The quantitative fluorescence fluctuation microscopy techniques were used for optimizing protein kinetics quantification (Chapter 5).

2.1 Cell Culture and Transfection

2.1.1 Conditions for Cell Maintenance

Human Embryonic Kidney 293 cells (HEK 293), DAB2IP stable transfected 293 cells (293-DAB2IP) and vector control subline (293-pCDNA), were maintained in Dulbecco's modified Eagle's media (DMEM) (Gibco) containing 10% fetal bovine serum (Invitrogen, Carlsbad, CA), 100 U/ml penicillin and 100 µg/ml streptomycin. C4-2 cells, DAB2IP stable transfected C4-2 cells (D2), vector control subline (Neo) and PC-3 were maintained in T media (Invitrogen) containing 5% fetal bovine serum, 100 U/ml penicillin and 100 µg/ml streptomycin. PZ-HPV-7

was maintained in PrEGM media (Lonza, Walkersville, MD) containing 100 U/ml penicillin and 100 µg/ml streptomycin. RWPE-1 cells were maintained in Keratinocyte medium (Invitrogen) containing 10% fetal calf bovine, 100 U/ml penicillin and 100 µg/ml streptomycin. All cell lines were obtained from American Type Culture Collection (Manassas, VA) and cultured in a 5% CO_2 humidified incubator at 37℃.

2.1.2 Transient Transfections

2.1.2.1 Transient Transfections for Quantitative Fluorescent Microscopy Methods

HEK 293 cells were seeded at a density of 3×10^5 into glass-bottom culture dishes with number 0 glass (MatTek, P35G-0-14-C), and then cultured for 48 hours to achieve 80% confluence. Cells were transfected with 1-7 µg of plasmid using Xfect (Clontech Laboratories Inc.) according to manufacturer's instructions. Cells were measured at 12-72 hours post-transfection using confocal microscopy or two-photon microscopy.

2.1.2.2 Transient Transfections for Nuclear and Cytoplasmic fraction extraction

HEK 293 cells were seeded in 8×10^5 per p60 dish (Corning, Tewksbury, MA), and then cultured for 48 hours to achieve 80% confluence. The amount of plasmid DNA used for transfection was 12 µg per dish, and then the rest of the procedure was the same as described in section 2.1.2.1. Cells were harvested at 48 hours post-transfection for Western blot analysis.

2.1.3 Generation of Stable Transfected Cell Lines

2.1.3.1 HEK 293 Stable Cell Lines Transfected with DAB2IP and AR

HEK 293 cells were seeded at 5×10^5 cells per well in a 6-well culture plate (Costar, Corning, NY), and then cultured for 24 hours to achieve 80% confluence (Chaudhary et al, 2012). Transfections were achieved using Lipofectamine LTX with PLUS (Invitrogen, Carlsbad, CA) by 4 µl lipofectamine per 1 µg of plasmid DNA according to the instructions of manufacturer. The cells were co-transfected with the combination of pCDNA3-DAB2IP and pCDNA3-GFP-AR

at the ratios of 9:1, 7:3, and 1:1, respectively, or single transfected with DAB2IP and CDNA3.1. The pCDNA3-DAB2IP construct was described previously (Zhang et al, 2003) and pCDNA3-GFP-AR constructs were obtained from Dr. Gioeli (University of Virginia, Charlottesville, VA). At 24 hours after transfection, cells were replated into 10 cm plates and selected by replacing standard media with media containing gentamycin sulfate (G418). To determine the optimal concentration of G418, the killing curve of cells not expressing the construct was used to determine the efficient dose of G418. Therefore, the transfected cells were grown in the presence of 600 µg of G418 per mL for 2-3 weeks in order to generate a stable cell clone. Subsequently, 50% of cells per dish were stored in liquid nitrogen and another half of them was harvested for fractionation, followed by Western blot analysis in order to confirm the expression level. HEK 293 cells stably co-expressing DAB2IP and AR-GFP with the ratios 9:1, 7:3, and 1:1 were named as 293-DAB2IP:AR/9:1, 293-DAB2IP:AR/7:3 and 293-DAB2IP:AR/1:1, respectively and HEK 293 cells stably expressing DAB2IP and pCDNA3.1 were called as 293-DAB2IP and 293-pCDNA, respectively.

2.1.3.2 HEK 293 Stable Cell Lines Expressing PAGFP-DAB2IP and EGFP-DAB2IP

HEK 293 cells were seeded at 3×10^5 cells per well in a 6-well culture plate, and cultured for 48 hours. Cells were transfected with PAGFP-DAB2IP, EGFP-DAB2IP, DAB2IP-PAGFP, DAB2IP-EGFP, PAGFP and EGFP (2 µg/well) using Lipofectamine LTX with PLUS by 4.5 µl lipofectamine per 1 µg of plasmid DNA according to the directions of the manufacturer , and then the rest of procedure was the same as in section 2.1.3.1. The selected, stable cells were maintained in DMEM containing 600 µg of G418 per mL for 2-3 weeks. 293-DAB2IP-PAGFP, 293-DAB2IP-EGFP, 293-PAGFP-DAB2IP, 293-EGFP-DAB2IP, 293-PAGFP and 293-EGFP were the HEK 293 cell's sub-lines which expressed DAB2IP-PAGFP, DAB2IP-EGFP, PAGFP-DAB2IP, EGFP-DAB2IP, PAGFP and EGFP, respectively.

2.2 Immunoblotting, Immunoprecipitation and Immunofluorescence Protocols

2.2.1 Western Blot

C4-2 D2, C4-2 Neo, RWPE-1, PZ-HPV-7 and transfected HEK 293 cells were washed once with cold phosphate-buffered saline (PBS) and lysed in 150-300 µl of cold lysis buffer [150 mM NaCl, 0.1% Triton X-100, 50mM Tris-HCL (pH7.5), 1 mM sodium fluoride, 1 mM sodiumpyrophosphate, 1 mM sodium pyrophosphate, 2 mM phenylmethylsufonyl fluoride, 10 mg/mL leupeptin, 10 mg/ mL aprotinin, and 1 mM EDTA] for 1 hour in ice. After incubating for 1 hour, the lysates were spun at 10500 revolutions per minute (RPM) at 4℃ for 10 min and the supernatants were transferred to clean microcentrifuge tubes. The concentrations of total protein in each sample were determined using a Bio-Rad Protein Assay or a bicinchoninic acid assay (BCA assay; Pierce Biotechnology, Rockford, IL) by use of spectrophotometer (Du 640; Beckman) measurements at 592 nm according to manufacturer's instructions.

The same amount of samples was loaded to 7%, 10% or 4-12% Bis-Tris NuPage gel (Invitrogen) and proteins were separated by size at 100 V for 20 min, and then at 120 V for 2 hours at room temperature (RT). The proteins were transferred from gel to nitrocellulose membrane either using a wet transfer apparatus (Bio-Rad) for 4 hours at 0.29 A at 0℃ or a Trans-Blot Turbo semi-dry transfer apparatus (Bio-Rad, Hercules, CA) for 14 min at 1.3 A at RT. To avoid nonspecific binding, membranes were blocked in a 2% skim milk (w/v) blocking solution for 1 hour at RT. Proteins of interest on the blotting membrane could then be probed using a primary antibody in 2% bovine serum albumin (BSA) solution at 4℃ overnight, after washing three times with PBST (1 x PBS / 0.1% Tween-20) over 15 min. The blotting membrane was washed three times with PBST over 15 min after primary antibody incubation, and then the blotting membrane was incubated with HRP-conjugate with secondary antibody at RT for 90 min. Chemiluminescence signal was generated by incubating blotting membrane with

SuperSignal West Dura Extended Duration substrate (Thermo Scientific, Rockford, IL) and was detected by AlphaImager (FluorChem HD2; Alpha Innotech) at 425 nm.

2.2.2 Nuclear and Cytosolic Fraction Extraction

C4-2 D2, RWPE-1, and transfected HEK 293 cells were harvested after cells were irradiated or when cells reached a density of 1.5×10^6 cells/mL, and then washed once with cold PBS. For preparation of different fractions, NE-PER kits (Pierce Biotechnology) were used according to the manufacturer's instructions. Briefly, to extract the cytosolic proteins only, cell pellets were lysed in 200 µl of cold CER I for 15 min on ice, and then incubated in 11 µl of cold CER II (NE-PER) for 1 minute on ice. The supernatant (cytoplasmic extraction), obtained by centrifugation at 16000 x g for 10 min at 4℃, was transferred to a clear pre-chilled microcebtrifuge tube.

Once the cytoplasmic extraction was obtained, the insoluble fraction was washed once in cold PBS. To extract the nuclear protein fraction, pellets were re-suspended in 100 µl of cold NER (NE-PER) for 1 hour and vortexed at the highest speed (14000 rpm) for 15 seconds every 15 min during 1 hour. The nuclear extraction fraction was then obtained by centrifugation at 16000 x g for 10 min at 4℃.

2*.2.3 Immunofluorescence*

There were two immunofluorescence protocols used in this work. The major difference between protocol I and protocol II was in the cell permeabilization step: in protocol I ice-cold 100% methanol was used for this purpose and in protocol II Triton X-100 was used instead. Triton X-100, a detergent, is more suitable for nuclear antigen staining because it is capable of dissolving partially the nuclear membrane (Senior & Gerace, 1988). Therefore, the immunofluorescence procedure for imaging DNA DSB kinetics followed protocol II.

2.2.3.1 Protocol I

Cells were seeded on a well of 8-well or 4-well culture chambered coverslip (LABTEK, Scotts Valley, CA) Cells were fixed in 4% paraformaldehyde for 15 min at RT, and then washed three times in cold PBS for 5 min each. The ice-cold 100% methanol was used to permeabilize the cells for 10 min, and samples were blocked in PBS containing 5% goat serum and 0.3% Triton X-100 for 1 hour at RT. Samples were incubated with primary antibody in PBS/Triton overnight at 4℃. After washing three times with PBS, samples were sequentially incubated with secondary antibody conjugated with fluorochrome in PBS/Triton for 1 hour at RT, and stained with 4',6-diamidino-2-phenylindole (DAPI).

2.2.3.2 Protocol II

Cells were seeded on a sterile glass coverslip keeping in a well of 6-well plate (Corning, Tewksbury, MA). After fixing, the cells washed three times in cold PBS for 10 min each. Cells were permeabilized by cold PBS containing 0.5% Triton X-100, instead of ice-cold 100% methanol, for 10 min at 4℃. Samples were blocked in PBS containing 5% Fraction V BSA and 1% goat serum for 1 hour at RT, and then washed three times with cold PBS. Samples were incubated with primary antibody in PBS containing 1% Fraction V BSA for 3 hours at RT and sequentially incubated with secondary antibody conjugated with fluorophore for 1 hour at RT in the dark. To remove extra antibody, samples were washed with PBS on a shaker for 15 min. and A drop of DAPI was placed on the slides and a coverslip was placed on top. The slides were stored at 4℃ in the dark.

2.2.4 Reagents

Antibodies used for Western blot were as follows: anti-Histone (1:500, Santa Cruz), anti-GAPDH (1:1000, Santa Cruz), anti-actin (1:5000, Sigma, St. Louis, MO), anti-FLAG (1:2000, Sigma, St. Louis, MO), anti-tublin (1:1000,), anti-GFP (1:1000, Abcam, Cambridge, MA), anti-Skp2 (1:300, Santa Cruz, Santa Cruz, CA), anti-p21 (1:2000, BD pharmingen, San Jose, CA).

Anti-p27 (1:2000, Cell signaling, Beverley, MA), anti-DAB2IP (1:650) (Xie et al, 2009), anti-vimentin (1:1000, Sigma, St. Louis, MO), anti-E-cadherin (1:1000, BD pharmingen, San Jose, CA) and anti-androgen receptor (1:1000, Sigma, St. Louis, MO).

Antibodies used for immunofluorescence were as follows: anti-Xpress (1:500, Invitrogen), anti-DAB2IP (1:50) (Xie et al, 2009), anti-FLAG (1:1000, Sigma, St. Louis, MO) and anti-γH2AX (1:1000, EMD-Millipore). Fluorescent dyes used for immunofluorescence were as follows: Alexa 594 (1:1500, Invitrogen, Carlsbad, CA), FITC (1:1500), Radamine-Tex-X (1:1000, Invitrogen) and DAPI (Prolong Gold; Invitrogen, Orange).

2.3 Generation of Recombinant Proteins

2.3.1 Plasmid DNA cloning

2.3.1.1 DAB2IP Plasmid Construction for Mammalian Systems

In PAGFP-DAB2IP construction, pcDNA3.1-DAB2IP (Zhang et al, 2003) was used as a template and the DAB2IP coding sequence was amplified by the polymerase chain reaction (PCR) using HotStar HiFidelity PCR kit (Quiagen) according to the manufacturer's instructions. The primer sequences used in PCR were as follows: forward primer 5'-GCAAG CTTATGCCGAGGCTGAAGGAGTCTCGCTCC-3'; reverse primer 5'-GCGAATTCGTTAACAA TTGCTGCTGTTTCTGAACTC-3'. To reserve the DNA fragment, the PCR product was generated 3'A-oberhangs with *Taq* polymerase and purified from 0.8% agarose gel using a CleanGel kit (Quiagen), and subsequently cloned into TOPO TA vector. The correct DAB2IP coding sequence was verified by DNA sequence analysis. The DAB2IP fragment was excised out by *HindIII* and *EcoRI* digestion and inserted into the pPAGFP-N1 (Patterson & Lippincott-Schwartz, 2002).

Due to a mistake in primer design, the stop codon between DAB2IP and PAGFP coding sequences needed to be removed, which was done using QuikChange site-directed

mutagenesis Kit (Stratagene). The primer sequences used for site-directed mutagenesis were: forward primer, 5'-GAAACAGCAGCAATTGTTTACGAATTCTGCAGTCGAC-3'; reverse primer, 5'-GTCGACTGCAGAATTCGTAAACAATTGCTGCTGTTTC-3'.

To clone PAGFP-DAB2IP, DAB2IP fragment, excised out of pDAB2IP-PAGFP by *HindIII* and *EcoRI* digestion, was inserted into PAGFP-c1, which had been modified by removing a base at a *BglII* digested site in order to generate an in-frame PAGFP-DAB2IP using the mung bean nuclease (New England Biolabs, Ipswich, MA). For EGFP-DAB2IP and DAB2IP-EGFP construction, the DAB2IP coding sequence was excised out of pDAB2IP-PAGFP and inserted into pEGFP-c3 and pEGFP-n1, respectively. In addition, the coding sequence for mCherry was sub-cloned into pPAGFP-DAB2IP by *NheI* and *BspeI* digestion.

2.3.1.2 Skp2 Plasmid Construction for Mammalian Systems

A plasmid vector with photoactivatable GFP (pPAGFP-c1) was digested using restriction enzyme *BglII*, and the sticky ends generated were filled in by T4 DNA polymerase to make it in-frame with the Skp2 coding sequence that eventually would be inserted. T4 DNA polymerase can catalyze the synthesis of DNA in the 5'→ 3' direction and result in blunt ends. This digest with blunt ends was self-ligated using T4 DNA ligase and then cut with *HindIII* and *EcoRI.* The Skp2 coding sequence was excised out of pXP-Skp2, a pCDNA4/HisMax-TOPO vector containing the Skp2 coding sequence (Lin et al, 2009), by *HindIII* and *EcoRI* digestion and subsequently cloned into the *HindIII* and *EcoRI* site of the modified pPAGFP-c1. In EGFP-Skp2 construction, the Skp2 coding sequence was amplified by PCR using pXP-Skp2 as a template. The primer sequences for PCR were: forward primer, 5'-GCGGAGCTCATGCACA GGAAGCACC TCCAG-3'; reverse primer, 5'-GCGAAGCTTCTATAGACAACTGGGCTTTTG-3'. The PCR product was purified from 0.8% agarose gel using a QIAquick Gel Extraction Kit (Qiagen) according to the manufacturer's instructions, and the purified PCR product was digested by *SacI* and *HindIII* and sequentially inserted into pEGFP-c3.

2.3.1.3 Bacterial Expression of EGFP, PAGFP, EGFP-Skp2 and PAGFP-Skp2

To generate a PAGFP expression vector, the PAGFP coding sequence was amplified by PCR using PAGFP-c1 as a template. The primer sequences used in PCR were as follows: forward primer, 5'-GCGAGATCTGTGAGCAAGGGCGAGGAGCTG-3'; reverse primer, 5'-GCG GGATCCCTTGTACAGCTCGTCCATGCC-3'. The PCR product, purified by a QIAquick Gel Extraction Kit from agarose gel, was inserted into pQE80L and pET28a by *Bgl*II and *BamHI*. For EGFP expression vectors, the EGFP coding sequence was amplified by PCR using pEGFP-c1 as a template and the primer sequences for PCR was the same as the primer used in the PAGFP expression vector. The PCR product, purified from agarose gel, was inserted into pQE80L and pET28a by *Bgl*II and *BamHI.*

Similar techniques were used to clone PAGFP-Skp2 and EGFP-Skp2 expression vectors. The pXP-SKp2 shown in 2.3.1.2 was used as template and Skp2 coding sequence was amplified by using the primers shown in sub-section 2.3.1.2. The Skp2 fragment, purified from agarose gel, was sub-cloned into pQE80-PAGFP, pQE80-EGFP, pET28-PAGFP and ET28-EGFP by *SacI* and *HindIII* digestion.

2.3.2 Recombinant Protein Purification

2.3.2.1 Purification of EGFP and PAGFP Protein

High-level expression and rapid production of recombinant proteins can be achieved by using Escherichia coli (E. coli) hosts. However, high-expression of recombinant proteins is usually limited by rare tRNAs. To improve high protein expression caused by the codon bias, BL21 codon plus competent cells (Stratagene), containing additional copies of specific tRNA, were used as host for all protein expression vectors in this study. The BL21 codon plus competent cells were transformed with pQE80-EGFP and then grown in 3 ml LB broth containing Ampicillin (50 µg/ml), at 37℃ at 350 rpm overnight. 1.5 ml of bacterial culture was transferred into 260 ml of fresh LB broth containing Ampicillin, and grown until an OD_{600} of 0.5

was reached. Transformed cells were incubated with 1 mM Isopropyl β-D-1thiogalactopyranoside (IPTG) at 30℃ at 150 rpm for 6.5 hours. Cells expressing EGFP were spun by centrifugation at 9000 x g at 4℃ for 15 min. Cell pellets were lysed using Tractor buffer with 1 mM phenylmethanesulfonylfluoride (PMSF) at 4℃ for 15 min. The Tractor buffer was provided by HisTALON Gravity column purification Kit (Clontech). The supernatant was obtained by centrifugation at 10000 x g at 4℃ for 20 min, and then filtered through a 0.22 µm filter. Recombinant EGFP protein was purified using a column by HisTALON (Gravity column purification Kit) according to the instructions of the manufacturer. The procedure described above was also used to yield the recombinant PAGFP protein. The QE80l vector system, instead of ET28a vector system, were selected for generating EGFP and PAGFP protein, because in same condition of purification the production of EGFP or PAGFP generated from transforming competent cells with QE80-EGFP or QE80-PAGFP was higher than that with ET28-EGFP or ET28-PAGFP shown as in Fig. 2.1. Competent cells expressing QE80-GFP could yield more recombinant EGFP protein in either 0.5 mM or 1 mM IPTG at 0, 2, 4, 6 hours post-induction.

2.3.2.2 Purification of EGFP-Skp2 and PAGFP-Skp2 Protein

Similar techniques were used to produce PAGFP-Skp2 and EGFP-Skp2 protein. However, transformed cells had to be incubated with 0.5 mM IPTG at RT for 4 hours 30 min in order to reduce degradation of the protein.

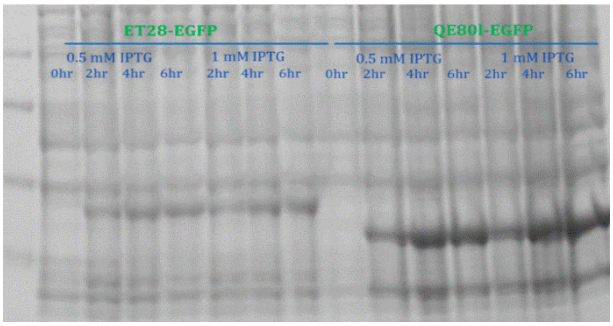

Figure 2.1 Expression of EGFP protein. Cell lysate was parted by 10% NuPage and probed using Coomassie Blue dye.

2.4 Colony Assay

2.4.1 Colony Survival for 293-DAB2IP and 293-pCDNA

Exponentially growing 293-DAB2IP and 293-pCDNA cells were harvested using trypsinization and counted using a particle counter (Beckman Coulter, Fullerton, CA). Cell suspensions were diluted into the appropriate seeding concentration, depending on the severity of the treatment, and then plated into p60 dishes in triplicate. Cells were treated with increasing doses of ionizing radiation (IR) (2, 4, 6 and 8 Gy) using a ^{137}Cs source (Mark 1-68 irradiator; J.L. Shepherd & Associates, San Fernando, CA) after 4 hours of incubation. After 14 days, cells were washed carefully with PBS, and then PBS containing 4% formaldehyde and 0.05% crystal violet was used to fix and stain cells. Colonies containing more than 50 cells were counted. The plating efficiency (PE) and surviving fraction (SF) of cells was calculated by equation (23) and (24) (Franken et al, 2006). The experimental data were fitted using a least-squares fit algorithm according to the curve $S=e^{-(\alpha D+\beta D2)}$ using the program GraphPad Prism (GraphPad Software, La Jolla, CA).

$$PE=(\text{number of colonies}/\text{number of cells seeded}) \times 100\% \quad (23)$$

$$SF=\text{number of colonies}/(\text{number of cells seeded}\times PE) \quad (24)$$

2.5 Luciferase Assay

2.5.1 Luciferase Assay for 293-ARS81D

The transcriptional activity of ARS81D was measured using ARE-luciferase reporter construct by a luciferase assay. Cells seeded in 6-well plates were co-transfected ARE-luciferase reporter construct, β-galactosidase reporter construct and DAB2IP-specific siRNA. Cells were treated with DHT 48 hours after transfection. Then cells were harvested and

assayed for luciferase activity, which was measured using the Reporter Assay System (Promega, Madison, WI).

2.6 Preparation of Calibration Samples for Microscopy

2.6.1 Fluorescent Beads

Green aqueous fluorescent particles, 25 nm beads (G25; Thermo scientific, Rockford, IL), were made of polystyrene and had a refractive index of 1.59. To calibrate the waist of the laser beam at the focus of the objective lens, G25 beads were sonicated for 10-15 minutes and diluted in nanopure H_2O to 10 nM in order to disperse aggregates. The beads were then sonicated for 25 min and 130 µl of the solution was plated in 8-well chambered coverglass chambers (Lab-Tek, Campbell, CA). The glass bottom side of the chambers, through which the measurements were performed, was between 0.13 and 0.17 mm.

2.6.2 Recombinant EGFP Protein

Once EGFP protein was purified from the expressing cells, the concentrations of the stock was determined using the BCA Protein assay kit (Pierce; Thermo Scientific, Rockford, IL) by spectrophotometer absorbance measurements at 592 nm according to the instructions of the manufacturer. The stock of EGFP solution was then concentrated by ultrafiltration using a Centricon 50 filter (Ambion), and stored with 20 mM Tris buffer (pH7.4), containing 1 mM PMSF, 200 µM sodium orthovanadate (Na_3VO_4), and 10 mM Sodium Fluoride at -20℃. To prevent the absorption of EGPF onto the coverglass during measurements, EGFP solutions had to be diluted with 0.2% BSA to their final concentration of 10 nM. EGFP would precipitate at the surface of the chambered coverglass if this 0.2% BSA dilution step were not performed, which would reduce the fluorescence intensity of the solution and lead to biased concentration estimates.

2.7 Microscopy Setups

2.7.1 Confocal Microscopy

The optical apparatus for live cell imaging was a Zeiss LSM 510 META inverted microscope (Zeiss, Oberkochen, Germany). The objective lens was a 63X Plan-Apochromat (1.4 NA) oil immersion and a photomultiplier tube (PMT) was used for light detection. The live cell staining probe Alexa 594, conjugated with IgG, was excited at 543 nm with a HeNe laser, using a dichroic HFT405/488/543/633 mirror and fluorescence was detected through a LP610 long pass filter. DAPI was excited at 405 nm with a diode laser, using a dichroic HFT405/488/543/633 and fluorescence was detected through a BP420-480 band pass filter. EGFP, expressed in HEK 293 cells, was excited at 488 nm with an Argon laser, using a dichroic HFT405/488/543/633 mirror and fluorescence was detected through a BP505-530 band pass filter. For photoactivation measurements, PA-GFP was photoactivated at 405 nm with a diode laser and fluorescence was excited at 488 nm with an Argon laser, using an HFT405/488 dichroic and a LP 505 long pass filter (Fig. 2.2).

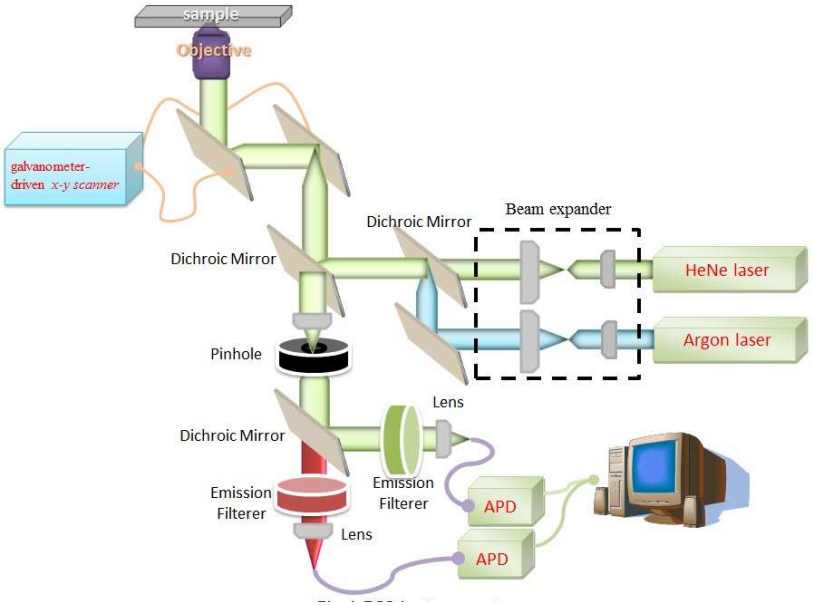

Figure 2.2 The confocal microscopy instrument setup.

2.7.2 Two-Photon Microscopy

The two-photon excitation fluorescence microscope is an in-house assembly of commercial parts. The laser excitation source is a Diode-pumped Ti:Sapphire mode-locked laser (Chameleon Ultra laser; Coherent Inc.) with 150 fs pulse width, with a 690-1040 nm tuning range and an 80 MHz pulse repletion rate. The laser beam first passed through a achromatic half-wave plate and a Glan-Laser Calcite Polarizer (Newport, Santa Clara, CA) used for adjustment of the laser power (Fig. 2.3). Furthermore, the two-photon photoactivating power at 765 nm needed to be small relative to the excitation power at 920 nm in order to avoid a rapid increase of photoactivated protein concentration during imaging. To address this issue a dichroic mirror 750LP was placed in the beam path and the angle of the dichroic mirror axis was adjusted to reflect 30% and 98% the activating light at 765 nm and excitation light at 920 nm, respectively, in order to reduce the activating laser power at 765 nm (Fig. 2.3). Then, the size of the laser beam was increased by travelling through a beam expander before entering the x-y scanner box. The x and y galvanometer scanner mirrors (Model#91031; ISS, Champaign, IL) in this scanner box were used to guide the laser beam into the microscope. The laser beam was focused into the sample by a 63X (1.2 NA) water immersion objective (Zeiss, Jena, Germany). PAGFP was photoactivated at 765 nm and excited at 920 nm, using a dichroic filter (long pass, Chroma Technology, Bellows Falls, VT), and a band pass filter (band pass, Chroma Technology, Bellows Falls, VT). Finally, a PMT, operating in photon counting mode, (Model: H7421; Hamamatsu, Bridgewater, NJ) was used for detecting the fluorescence emission. The cell culture dish holder on the microscope stage was home-made, as shown as in Fig. 2.3. The cell culture dish was maintained at 37 ℃ using the obje ctive heater (Zeiss, Jena, Germany).

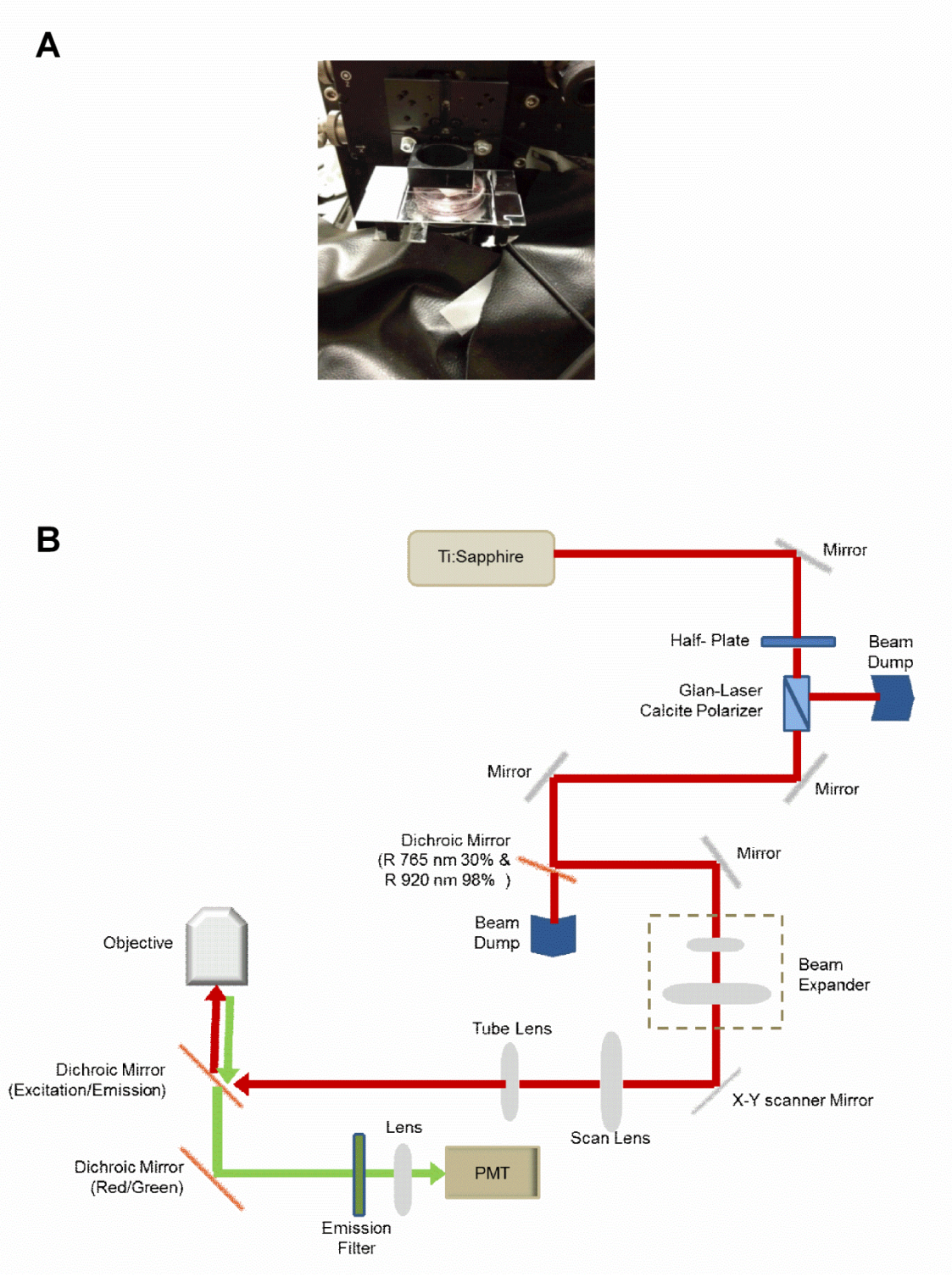

Figure 2.3 Schematic of (A) culture dish holder and (B) the two-photon microscope setup

2.8 Incremental Photoactivation Process for Improved Quantification of Molecular Dynamics

2.8.1 Calibration of Focal Volume Size and Determination of Spatial Resolution

To calibrate the focal volume of the excitation beam, the autocorrelation curves of 10 nM fluorescent beads (25 nm beads) or of 10 nM EGFP recombinant protein were measured using the RICS analysis method (Digman et al, 2005). The scan area for RICS measurements was 256 x 256 pixels, 0.05 µm per pixel, defining a 12.8 µm x 12.8 µm, field of view in total, with a dwell time of 10 µs/pixel. After computation of the autocorrelation by use of the Globals software (SimFCS program; Laboratory for Fluorescence Dynamics) the data was fitted to the one-component diffusion model using Eqs. 8, 9 and 10 with wr, wz and concentration as the free variables and assuming the known bead diffusion coefficient of 17.9 $\mu m^2/s$ or the known EGFP diffusion coefficient of 99 $\mu m^2/s$. These diffusion coefficients were calculated using the Stokes-Einstein relation $r_h = \frac{kT}{6\pi\eta D}$, where k is the Boltzmann constant, T the absolute temperature and η the viscosity of water (Wang et al, 2003).

2.8.2 Photoactivation Set-up

PA-GFP is capable of switching on from a non-fluorescent state to a fluorescent one in response to 765 nm light irradiation (Schneider et al, 2005). The amount of photoactivated PAGFP in solution was controlled by varying the total amount of light energy delivered to the sample, which depended on the activation light laser power, pixel dwell time and the size of the activated ROI. In our two-photon microscopy system the laser power was adjusted by a half-wave plate and polarizer combination and the photoactivated protein concentration was tuned by different photoactivation durations, repeated scanning over the same region, at a fixed laser power of 2mW at the objective's focus. The size of the photoactivated region of interest (ROI) was 64x64 pixels and 0.004 µm per pixel (1.056 µm X 1.056 µm), and the pixel dwell time was 10 µs. HEK 293 cells expressing PA-GFP or PAGFP-Skp2 were serially photoactivated to an

optimal concentration for RICS by serially incrementing the total photoactivated dose delivered to that ROI.

2.8.3 Determination of the Optimal Photoactivation Concentration for RICS Analysis

The photoactivation concentration was used as a tunable tool to improve the ability of RICS to quantify the protein diffusion coefficient in living cells. To that end the concentration of photoactivated fluorophore was increased incrementally and the accuracy of the resulting molecular diffusion coefficient, as compared to published values in the literature, was determined by RICS (Digman et al, 2005) before the concentration was increased further. By starting at very low photoactivated fluorophore concentrations where a RICS curves were not detectable and incrementing the fluorophore concentration to the hundreds of µM range, which is the upper limit of the RICS method, the accuracy of determining the molecular diffusion coefficient for the whole range of measureable concentrations was tested. Specifically, PA-GFP or PAGFP-Skp2 was serially activated by the increment of activated duration with the condition shown as in sub-section 2.8.2. The number of fluorophores per pixel after each photoactivation step was determined using number and brightness analysis (Digman et al, 2008).

The RICS measurements in each cell were performed 5 times from low photoactivation concentration to high photoactivation concentration (40-800 nM). The photoactivation concentration is proportional to fluorescent intensity which can be directly represented by photon count rate. Therefore, for each cell measured the activation dose was adjusted to produce 100, 300, 500, 700 and 900 X 10^3 counts per second (cps). Variability in RICS measurements between different cells could be created by cell movement, differences fraction of slow species that may bias the mobile fraction diffusion coefficient to lower values, and cell size as cells which is smaller than ROI size are less homogeneous, and therefore RICS measurement in each cell were performed 5 times from low to high photoactivation concentration.

Clearly, in order to quantify the dependence of the photoactivated protein diffusion coefficient on its cellular concentration the latter also needed to be quantified in each cell after each photoactivation step. Specifically, the variance of photon count rate for each pixel in an image stack was converted to fluorophore concentration using N&B analysis. For N&B analysis, the instrument settings of this work were set at 50 frames, pixel dwell time of 10 μs and a ROI size of 256x256 pixels. The experimentally derived image stack was then fitted using Eq.21 and 22 (section 1.2.5) as coded in Globals software (SimFCS program; Laboratory for Fluorescence Dynamic) where ε and n are the fitting parameters (Digman et al, 2008). The parameter ε means molecular number for each pixel in an image stack and the calibrated focal volume (section 2.8.1) was used to the conversion of molecular number per pixel to molecular concentration. This standardized procedure was performed in at least 10 different cells for each fluorescently tagged protein type in order to obtain an estimate of the mean and standard deviation of molecular diffusion coefficient values at each photoactivated protein concentration. The optimal range of photoactivated molecule concentrations was considered to be the one where the determined diffusion coefficient was consistent with the estimated Stokes-Einstein value for each protein type. These estimated values were 23.5 $\mu m^2/s$ for PA-GFP and 16.8 $\mu m^2/s$ for PAGFP-Skp2, which were lower than than the aqueous solution values by a factor of 4 to compensate for the increased cytoplasmic viscosity (Chen et al, 2002; Schwille et al, 1999; Wang et al, 2003) If the estimated diffusion coefficient values for each protein type were attained at more than one photoactivated protein concentration, the optimal concentration was considered the one producing the minimum possible standard deviation in diffusion coefficient values.

CHAPTER 3

THE INTERACTION BETWEEN AR AND DAB2IP

3.1 Background and Significance

Abnormal AR activities including constitutively active AR splice variants, increased AR sensitivity and activated AR via crosstalk with other signaling pathways were frequently found in lethal castrate resistance prostate cancer due to cancer metastasis (Dehm et al, 2008; Gregory et al, 2001; Wen et al, 2000). Therefore active AR and its associated pathways is a major target in the development of therapies for aggressive prostate cancer. AR signaling activity goes through both genomic and non-genomic pathways. In the genomic pathway the AR forms a complex with co-activators or repressors, translocates to the nucleus and then binds to androgen-responsive elements in order to regulate the expression of target genes (Heinlein & Chang, 2002; Shang et al, 2002). The non-genomic effect is that AR is also able to interact with several signal effector proteins in the cytosol to change their cellular function (Costarella et al, 1996; Kousteni et al, 2001).

In contrast to the expression of AR that elevated in aggressive prostate cancer, loss of DAB2IP expression, suppressed by EZH2, commonly occurs in aggressive prostate cancer (Chen et al, 2003; Min et al, 2010). Interesting, the EZH2 expression is usually elevated in castration resistant prostate cancer and can be suppressed by androgen through AR (Bohrer et al, 2010). The loss of DAB2IP can induce EMT in either prostate cancer or epithelial cell lines and promote tumor growth *in vivo* (Xie et al, 2010). EMT is critical process for the development of aggressive prostate cancer. Importantly, the mechanism by which AR transcriptional activity is induced by the factors, such as peptide growth factor, through phosphorylation of AR may cause the development of castration resistant prostate cancer. Moreover, apoptosis activities and growth rate in prostate cancer cell can be modulated by DAB2IP (Wang et al, 2002; Xie et

al, 2009). Conversely, cell survival and proliferation can be modulated by AR transcriptional activity (Dehm & Tindall, 2006). However, knowledge of the role of DAB2IP in the activation of AR signaling pathways is extremely little. In this work we explored the mechanism of how DAB2IP is involved in the AR genomic pathway in an HEK 293 cell line stably expressing AR-GFP.

3.2 Results and Discussion

3.2.1 Kinetics of AR Nuclear Translocation

In the genomic pathway, the wild-type AR nuclear translocation is responsive to the presence of androgen such as DHT, and activated AR is associated with co-activators or suppressors to initiate target gene regulation in the nucleus. The regulation of AR activation in the genomic pathway can be modulated by the levels of androgen and AR (Waltering et al, 2009). HEK 293 cell subline stable expressing chimeric AR-GFP was used to investigate the intracellular dynamics of AR with different levels of androgen using N&B analysis. To observe the intracellular movement of activated AR in response to androgen, initially HEK 293 cells should be maintained in the media without hormonal ligands. Therefore, HEK 293 cells were cultured in standard media with 5% charcoal-stripped serum for two days and the unliganded AR-GFP was primarily in the cytoplasm as a heteromeric complex with heat shock proteins (Jenster et al, 1993) Subsequently, the time-dependent and dose-dependent nuclear translocation of AR-GFP was followed by adding different levels of DHT in the culture medium. The numbers of AR-GFP in nuclear and cytoplasmic compartment were determined by N&B analysis as a function of time after adding DHT. In addition, physiological testosterone levels in a young adult male is the vicinity of 10 nM (Goldenberg et al, 2011; Zitzmann & Nieschlag, 2001) and serum testosterone levels in a patient after castration treatment is ≤ 50 ng/dL (~1.6 nM) (Oefelein et al, 2000). According to these observations, the 1 nM DHT was set to simulate the

serum testosterone levels in a man after castration. After a 1 nM DHT treatment, the numbers of AR-GFP molecules was recorded in the cytosol and the nucleus at different times post-treatment and plotted as fraction to the total concentration in Fig. 3.1A. The time-course study shows that the nuclear fraction of AR gradually increases and the nuclear import reaches to 90% at approximately 120 min post DHT-induction. Subsequently a titration study was performed to quantify differences in AR translocation kinetics for doses of DHT that spanned its physiological concentration range (0.1-1 nM) (Potter et al, 2006). The results presented in Figs. 3.1B and 3.1C show that the rate of AR nuclear translocation at 0.1 nM DHT is slower than that seen for the 0.5 nM and 1 nM DHT treatments with the nuclear import fraction only reaching ~70% at 300 min post 0.1 nM DHT-induction. 90% AR imported to nuclear at approximately 120 min post 1 nM DHT-induction, and therefore the role of DAB2IP in AR nuclear translocation was observed at this time point. In addition, 1 nM DHT was consistently used in this study, because the rate of AR nuclear translocation was faster and convenient for experiments.

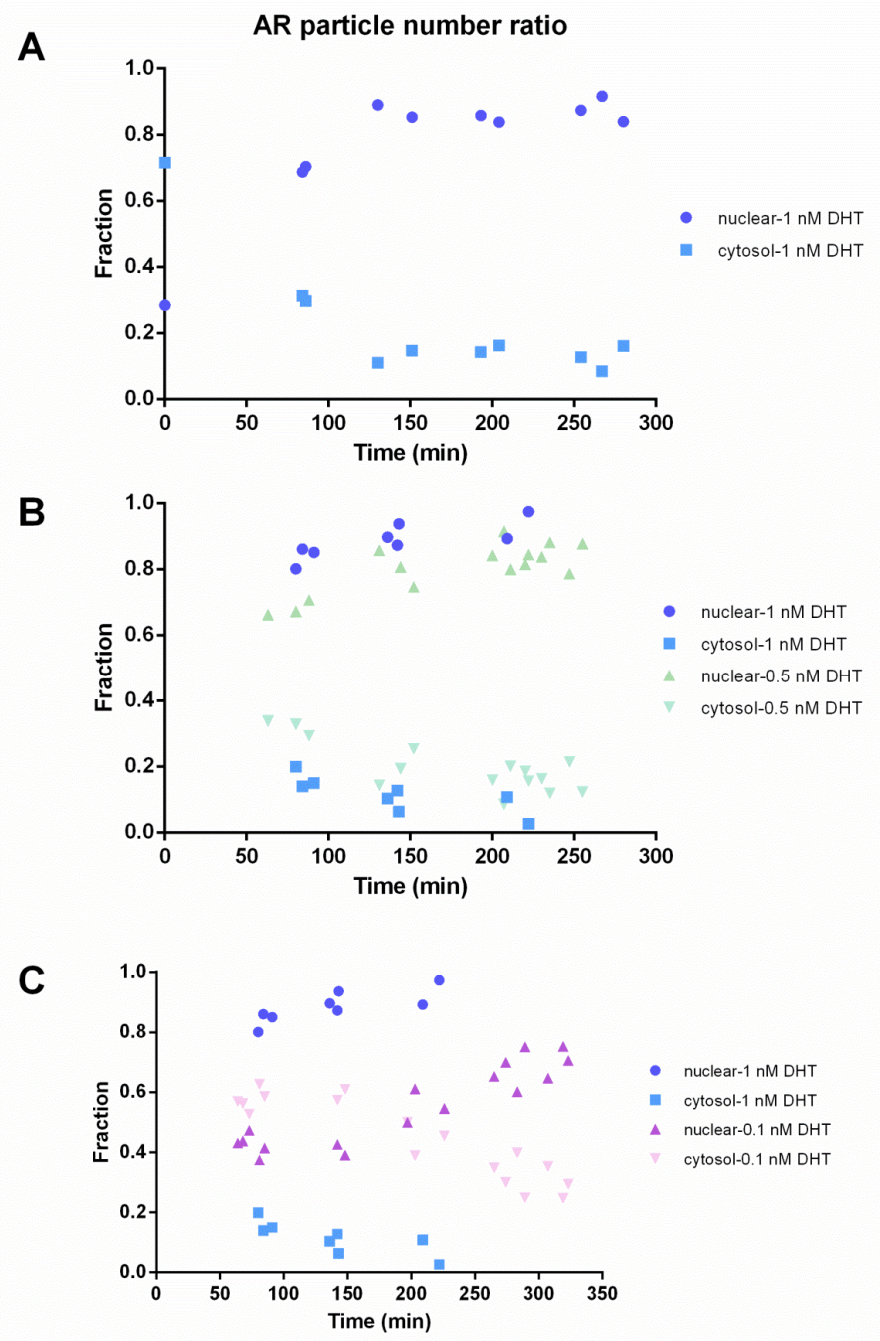

Figure 3.1 AR particle number ratio in the cytoplasm and the nucleus as a function of time after induction with different levels of androgen. 293-AR-GFP cells were used to determine the AR molecule number density using N&B analysis as a function of time after treatment with 1 nM DHT (A), 0.5 nM and 1 nM DHT (B) and 0.1 nM and 1 nM DHT (C).

3.2.2 DAB2IP Induces AR Cytoplasmic Sequestration

To examine the effect of DAB2IP on AR nuclear translocation, the intracellular distribution of AR in HEK 293 cells transiently co-expressing AR-GFP and DAB2IP was compared to that in HEK 293 cells transiently co-expressing AR-GFP and control vector. Then, these samples were stained with anti-DAB2IP antibody conjugated with Alexa 594. However, the results (not shown here) revealed no significant difference between these two samples. Therefore, HEK 293 stable sublines, instead of transiently transfected cells, were used to investigate the mechanism of DAB2IP action on AR nucleocytoplasmic movement. The strategy was that HEK 293 cells were co-transfected in combination with DAB2IP and AR-GFP constructs at different ratios. The expression levels of AR-GFP and DAB2IP in HEK 293 stable sublines, 293-DAB2IP:AR-GFP, 293-DAB2IP and 293 AR-GFP, were confirmed by Western blot analysis as shown in Fig. 3.2. In HEK 293 stable cell clones, 293-DAB2IP:AR/7:3 CL3 (Methods section 2.1.3.1) successfully expressed both AR-GFP and DAB2IP and was used to investigate the nucleo-cytoplasmic movement of AR-GFP. In 293-DAB2IP:AR/7:3 cells (section 2.1.3.1), the majority of AR-GFP was still located in the cytosol even after treatment with 1 nM DHT (Fig. 3.3A). The result implied that DAB2IP could inhibit AR-mediated genomic activity by preventing AR nuclear translocation. This concept was also proved in the prostate cancer cell line C4-2. C4-2 cells were transiently co-transfected with DAB2IP and AR-GFP constructs in the ratio of DAB2IP to AR is 8:2. AR-GFP was still predominantly cytoplasmic after the treatment with 1 nM DHT (Fig. 3.3B).

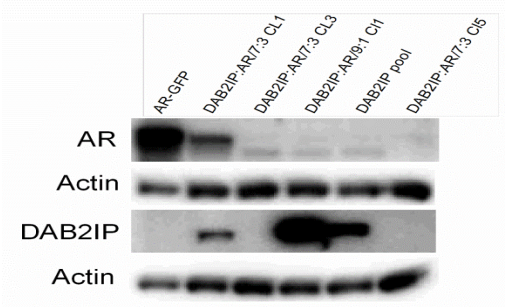

Figure 3.2 Expression levels of AR and DAB2IP in individual HEK 293 stable cell clones.

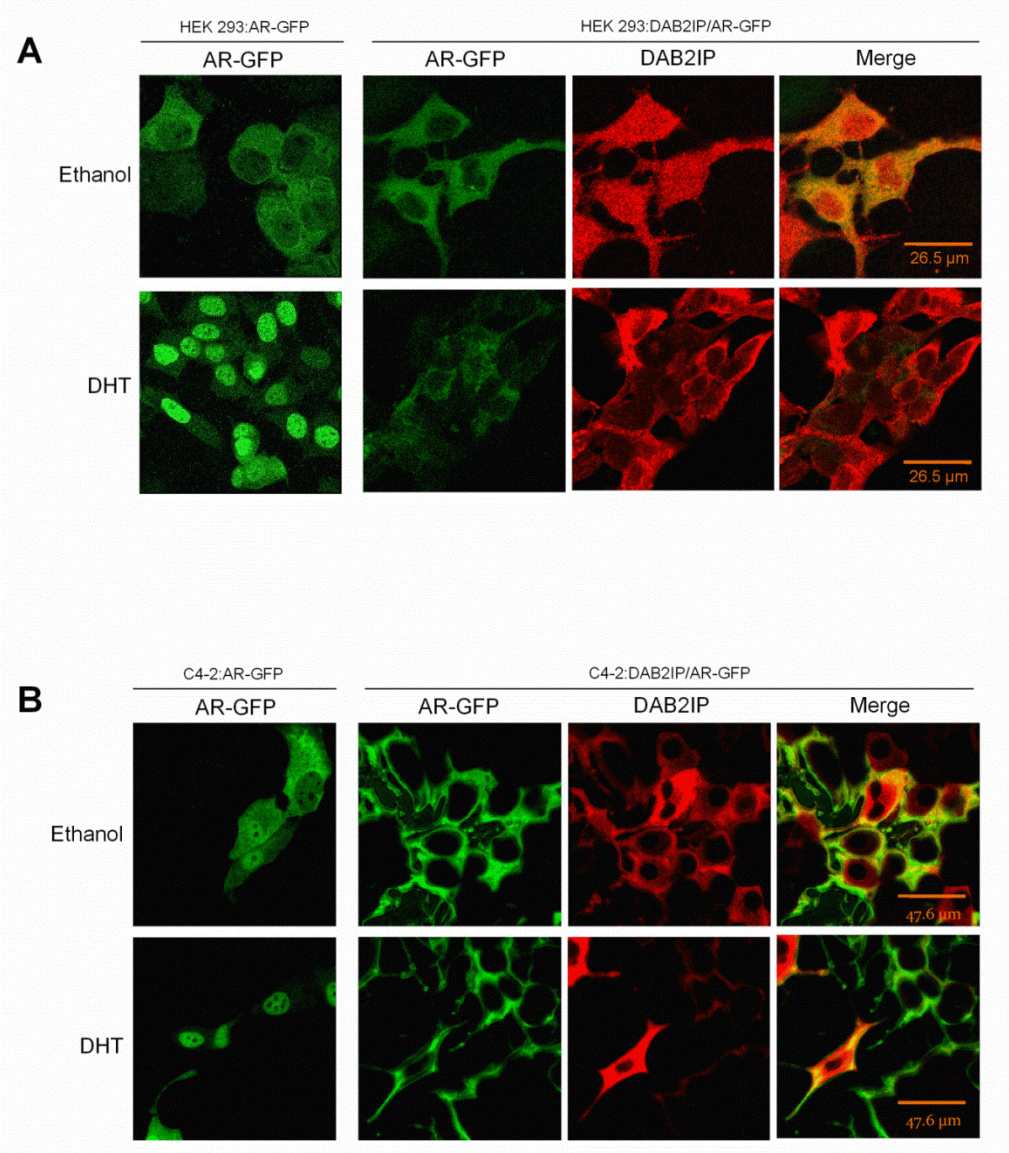

Figure 3.3 The inhibition of androgen-dependent AR nuclear translocation by DAB2IP. (A) After treatment with 1 nM DHT in 293-DAB2IP:AR-GFP and 293-AR-GFP cells for 2 hours, the cells were immuno-stained for DAB2IP (red, Alexa596). The subcellular distribution of AR-GFP and DAB2IP was visualized by confocal microscopy. (B) C4-2 cells were co-transfected with AR-GFP and DAB2IP constructs and then treated with 1 nM DHT for 2 hours. After DAB2IP immunostaining as in (A), the subcellular localization of AR-GFP and DAB2IP in C4-2 cells was observed by confocal microscopy.

3.2.3 The Nuclear Translocation of Mutant AR

Previous studies suggest that phosphorylation of AR plays a vital role in AR-mediated transcriptional activation (Lindzey et al, 1994) and the phosphorylation status is correlative to the functional status of the AR (Gioeli et al, 2006; Wang et al, 1999). These observations strongly suggest that understanding the mechanism by which phosphorylation of AR is modulated to induct the AR transcriptional activity is significantly important for progression to androgen-refractory prostate cancer. In this work we focused on the, Serine 81 and 650 phosphorylation site mutants of AR that are both considered important for altering the function of AR. Specifically, in a previous study the Ser-81 phosphorylation site had the highest stoichiometric phosphorylation in response to the induction of androgen (Gioeli et al, 2002; Gordon et al, 2010) and Ser-81 phosphorylation was associated with AR chromatin binding for transcription (Chen et al, 2012). Also, the Ser-650 phosphorylation site, located in DNA binding domain of AR, could promote AR nuclear export to limit its nuclear concentration and then reduce the expression of the AR target gene (Gioeli et al, 2006).

Unpublished results from Dr. Hsieh's lab show that DAB2IP can suppress phosphorylation of AR at Ser-81 site through PP2A, after treatment with DHT and then inhibit its transcriptional activity. However, the nuclear translocation of ARS81D, mutation of Serine 81 to the phosphomimetic amino acid aspartate, could not be blocked by DAB2IP in the presence or absence of androgen (Fig. 3.4A). In addition, ARS81D transcriptional activity was measured using ARE-luciferase reporter construct by a luciferase assay and nevertheless DAB2IP failed to inhibit the ARS81D-mediated transcriptional activity (Fig. 3.4B). These results imply that DAB2IP failed to in either inhibiting the transcriptional activity mediated by AR or to block AR nuclear translocation when AR was constitutively active at Ser-81 site.

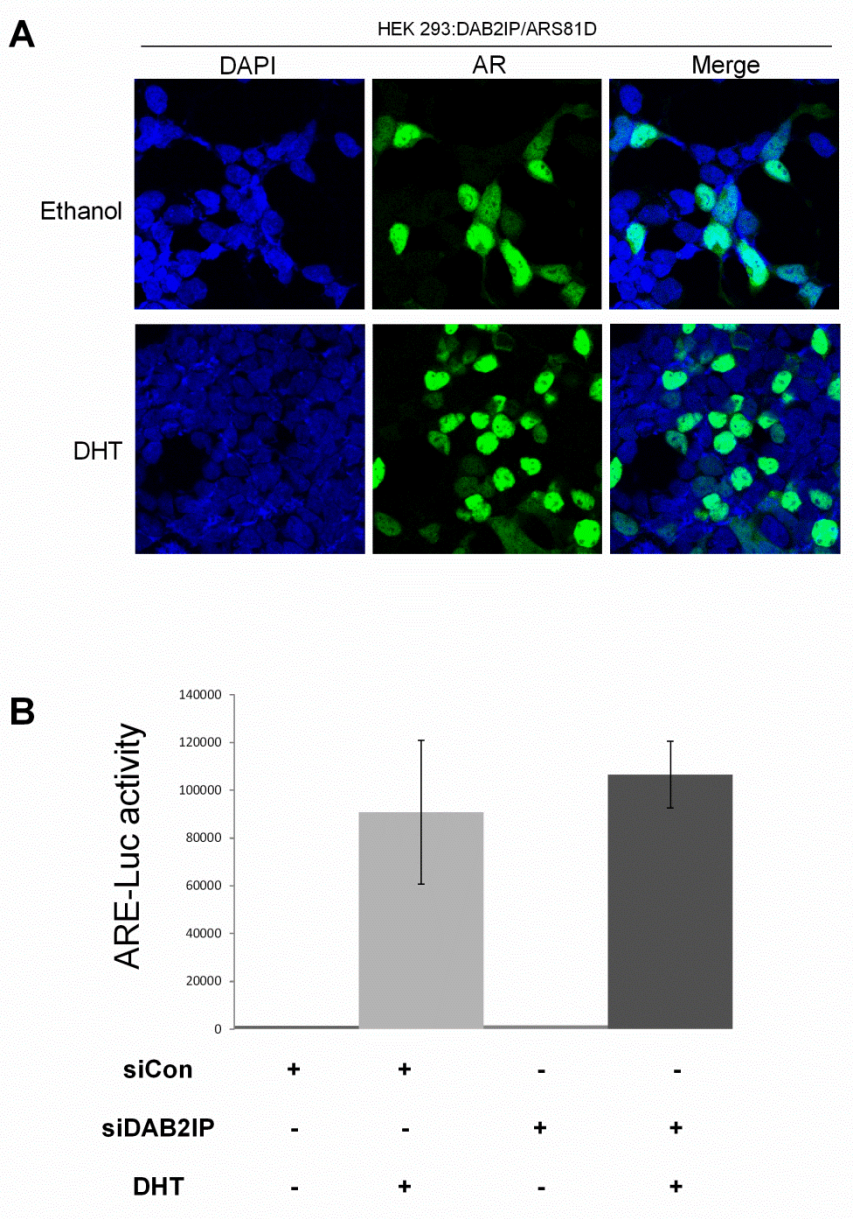

Figure 3.4 DAB2IP failed to inhibit the nuclear translocation of the constitutive active AR variant, ARS81D. (A) After treatment with 1 nM DHT for 2 hours, ARS81D in 293-DAB2IP/ARS81D cells was stained with anti-AR antibody conjugated with FITC. The subcellular distribution of ARS81D was observed by confocal microscopy. (B) 293-DAB2IP/ARS81D was co-transfected with an ARE-Luc construct and DAB2IP-specific siRNA and then treated with 1 nM DHT. Cells were harvested for fractionation, which was followed by a Luciferase assay.

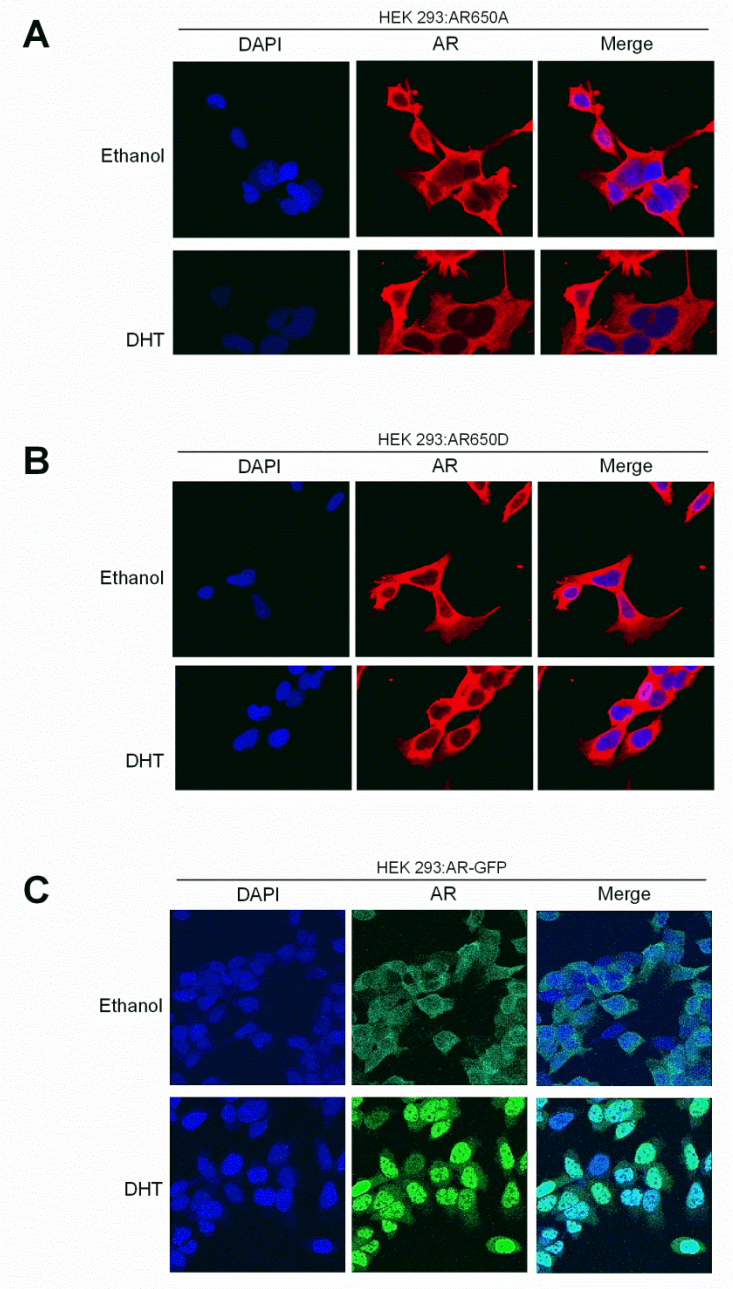

Figure 3.5 ARS650 failed to translocate into nucleus. HEK 293 cells were transfected with ARS650D (A) or ARS650A (B), and then treated with 2 nM DHT for 2 hours. Samples were immuno-stained with AR (red, Alexa 594) and subsequently the subcellular distribution of AR was observed by confocal microscopy. (C) Subcellular distribution of AR-GFP in 293-AR-GFP cells.

In addition, phosphorylation of Ser-650 is required for nuclear export to limit AR nuclear concentration, and hence the hypothesis to test here was whether DAB2IP could increase nuclear export to inhibit the transcriptional activity of AR by modulating the phosphorylation of Ser-650. However, the data shown in Figs. 3.5A and 3.5B reveal that the ARS650D and ARS650A, mutations of Ser-650 to the phosphomimetic amino acid aspartate and alanine respectively, both failed to translocate into the nuclear compartment in response to androgen simulation. Therefore, there is no model for verification of this hypothesis.

3.3 Conclusion

The amplification, hypersensitivity and mutation of AR, and abnormal AR signaling activation usually occur in lethal castrate resistant prostate cancer which cannot be cured by current conventional therapies of any type (Dehm et al, 2008; Wen et al, 2000). Therefore, AR is considered as a good target to develop therapies for aggressive prostate cancer.

The androgen receptor is a nuclear transcription factor and can translocate into the nuclear compartment to induce target gene expression in response to androgen stimulation. Also, the levels of androgen and AR are capable of regulating the AR signaling activation (Waltering et al, 2009). A time-dependent and dose-dependent AR nuclear translocation was observed using N&B analysis after the induction of DHT. The dynamic rate of AR nuclear translocation was slower for the lower concentration of androgen. Also, AR transcriptional activation was correlative to its phosphorylation status, and Ser-81 and Ser-650 phosphorylation sites were investigate in this work. The results showed that DAB2IP is capable of blocking AR nuclear translocation which could result in the inhibition of AR transcriptional activity. However, DAB2IP failed to block ARS81D (the highest stoichiometric phosphorylation mutant) translocation into the nuclear compartment in the presence or absence of DHT. In addition, though the phosphorylation site Ser-650 is known to be important for nuclear export, both

AR650D and AR650A mutants were not responsive to the treatment with DHT in this study. Therefore the effect of DAB2IP on the phosphorylation site Ser-650 remains unknown.

CHAPTER 4

THE ROLE OF DAB2IP IN RADIATION THERAPY

4.1 Background and Significance

Radiation therapy is a non-invasive and well-tolerated treatment modality for non-metastatic prostate cancer (Kaprealian et al, 2012; Schmitz et al, 2010). However, radiation-resistant prostate cancers frequently occur after radiotherapy, or radio-recurrent prostate cancers repopulate irradiation sites (Thompson et al, 2009). Therefore, clinical evidence shows that radiation therapy in combination with other treatments, such as ADT, or gene therapy could enhance the efficiency of therapy and antitumor activity (D'Amico, 2002; Freytag et al, 2003). Also, a clinical study showed that patients undergoing a combined treatment of ADT and radiotherapy had longer survival than those undergoing radiotherapy alone (Bolla et al, 2010). In addition, previous studies show that loss of DAB2IP in prostate cancer cells results in resistance to ionizing radiation because of a robust G_2-M cell cycle checkpoint, faster DNA DSB repair kinetics and the resistance of IR-inducted apoptosis (Kong et al, 2010b). Conversely, prostate cancer cells expressing DAB2IP become radiosensitive due to slower DNA DSB repair kinetics and have augmented IR-induced apoptosis (Kong et al, 2010b). According to these observations, DAB2IP may be involved in DNA repair pathways, and loss of DAB2IP can be a predictive biomarker for radio-resistant prostate tumors. DAB2IP may not only have a possible use as a biomarker to stratify patients for appropriate therapy, but also be a potential target for gene therapy.

However, whether DAB2IP may function as an inhibitor in DNA repair pathways remains unknown. Much attention has been attracted to investigate this mechanism due to new approach for cancer research, which entails that the status of DNA damage response of tumors can be considered as a tool to stratify patients for appropriate treatment (Curtin, 2012). Either

up-regulated expression, or epigenetic silencing of DNA damage response genes in DNA repair pathways commonly occurs in tumors (Lee et al, 2007; Liu et al, 2008), which may cause resistance to radiotherapy, or chemotherapy (Abbotts & Madhusudan, 2010). To enhance the efficiency of therapy and expand the range of tumor types, the identification of DNA damage response defects or hyperactivity in tumors is utilized to select the appropriate inhibitors in combination with radiotherapy. Moreover, cancer cells with a dysfunction in certain DNA damage responses can have alternative compensatory DNA repair pathways for survival upon radiotherapy. Based on this observation, a new approach, synthetic lethality, is exploited to selectively kill cancer cells with certain molecular defects in DNA repair pathways by combining the therapy with appropriate cDNA repair-inhibiting drugs (Bryant et al, 2005; Curtin, 2012; Patel et al, 2011). For instance, a previous study shows that poly (ADP-ribose) polymerase (PARP1), which plays a critical role in base excision repair, was inhibited by an inhibitor, PARPi, that was only toxic to homologous recombination repair (HRR) deficient tumor cells (Farmer et al, 2005). These observations strongly suggest that identification of the DNA repair pathway in which DAB2IP is involved is extremely important. The use of the DAB2IP, as an inhibitor in DNA repair, in combination with radiotherapy or chemotherapy could possibly be applied in various types of tumors with corresponding molecular defects to further enhance antitumor activity.

4.2 Results and Discussion

4.2.1 Increased DAB2IP Expression Inhibits Irradiation-Induced Autophagy

Recent studies show that the inhibition of autophagy-related genes in resistant cancer cells sensitizes these cells to radiation (Apel et al, 2008; Bae & Guan, 2011). Autophagy, a catabolic mechanism, causes the degradation of potentially damaged organelles and toxic proteins under cellular stress, such as long-term nutrient deprivation (Ogier-Denis & Codogno, 2003). Some recent results also reveal that autophagy can prevent cancer cells from death

through the inhibition of apoptosis (Apel et al, 2008; Gonzalez-Polo et al, 2005; Hippert et al, 2006). In a previous study it has been shown that DAB2IP over-expression in prostate cancer cells can result in the induction to apoptosis (Kong et al, 2010b). On the basis of these observations, the question of whether DAB2IP overexpression in prostate cancer cells is correlated with IR-induced autophagy has attracted a lot of attention. Furthermore, a recent study shows that the inhibition of DNA-dependent protein kinase catalytic subunit (DNA-PKcs), of vital role in non-homologous end joining (NHEJ) pathway of DNA repair, can induce massive autophagic cell death after radiation treatment (Daido et al, 2005). In this work, the levels of autophagy in C4-2 cell sublines, C4-2 Neo and C4-2 D2 after combining radiation treatment with or without NU7441, an inhibitor of DNA-PKcs, were determined by staining autophagosomes, acidic vacuoles, with acridine orange and observed by confocal microscopy. The results showed that DAB2IP over-expression in C4-2 cells could suppress IR-induced autophagy and DNA-PKcs-associated autophagy (Fig. 4.1). Moreover, survival fraction analysis from Dr. Saha's lab revealed that NU7441 can cause radioresistant prostate cancer cells (DAB2IP-deficient cells) to be more sensitive to radiation due to delayed DNA DSB repair, and the combination of DAB2IP and NU7441 can further sensitize cells to IR-induced cell death due to inhibition of autophagy (Yu et al, 2012). These novel findings strongly suggest that to investigate the mechanism by which DAB2IP may function as a DNA repair inhibitor can be significant for the improvement of future treatments.

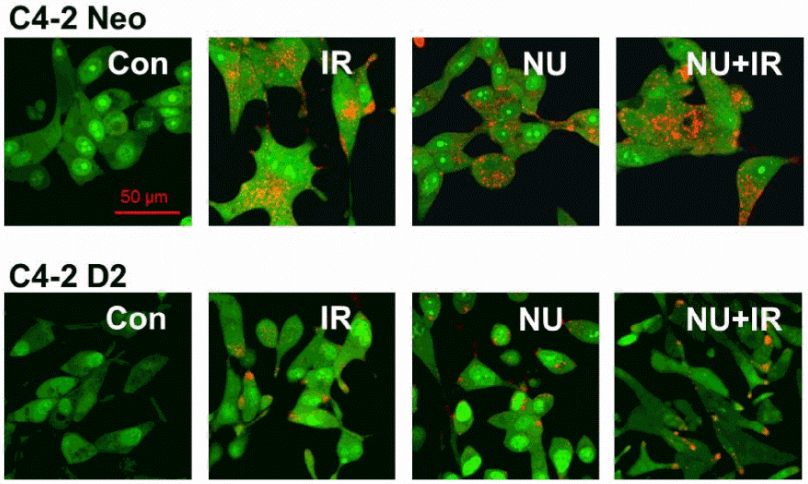

Figure 4.1 The levels of autophagy in C4-2 D2 and Neo cells.

C4-2 D2 and Neo cells were treated with NU7441 (1 µM), IR and IR in combination with NU7441. Then, autophagosomes were stained with acridine orange and observed by confocal microscopy.

4.2.2 Increased DAB2IP Expression Enhances Radiosensitivity

In a previous study it has been shown that DAB2IP-deficient prostate cancer cells, such as PC-3 shDAB2IP, have increased resistance in response to ionizing radiation treatment and faster DNA DSB repair kinetics (Kong et al, 2010b). Due to high-efficiency transfection, HEK 293 cells were used as a study model in this work. However, whether over-expression of DAB2IP in HEK 293 cells also causes radiosensitivity was not verified. To test this assumption, HEK 293 cells expressing DAB2IP or pCDNA construct were irradiated with 2, 4, 6 and 8 Gy and then maintained in 5% CO_2 incubator for 14 days. Colonies (> 50 cells) were counted after 14 days and survival curves were fitted using a linear-quadratic algorithm by the program GraphPad Prism (GraphPad Software, La Jolla, CA). Compared to control cells expressing pCDNA (a control vector), DAB2IP over-expression in HEK 293 cells (293-DAB2IP) sensitized cells to IR-induced cell death (Fig. 14). The survival fractions at 2 Gy for 293-DAB2IP and 293-pCDNA cells were 0.12±0.038 and 0.27±0.066, respectively (Fig.4.2). On the basis of this result,

HEK 293 cells were exploited to investigate the functional role of DAB2IP in response to radiation.

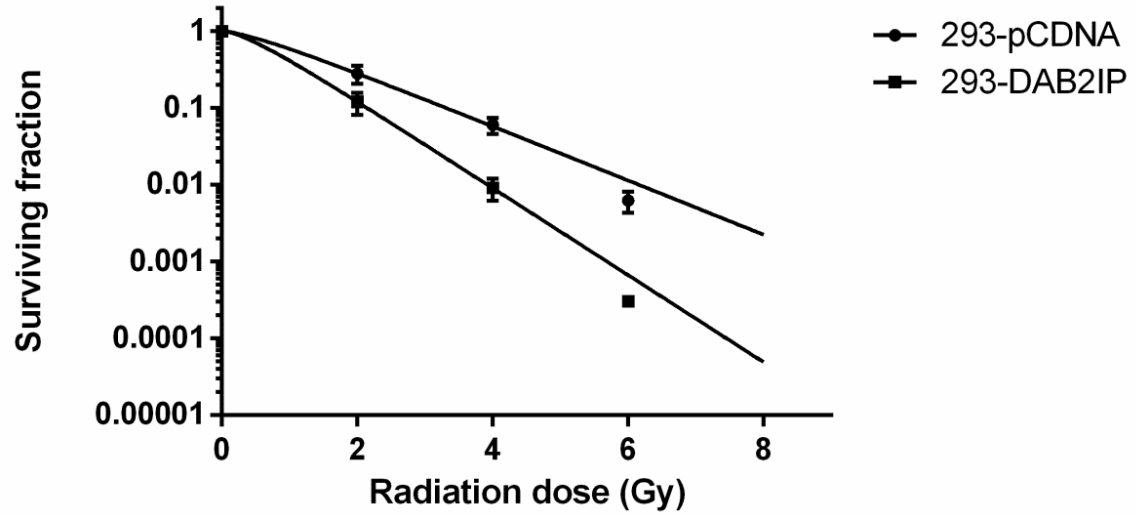

Figure 4.2 Survival fraction analysis for 293-DAB2IP and 293-pCDNA cells.

Cells were irradiated with 2, 4, 6 and 8 Gy and then maintained in 5% CO_2 incubator for 14 days. Colonies (> 50 cells) were counted after 14 days and survival curves were fitted by using a linear-quadratic algorithm.

4.2.3 Co-localization of DAB2IP and γH2AX

A previous report suggests that loss of DAB2IP result in radioresistance in both prostate cancer and normal prostate epithelial cells (Kong et al, 2010a; Kong et al, 2010b). However, whether DAB2IP was directly relocated at DNA DSB sites remains unknown. To address this issue, immunofluorescence staining was performed to investigate whether DAB2IP was relocated at γH2AX foci. Previous reports have shown that histone H2A.x+ (H2AX) phosphorylation on serine 139 is primarily mediated by Ataxia telangiectasia mutated (ATM), serine/threonine protein kinase, in response to DSB formation (Kastan & Lim, 2000; Rogakou et al, 1998). Upon radiation treatment, γH2AX is relocated at nuclear foci, DNA DSB sites, which

results in repair proteins encompassing a DNA DSB site by attracting repair factors (Kouzarides, 2007; Paull et al, 2000; Ward et al, 2003). In this work, after radiation treatment (5 Gy), C4-2 D2 cells were immunostained for γH2AX and DAB2IP and collected at various times post-irradiation to investigate the co-localization of DAB2IP and γH2AX (Fig.4.3). However, the co-localization of DAB2IP and γH2AX was not observed either before or after IR treatment shown as in Fig. 4.3. This result indicated that DAB2IP may not be directly involved in DNA damage response at the sites of DNA DSBs.

HR and NHEJ both play important roles for DNA DSB repair. A previous report showed that NHEJ repair is faster than HR (Mao et al, 2008). The process of NHEJ repair is completed in approximately 30 min, and the process of HRR is completed in around 7 hours or even longer (Mao et al, 2008). The accumulation of DAB2IP surrounding the sites of DNA DSB may take longer than 1 hour. Therefore, the formation of DAB2IP foci in C4-2 D2 cells was investigated at various times, from 0 hours to 2 hours post IR-induction. However, the result showed that the formation of DAB2IP foci was not observed at any time post IR-induction (Fig. 4.4). In addition, the subcellular distribution of DAB2IP in C4-2 D2 cells is different to that in PC-3 cells (Fig. 4.4). The majority of DAB2IP was located in the cytosol of C4-2 D2 cells, but DAB2IP was homogenously distributed in PC-3 cells. Furthermore, C4-2 D2 and PC-3 cells expressed exogenous DAB2IP (rat-species) and endogenous DAB2IP (human-species), respectively. The formation of DAB2IP foci in PC-3 cells was also investigated at various times post-irradiation. However, there were no DAB2IP foci observed in PC-3 cells. No conclusions can be drawn regarding the role of DAB2IP in DNA repair form these observations.

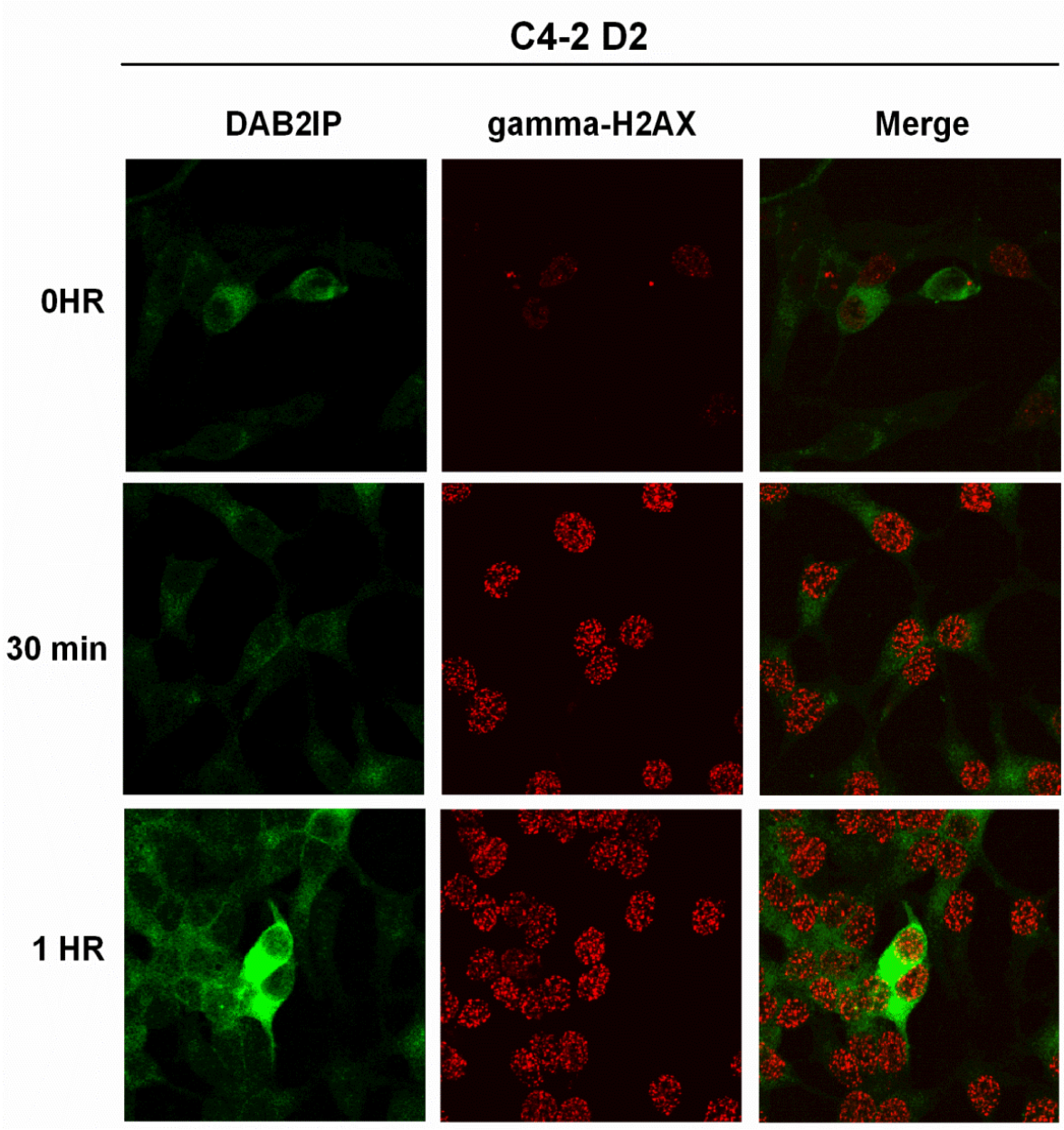

Figure 4.3 The accumulation of DAB2IP at γH2AX foci.

C4-2 D2 cells were irradiated with 5 Gy, and then collected at various times as indicated. Samples were immunostained for DAB2IP (green, FITC) and for γH2AX (red, Rodhamine-Tex-X).

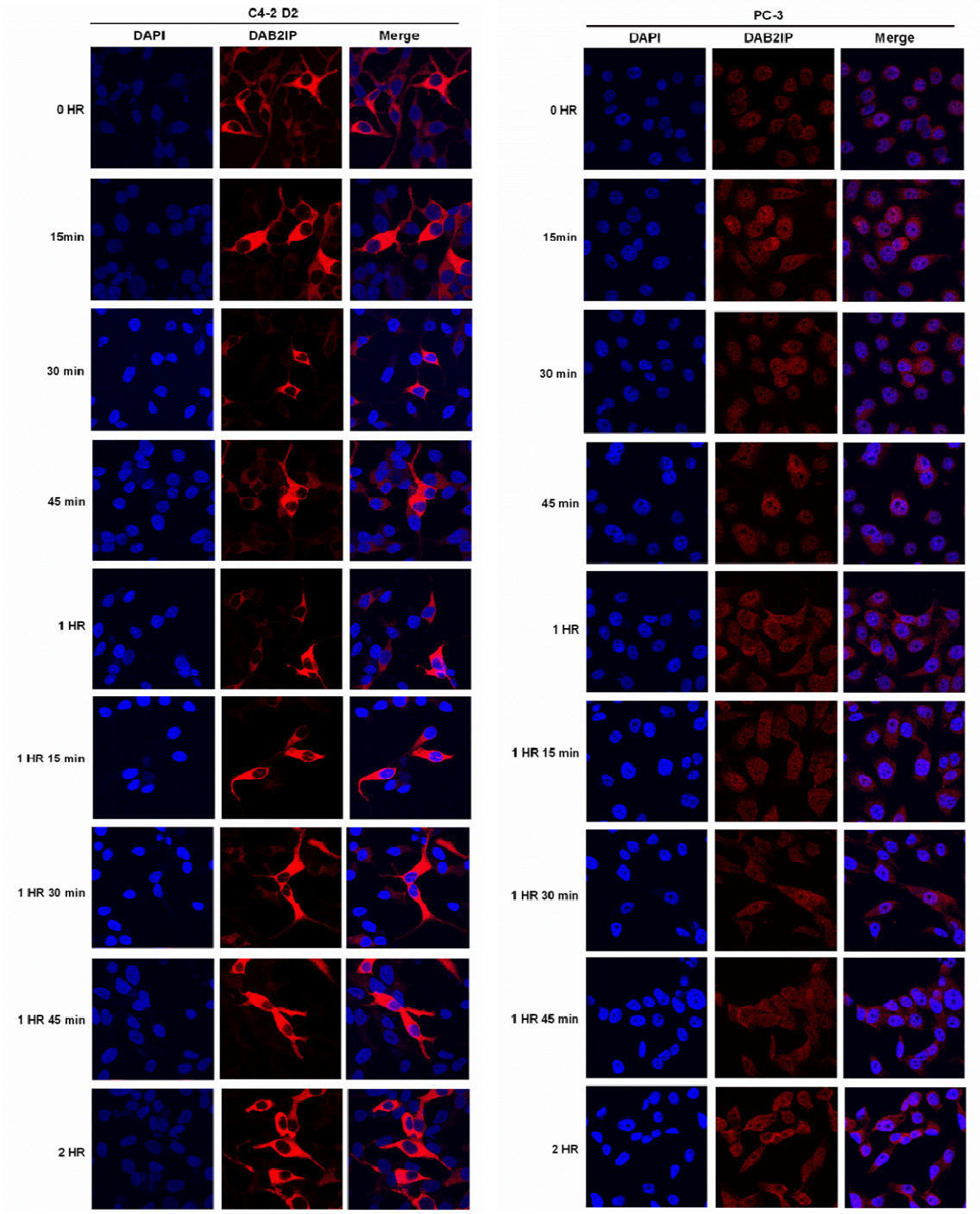

Figure 4.4 The formation of DAB2IP foci.

C4-2 D and PC-3 cells were irradiated with 5 Gy and collected at different times post-irradiation as indicated. Samples were immunostained for DAB2IP (red, Alexa 594).

4.2.4 Functionality and Subcellular Localization of Skp2 Chimeric Protein

Although the fact that DAB2IP did not relocate at the sites of DNA DSB has been verified, how DAB2IP functions in DNA repair pathway upon IR treatment remains unclear. Quantitative kinetics of DAB2IP in response to IR induction can be investigated by N&B and RICS analysis. To quantify kinetics of DAB2IP after irradiation, DAB2IP was tagged with a fluorescent protein as a probe. The fluorophore tag used was EGFP or PAGFP (section 2.3.1.1). Firstly, it was necessary to ensure that the function and localization of DAB2IP was not affected by tagging with the fluorescent protein. Western blot results showed that the molecular weight of the DAB2IP chimeras were larger than that of DAB2IP itself, by 28 kDa, and that DAB2IP chimeras could also be recognized by anti-GFP and anti-DAB2IP antibodies at the same time (Figs. 4.5A and 4.5B). Among DAB2IP chimeras, PAGFP-DAB2IP Cl5 and PAGFP-DAB2IP Cl10 were modified by mung bean nuclease to generate in-frame constructs. Mung bean nuclease can digest single strand overhangs, but it may also digest double stranded DNA when it breathes due to thermal excitations. Therefore, two constructs of PAGFP-DAB2IP chimera were simultaneously obtained after modification by Mung bean nuclease. HEK 293 cells were transiently transfected by four chimeric constructs, DAB2IP-EGFP, PAGFP-DAB2IP Cl5, PAGFP-DAB2IP Cl10 and EGFP-DAB2IP, and collected for Western blot analysis. Also, as a previous study has shown that DAB2IP can suppress the process of EMT which results in up-regulation of E-cadherin and down-regulation of vimentin (Xie et al, 2010), to exclude the influences of transfection and fluorescent protein, the EMT markers in transiently transfected cells with chimeric constructs were compared to that with control vector. The results showed that up-regulation of E-cadherin and down-regulation of vimentin occurred after induction of DAB2IP (Fig. 4.5C). Compared to the subcellular distribution of endogenous DAB2IP, the DAB2IP chimeras, flag-DAB2IP and DAB2IP-EGFP, primarily localized in cytosol (Fig. 4.6 C-D), and their subcellular localization was similar to that in most of prostate cell lines except for PC-3 and PZ-HPV-7T (Fig. 4.6 A-B). The subcellular localization of the other DAB2IP chimeras,

PAGFP-DAB2IP Cl5 and CL10 and EGFP-DAB2IP, was also similar to that of DAB2IP-EGFP (not shown).

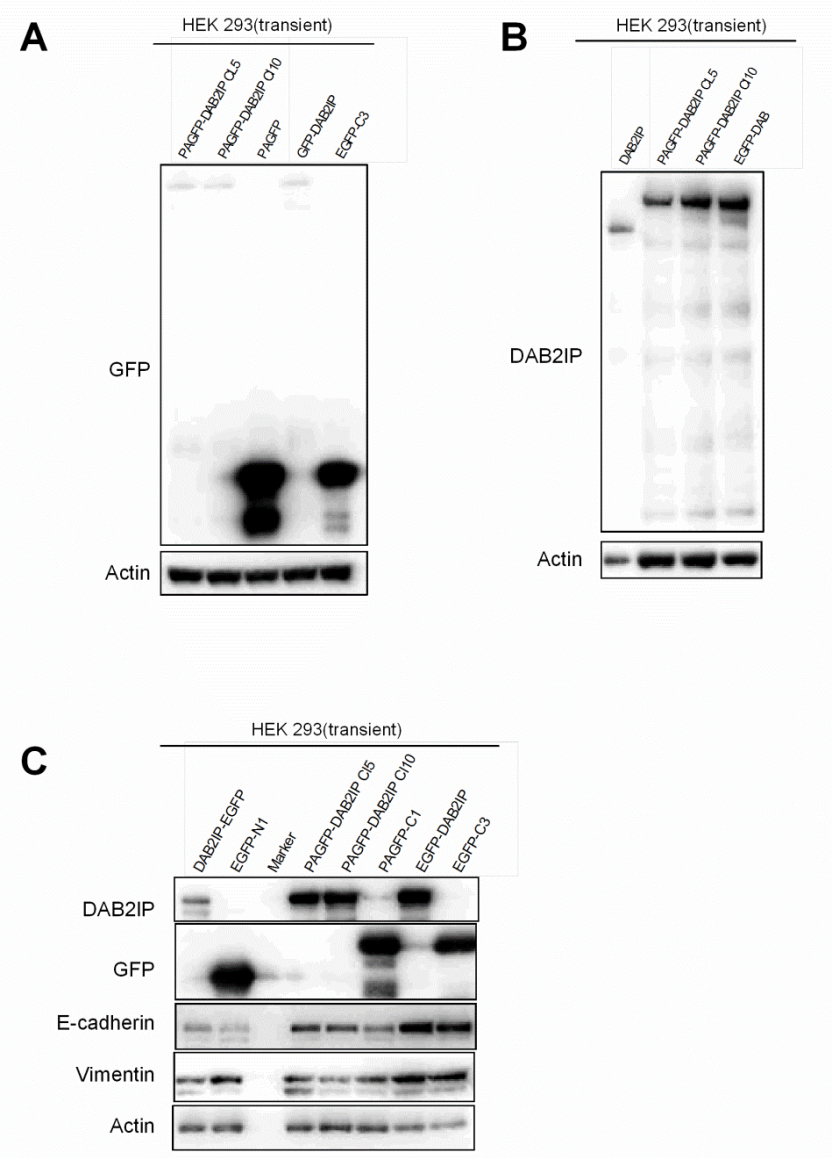

Figure 4.5 The functionality of PAGFP-DAB2IP, EGFP-DAB2IP and DAB2IP-EGFP. (A) and (B) HEK 293 cells were transiently transfected with recombinant DAB2IP constructs and harvested for Western blot analysis in order to confirm the molecular size of the DAB2IP chimera. (C) HEK 293 cells were transiently transfected with recombinant DAB2IP constructs and harvested for Western blot analysis in order to confirm the function of the DAB2IP chimera.

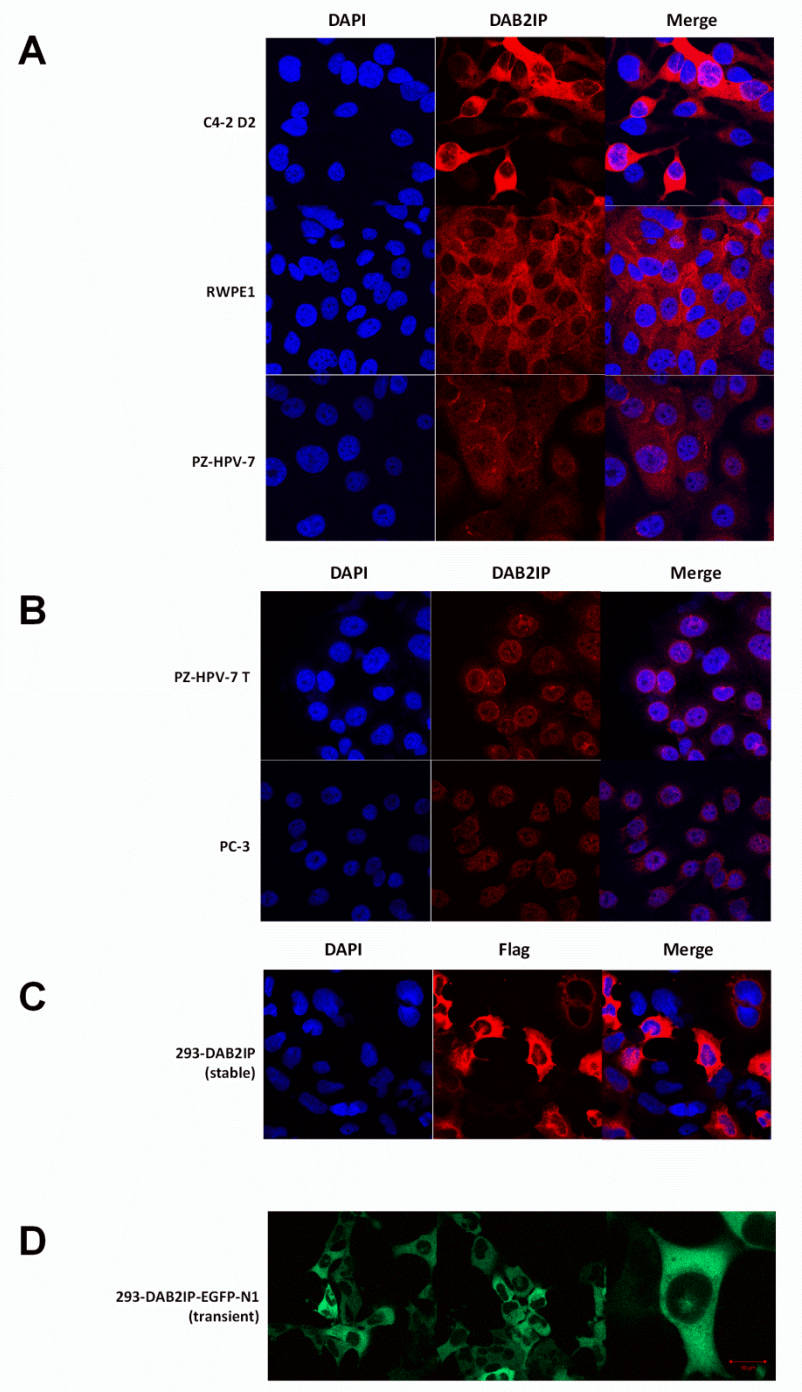

Figure 4.6 The localization of DAB2IP-EGFP in different cell lines.

(A), (B) and (C) cells, C4-2, PC-3, RWPE1, HEK 293 and PZ-HPV7 were immuno-stained for DAB2IP (red, Alexa 594). Cells were observed by confocal microscopy.

4.2.5 Kinetics of the DAB2IP Chimera upon IR Treatment

Once the functionality and localization of fluorescent fusion protein were identified as non-tagged protein, the next step was to investigate the role of DAB2IP in the response to DNA repair. To help address this issue, the nucleocytoplasmic transport of DAB2IP chimera was first observed as a function of time post-irradiation. This study was undertaken because of known examples of other proteins that are important to DNA repair that also relocate to nucleus post-irradiation. For instance, previous studies show that breast cancer 1 (BRCA 1), a nucleocytoplasmic shuttling protein (Fabbro & Henderson, 2003), is imported to nucleus by BARD1 for DNA repair (Fabbro et al, 2002; Mullan et al, 2006) and exported to the cytosol for cellular apoptosis following DNA damage (Fabbro et al, 2004). Furthermore, previous reports revealed that tumor protein 53 (p53) is rapidly imported and accumulates in the nucleus to increase its transcriptional activity through phosphorylation of its nuclear export signal domain and interaction with importin proteins in response to DNA damage (Feng et al, 2005; Marchenko et al, 2010; Zilfou & Lowe, 2009). Furthermore, cellular distribution of DAB2IP was primarily in cytoplasm of the normal cells, and then we speculate DAB2IP may be involved in DNA repair pathway through nuclear import. On the basis of these examples and observations, experiments were performed to elucidate whether regulation of subcellular localization of DAB2P may play an important function in the response to DNA damage.

In this work the regulation of subcellular localization of DAB2IP in 293-DAB2IP cells was observed after irradiation. It was found that the nuclear DAB2IP-EGFP levels were gradually increased post IR-induction and then dropped (Fig. 4.7A and 4.7B). The variance of transfection between samples may have had a critical effect here. Therefore, HEK 293 cells stably expressing DAB2IP-EGFP were established and then used to investigate the nucleocytoplasmic transportation. The trend of nuclear DAB2IP-EGFP levels in stably transfected cells was similar to that in transiently transfected cells (Fig. 4.8A and 4.8B). This result is compatible with the current assumption that DAB2IP may be involved in DNA DSB repair upon IR treatment via

nuclear transport. Moreover, nuclear DAB2IP levels were low in most of the cell lines studies (Fig. 4.6), which could cause huge variation between samples by multiple factors, such as different sample collecting times and protein degradation rates. Therefore, further experiments were needed to elucidate whether DAB2IP nucleocytoplasmic transport played an important role in response to IR treatment. To address this issue, quantitative kinetics and the concentration changes of DAB2IP were determined by confocal microscopy using RICS and N&B analysis. However, the diffusion coefficients of both DAB2IP-EGFP and EGFP obtained from RICS analysis were significantly slower than the expected free diffusion values. After troubleshooting, a lack of an emission filter in the appropriated fluorescence detection path of the Zeiss confocal microscope was found to result in the inaccuracy of the diffusion coefficient quantification. The Zeiss confocal microscopy system contains two channels for green and red probes. Unfortunately, the APD detector for the green channel was burned and there were no suitable emission filters for green probes in the red channel. Therefore, only the dichroic mirror, HFT500, was used to block the excitation light, which was inadequate. Just to demonstrate the effect that excitation light leakage could have on measurements and raster scan images were performed with or without emission filter in the fluorescence path using the Zeiss PMT channels that were not suitable for RICS is shown in Fig. 4.9. As a result, a two-photon system that was built in Dr. Alexandrakis' lab was used for RICS and N&B analysis in all subsequent work.

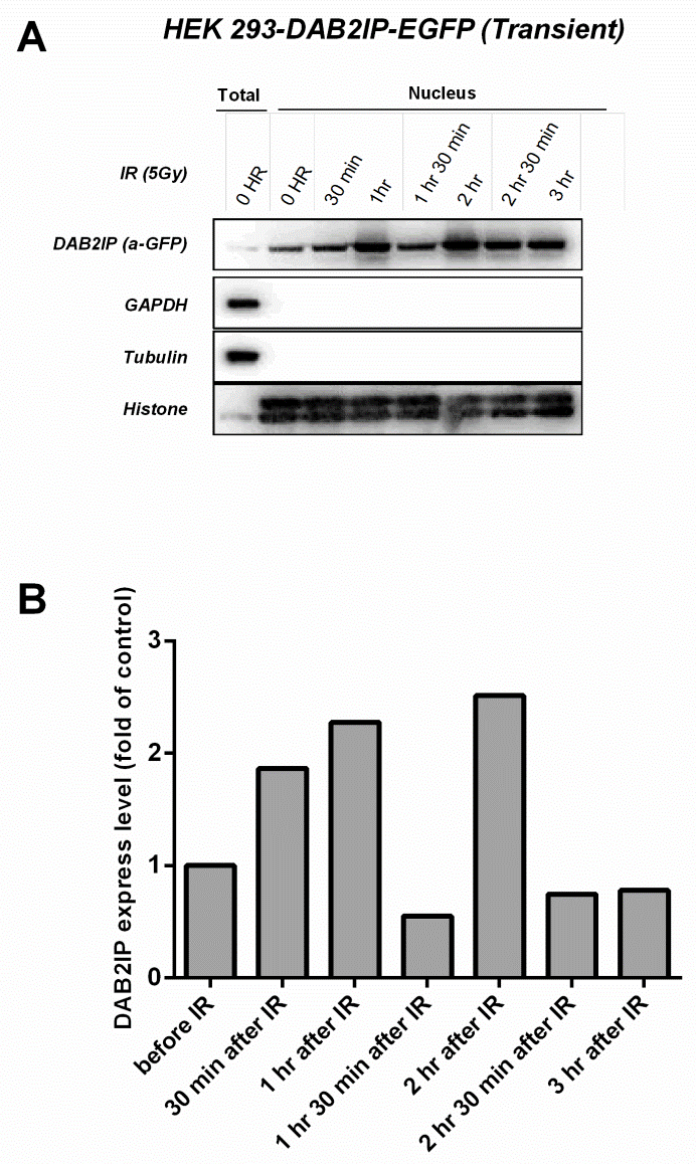

Figure 4.7 Subcellular localization of DAB2IP-EGFP upon IR treatment.

(A) HEK 293 cells were transfected with chimeric DAB2IP construct, and then irradiated with 5 Gy. Samples were collected at various times post-irradiation as indicated. (B) The bar graph represents the Western blot results (A).

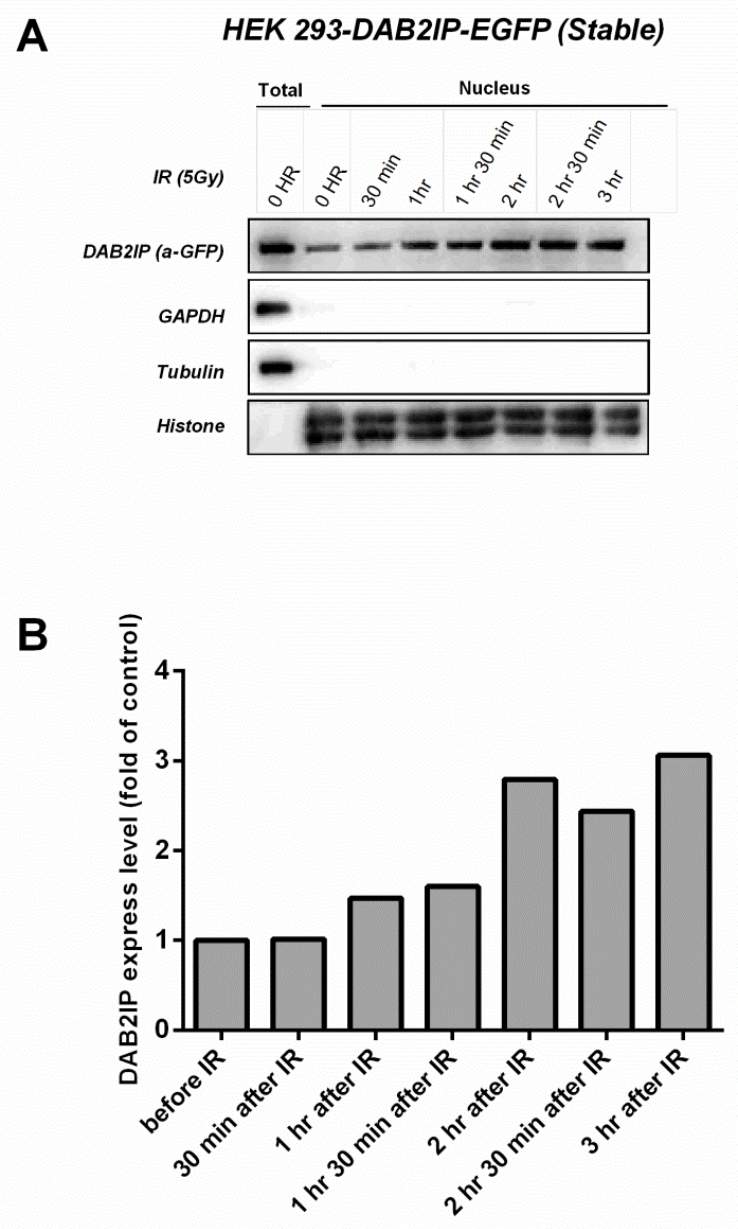

Figure 4.8 Subcellular localization of DAB2IP-EGFP (HEK 293 stable clone) upon IR treatment. (A) HEK 293 cells stably expressing DAB2IP-EGFP were irradiated with 5 Gy. Samples were collected at various times post-irradiation as indicated. (B) The bar graph represents the Western blot results (A).

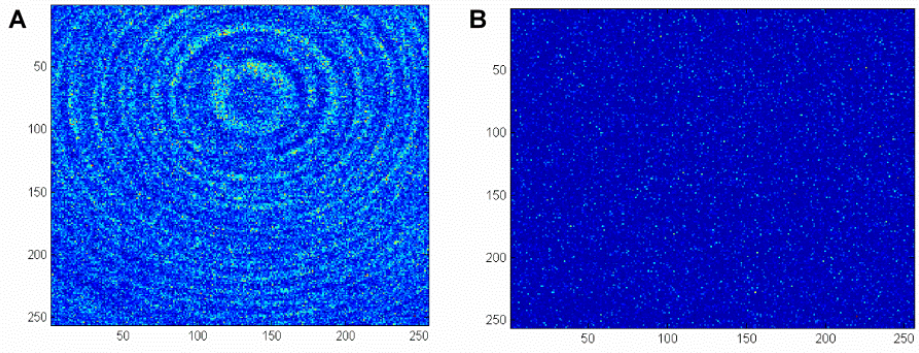

Figure 4.9 The effect of the emission filter on raster scan images.

The image of excitation light (A) without an emission filter and (B) with the emission filter, BP505-530, in place.

4.3 Conclusion

Upon IR treatment, DAB2IP may function as an inhibitor in DNA repair pathways or associate with the genes in response to radioresistance, causing slower DNA DSB repair kinetics and induction of apoptosis (Kong et al, 2010b). Autophagy is a mechanism by which tumor cells can skip cellular death resulting from cellular stress (Apel et al, 2008; Hippert et al, 2006). The results of this work show that DAB2IP can suppress radiation-induced autophagy in order to increase the radiosensitivity of cells. DAB2IP in combination with NU7441 can further enhance antitumor activity due to suppression of autophagy and slower DNA DSB repair kinetics. Although DAB2IP causes slower DNA DSB repair kinetics upon IR treatment, the mechanism is still unclear. In an attempt to help shed some light on this mechanism, the co-localization of DAB2IP and γH2AX was studied. However, no co-localization was observed which indicates that DAB2IP may not be directly recruited at DNA DSB sites in response to IR treatment. As some important cell survival proteins, such as p53 and BRCA1, can be responsive to DNA repair by nucleocytoplasmic transport (Fabbro et al, 2002; Feng et al, 2005), it was investigated whether DAB2IP nucleocytoplasmic transportation occurred post-irradiation by Western blot analysis. However, it was found that upon IR treatment, nuclear DAB2IP-EGFP

levels gradually increased (Figs. 4.7 and 4.8). Additional efforts using confocal RICS for verifying that the expressed tagged proteins were mobile and had the expected diffusion coefficients did not succeed due to a hardware issue with the Zeiss confocal microscope that could not be repaired.

CHAPTER 5

A METHOD FOR IMPROVED QUANTIFICATION OF A PROTEIN'S DIFFUSION COEFFICIENT BY CONTROL OF FLUORESCENT PROTEIN CONCENTRATION THROUGH PHOTOACTIVATION

5.1 Background and Significance

Quantification of molecular kinetic parameters in living cells by fluorescence fluctuation spectroscopy methods, such as FCS (Bacia & Schwille, 2003), RICS (Digman et al, 2005), and N&B analysis (Digman et al, 2008) requires relatively tight control of fluorescently tagged protein expression levels. This is because the accuracy of the measured molecular kinetic properties depends on how large the measured signal fluctuation amplitude, is compared to sources of background noise (Kim et al, 2010). At low (pM) concentrations the cellular autofluorescence background and detection system noise overwhelm the fluorescence fluctuation signal, whereas at high (> 500 nM) concentrations the amplitude of fluorescence fluctuations becomes very small due to the inverse relation between signal fluctuation amplitude and molecular concentration (Haustein & Schwille, 2007; Kim et al, 2010). Another challenge for quantitative measurement of molecular kinetic parameters in cells, such as a protein's diffusion coefficient, is the presence of an immobile protein fraction that can mask the fluorescence fluctuation signal of the protein's mobile fraction, especially when this protein is expressed at high concentrations. Mitigation approaches include pre-bleaching of a selected area of the cell (Zhou et al, 2012), or the subtraction of the estimated fraction of the contribution of the mobile background to the total fluorescence fluctuation signal (Brown et al, 2008). Nevertheless, both of these approaches have not been successful at completely removing the immobile background signal and as a result the reported molecular diffusion coefficients for the same protein vary between studies. For example, though a commonly reported value for EGFP in

cells is 23.5 $\mu m^2/s$ which is 4 times lower than the free solution value presumably due to the higher crowding in the cell environment (Chen et al, 2002), other studies have reported values up to a factor of 10 lower than the free solution value (Schwille et al, 1999).

In order for fluorescence fluctuation measurements to not be significantly biased by unsuitably low or high protein expression levels or by a high immobile fraction, the protein expression levels at the time of the measurement need to be controlled. For transient transfections this is typically done by selecting the time window post-transfection to make the experiments, which however can be narrow (few hrs) before molecular concentration exceeds the upper bound for accurate quantification (Kim et al, 2010). It may be possible to select cells with lower transient expression levels so that the time window during which the expression levels are not too high is longer (many hrs to days).In addition, an increasing concentration fraction of the expressed protein may cause more molecular crowding and increase the possibility of nonspecifically interaction with immobile partner, such as microtubule that can mask quantification of kinetics for the mobile fraction (Dauty & Verkman, 2004; Dauty & Verkman, 2005). On the other hand, one could create a stable expression line and select a clone with expression levels the appropriate concentration range. However, stable expression cell lines take weeks to create, and it takes even longer to select a clone with appropriate expression levels. Furthermore, there is ample time for a significant immobile fraction to build up over time in the stable clones.

In this work, a photoactivatable variant of GFP (PA-GFP) (Patterson & Lippincott-Schwartz, 2002) was used as part of a proposed experimental protocol for tuning the fluorescent protein concentration at optimal levels for fluorescence fluctuation measurements while also circumventing the immobile fraction problem both for transient transfections and stable clones. The capacity of this protocol to resolve the immobile fraction issue and obtain consistent diffusion coefficient values, as quantified by RICS, is demonstrated in both transiently transfected and stable lines expressing PA-GFP. Comparisons are made with corresponding

cells expressing EGFP to show the advantages of this method. Further comparisons are made for a protein important to metastatic prostate cancer progression, namely Skp2 (Yang et al, 2002), that was transiently expressed as a fusion protein with both PA-GFP and EGFP. Concurrent concentration measurements by N&B analysis (Digman et al, 2008) enabled identifying the optimal concentration range for accurate diffusion coefficient quantification for both PA-GFP and PA-GFP-Skp2. The photoactivation protocol presented here can be applied to the optimal quantification of the diffusion coefficient of any protein of interest.

5.2 Results and Discussion

5.2.1 Choosing the Photoactivated Protein Concentration and Fluorescence Excitation Power for Optimal Quantification of the Molecular Diffusion Coefficient

The expression level of exogenous protein can vary by a few orders of magnitude in transiently transfected lines depending on the transfection dosage and the timing of the measurement post-transfection. Significant variations in concentration can also occur between different clones of a stably transfected cell line. In this work the variation of fluorescent protein concentration in the cell was simulated by increasing the photoactivated PA-GFP concentration in the cell in a step-wise manner by repeatedly scanning over a selected ROI as described in the Methods (Section 2.8.2) at a fixed photoactivation laser power of 2 mW at 765 nm. At each step the PA-GFP number density (number/pixel) was determined by N&B analysis. Number density could be converted to protein concentration expressed in nM as described in Methods Section 2.8.3 This way the protein concentration in each cell was tuned to 0-4.5, 4.6-10.5, 10.6-23, 23.1-36.5 and 36.6 molecules per pixel, or equivalently 41, 139, 310, 644 and 779 nM for a calibrated focal volume (Methods 2.8.1) of about 0.09 fl.. Therefore the range of concentration values explored by photoactivation spanned the range where RICS measurements are possible. The above five concentration values were chosen such that they produced 100, 300, 500, 700

and 900×10^3 counts per second (cps), respectively, at the detector. The lower bound of these count rates was set to exceed the background count rate for PA-GFP transfected HEK 293 cells, which was ~50 x 10^3 cps. The background count in this case was high because PA-GFP emits very weak fluorescence even in its 'non-photoactivated' form (Patterson & Lippincott-Schwartz, 2004). The upper bound was set by the saturation limit of the detector which was ~1.2M cps. The protein diffusion coefficient was determined by RICS analysis (Methods 2.8.3) of the exact same data set acquired for N&B analysis at each protein concentration level before the subsequent photoactivation and the analysis procedure was repeated for the new concentration.

Once the five target protein concentrations, reached sequentially after each photoactivation step, were set the next question to be answered was whether the level excitation power during the subsequent RICS measurements also affected the accuracy of the deduced diffusion coefficient. To address this question RICS experiments were performed at five different excitation powers (8, 9, 10 and 11 mW). For each excitation power, 5-10 cells were used for RICS measurements, and results were fit to a one-component diffusion model (Eqs. 8, 9 and 10). Corresponding fits of the same data to a two-component model, did not yield a significant second component. At low excitation powers the fluorescence signal amplitude was not much larger from background noise contributions that degraded the quality of autocorrelation profiles and resulted in slower apparent diffusion coefficients. This was especially evident in the lowest and highest concentration categories of Fig. 5.1A, where the signal amplitude was minimal due to not enough signal (low case) or due to the autocorrelation amplitude being small and noisy (high case). As the background signal from the 'non-photoactivated' PA-GFP emitted much more weakly than the photoactivated species, the diffusion coefficient was determined more accurately for higher excitation powers (Figs. 5.1C-D). Nevertheless, at the highest excitation power of 11 mW (Fig. 5.1D) it was found that the high-powered laser caused significant unintended photoactivation (Fig. 5.1E). Therefore these

studies indicated that for our instrument an excitation power in the vicinity of 10 mW was optimal for accurate quantification of the diffusion coefficient. Most importantly, for any excitation power photoactivatable concentration could be gradually tuned until it reached the middle of the optimal concentration range which was in the vicinity of 300 nM (10.6-23 per pixel).

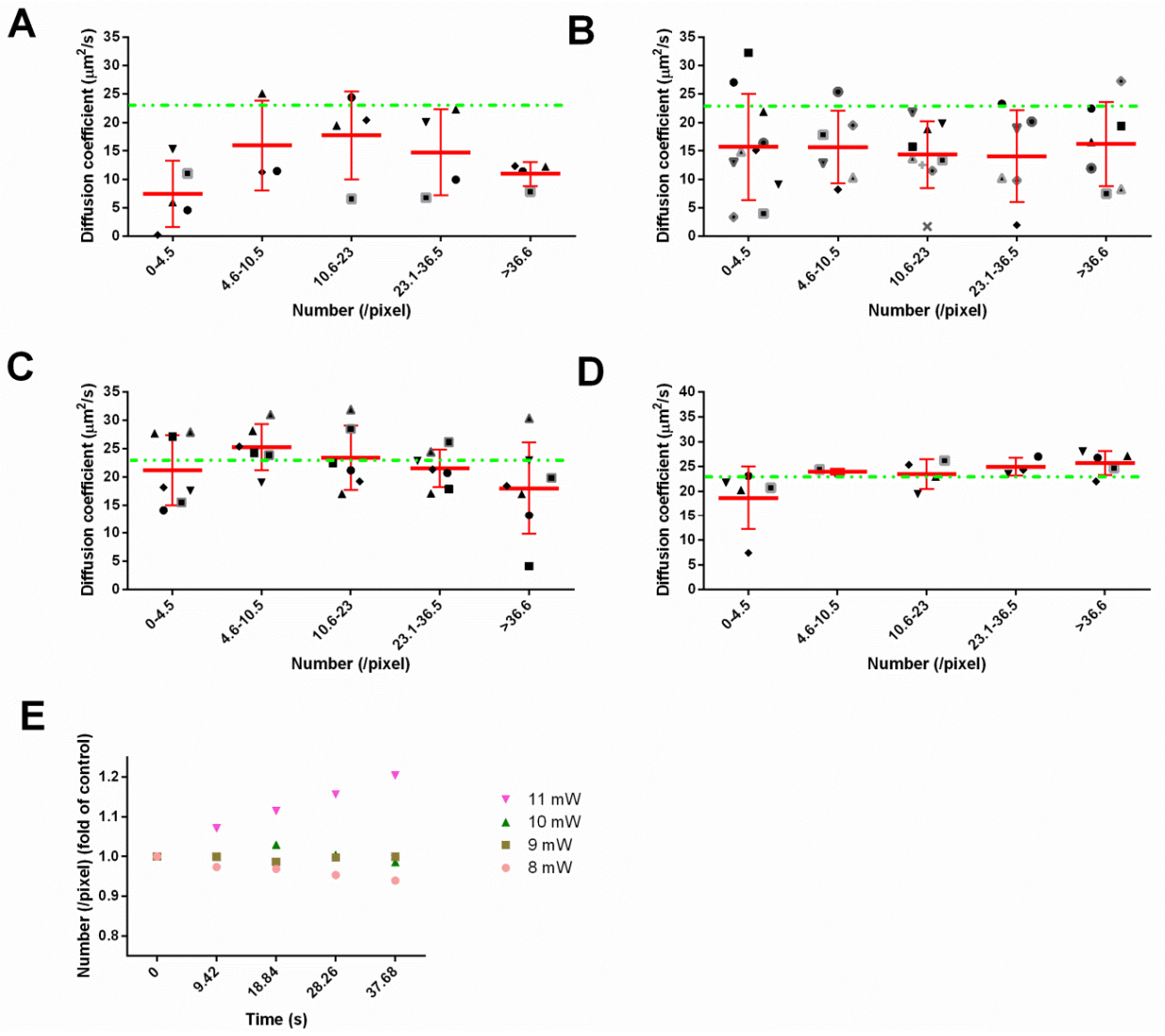

Figure 5.1 Laser power series (A)-(D). PA-GFP stably expressed HEK 293 cells were used to monitor the relationship of diffusion coefficient with laser power and a wide range of molecular

concentrations (number per pixel). The diffusion coefficients were calculated at the target ranges of molecule number per pixel for each average laser power, 8 mW (A), 9 mW (B), 10 mW (C) and 11 mW (D). Each symbol represents an individual cell and each cell was measured 5 times from low molecular concentration (number per pixel) to high. The green dotted line depicts the estimated diffusion value, 23.5$\mu m^2/s$, and error bars represent the standard deviation of 5~10 cell measurements at each concentration. (E) For a 50-frame RICS measurement, each molecular concentration (number per pixel) from 10-consecutive image frames (~9.42 s) was determined using N&B analysis in order to demonstrate if molecular number density was constant throughout the measurement at each excitation power.

5.2.2 A Comparison of Diffusion Coefficient between EGFP and PAGFP

Once an optimal excitation power for accurate diffusion coefficient quantification was identified, the next step was to compare results from cells expressing PA-GFP to cells expressing EGFP. These cells were measured using RICS at 12, 16, 20 and 24 hours post-transfection with an average laser power at focal plane of about 10 mW (Fig. 5.2). Over 30% of cells expressing PA-GFP was initiated at 12 hours post-transfection according to pilot experiments, and therefore RICS experiments were initially performed at this time. For these measurements the number of activated PA-GFP molecules in the focal volume was set in the range of 10.6-23 (number per pixel) based on the previously described incremental process, which brought the fluorophore concentration near the optimal rage. The measured average diffusion coefficients of PA-GFP measured on a number of cells, n, at various times post-transfection indicated by the corresponding subscripts were as follows: (D_{P12hr} =22.4 ± 2.33 $\mu m^2/s$, n=14; D_{P16hr} =21.2 ± 4.67 $\mu m^2/s$, n=12; D_{P20hr} =24.4 ± 4.51 $\mu m^2/s$, n=11; D_{P24hr} =22.8 ± 5.99 $\mu m^2/s$, n=11). These diffusion coefficient values were comparable to those reported in prior work (Chen et al, 2002). The expected estimated value for the PA-GFP diffusion coefficient calculated from the hydrodynamic radius was 2.8 nm (Dill et al, 2011; Kalwarczyk et al, 2012)

and is also indicated as a flat line in Fig 5.2A. In contrast, the diffusion coefficients determined from the EGFP cells had consistently lower diffusion values by ~30%and were in the vicinity of 23 μm^2 /s, as also shown in Fig. 5.2A. When differences in the mean values for 10 cell measurements were compared pair wise for the different measurement time points, significant differences were found for 12, 20 and 24 hours post-transfection, as shown in Fig. 5.2B. Furthermore the determined diffusion coefficient variances were more uniform for the case of PA-GFP compared to EGFP. Specifically, the variances of the determined diffusion coefficients between the different time points were not significantly different for the case of PA-GFP as proven by ANOVA analysis ($F_{[3,44]}$ = 1.01; p=0.3968). In contrast, the variances of the average diffusion coefficient in EGFP post-transfection measurements were significantly different ($F_{[3,60]}$=2.801;p=0.0475). In comparison to PA-GFP, the diffusion coefficients of EGFP at various times post-transfection indicated by the corresponding subscripts were as follows: (D_{E12hr} =14.8 ± 5.32 μm^2/s, n=15; D_{E16hr} =18.1 ± 4.62 μm^2/s, n=16; D_{E20hr} =16.5 ± 3.26 μm^2/s, n=18; D_{E24hr} =14.0 ± 3.88 μm^2/s, n=15). These diffusion coefficient values were 30% lower than the PA-GFP case with the exception of the 16 hours post-transfection that did not have a statistical difference. The variance of diffusion coefficient is reduced in EGFP measurements due to differences in its expression levels from cell to cell. On the other hand, the variance of diffusion coefficient in PA-GFP measurements can be enhanced by optimizing the concentration of photoactivated PA-GFP despite differences in PA-GFP expression levels among cells. Therefore not only the accuracy of the determined coefficient was improved, but also the variance of results became more uniform using the incremental photoactivation method.

5.2.3 Functionality and Subcellular Localization of Skp2 Chimeric Protein

To test that the proposed incremental photoactivation method does not only improve the diffusion coefficient of the PA-GFP fluorophore itself, but also of a protein tagged to that fluorophore, we performed RICS and N&B measurements in cells expressing the PAGFP-Skp2

oncogene protein. In PAGFP-Skp2 construction, the Skp2 coding sequence was excised out of a XP-Skp2 construct (Lin et al, 2009) and inserted into the pPAGFP-c1 plasmid, as described in detail in Methods 2.3.1.2 and shown schematically in Fig. 5.3A. Before studying the diffusive mobility of the PA-GFP-Skp2 chimera protein, we had to demonstrate that this fluorescent fusion protein maintained the localization and functionality of unmodified protein (Snapp, 2005). Therefore, the cellular distribution of fluorescent fusion protein was compared with untagged protein using immunofluorescence and confocal fluorescence imaging (Fig. 5.3B). The majority of Skp2 protein was localized in the nucleus in both cases as was intended, and the subcellular distribution of PAGFP-Skp2 was similar to that of the XP-Skp2 chimeric protein. Skp2 is a member of F-box formed SCF complex with cullin-1 and Skp1 for ubiquitylation which is required for ubiquitin-mediated degradation of cyclin-dependent kinase inhibitor 1B (p27) (Carrano et al, 1999), and thence the degradation of p27 is indicated as a function of Skp2. A dose-dependent reduction of p27 expression level was observed with increasing amount of PAGFP-Skp2 plasmid (Fig. 5.3C), which is consistent with its known biological function. The expression levels of p27 in PA-GFP transiently transfected cells and XP-Skp2 transiently transfected cells were considered as baseline and positive control, respectively (Fig. 5.3C).

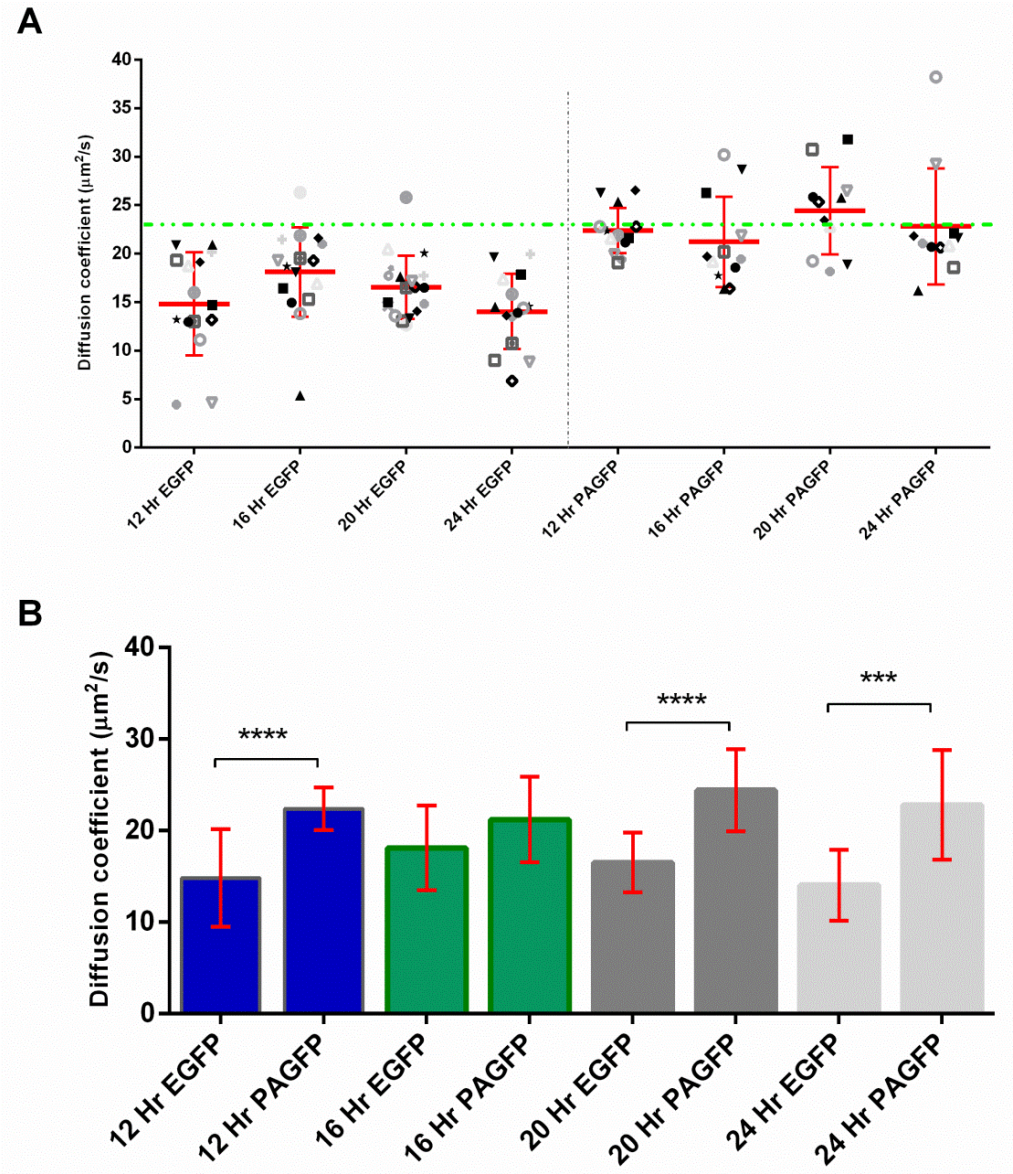

Figure 5.2 A comparison of diffusion coefficients between EGFP and PA-GFP.

(A) HEK 293 cells were transiently transfected with the EGFP or PA-GFP plasmid and the diffusion coefficient was measured at 12, 16, 20, 24 hours post-transfection. Each data point represents an independent measurement at the different individual cell. The green dotted line depicts the published value, 23.5 μm^2 /s and error bars represent the standard deviation of the values in each group. (B) Statistical significance was analyzed by t-test. (p-values at 12, 16, 20 and 24 hours post-transfection were 4.12×10^{-5}, 0.0925, 8.84×10^{-6} and 0.0001 , respectively).

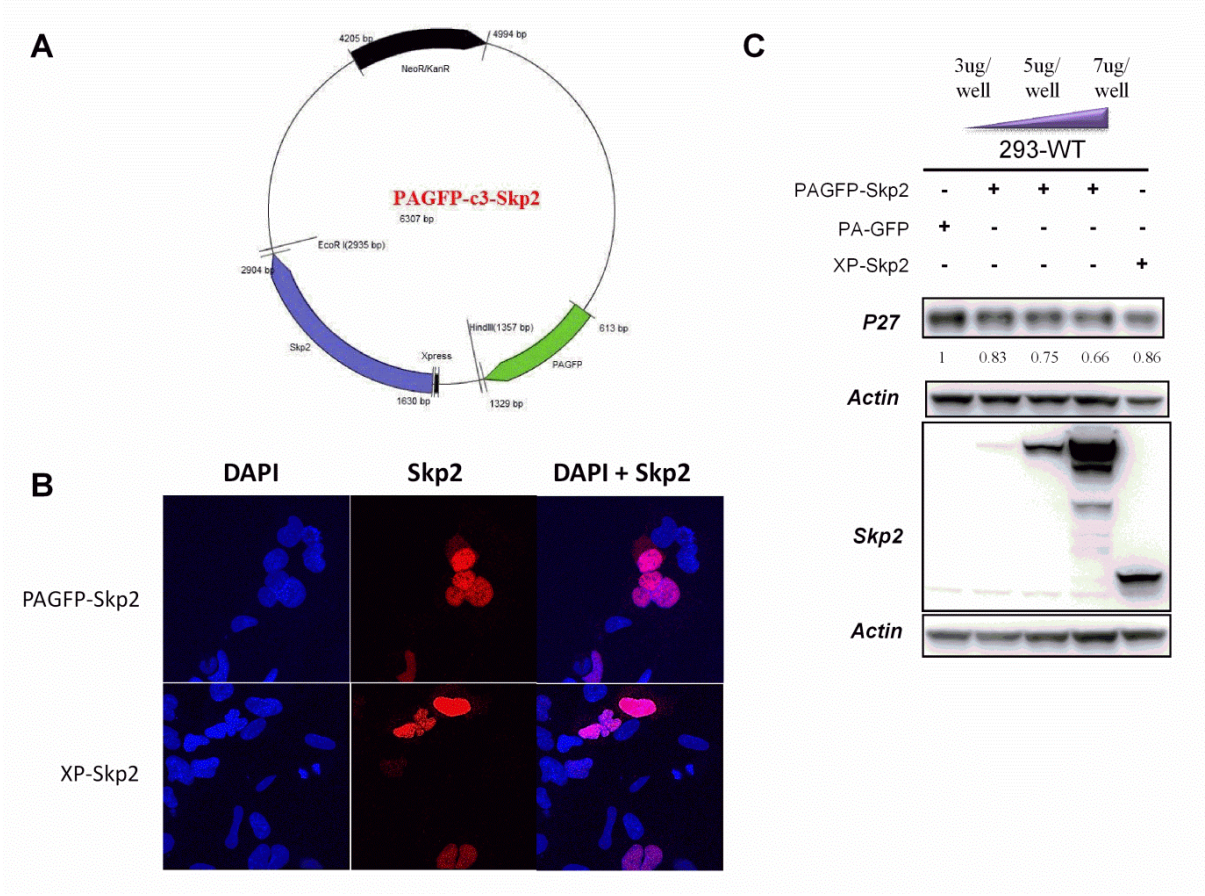

Figure 5.3 The functionality and localization of PAGFP-Skp2.

(A) Schema of the PA-GFP-Skp2 plasmid. (B) HEK 293 cells were transiently transfected with PA-GFP-Skp2 or XP-Skp2 plasmids, and consequently cells were harvested for immunofluorescence analysis in order to confirm the localization of PA-GFP-Skp2. (C) HEK 293 cells were transfected with PAGFP-Skp2, PA-GFP and XP-Skp2 plasmids, and harvested for fractionation, followed by Western blot analysis in order to confirm the PAGFP-Skp2-dependent degradation of p27.

5.2.4 Optimization of Photoactivated Protein Concentration for PAGFP-Skp2

Once the PAGFP-Skp2 function and cellular localization was shown to be consistent with those of the corresponding unlabeled protein properties, the next step in this work was to

see if the incremental photoactivation process could be used to improve quantification of this protein's diffusion coefficient. It was interesting to find that, in contrast to the case of cells expressing PA-GFP alone there was a significant slowly diffusing component for PAGFP-Skp2 in addition to the freely diffusing protein component, as was revealed by fitting RICS data to a two-component diffusion model (Eqs.11, 12, 13, 14 and 15). This slow component was likely to originate from Skp2-mediated ubiquitination that Skp2-SCF complex with their substrates is known to crated large slow-moving protein agglomerates. To determine the molecule number per pixel that was optimal for enhancing diffusion coefficient quantification, each HEK 293 cell transiently transfected with PAGFP-Skp2 was photoactivated from low molecular number per pixel to high using different photoactivating energy doses as described in the Methods section. After each photoactivation step, the diffusion coefficient was determined by RICS measurements performed at the previously optimized laser power of 10 mW (Fig. 5.1). The estimated diffusion coefficient of the freely diffusing PAGFP-Skp2 was estimated using the known cube root dependence of the diffusion coefficient on mass and the diffusion coefficient of PAGFP. Specifically, the diffusion coefficient of PAGFP-Skp2 was estimated as $\sqrt[3]{(m_{EGFP}/m_{PA\text{-}Skp2}} \times D_{EGFP}=16.8\ \mu m^2/s$, where D_{EGFP} is the published diffusion coefficient of EGFP, 23.5 $\mu m^2/s$, and m_{EGFP} and $m_{PA\text{-}Skp2}$ are the molecular weights of EGFP and PAGFP-Skp2, respectively (Wang et al, 2003). From these experiments it was determined that the optimal range of molecule number per pixel for determining the fast diffusion component accurately was 10.6-23 or greater (Fig. 5.4A). The slow second diffusion coefficient of PAGFP-Skp2 was small in value but varied significantly between experiments (Fig. 5.4B).

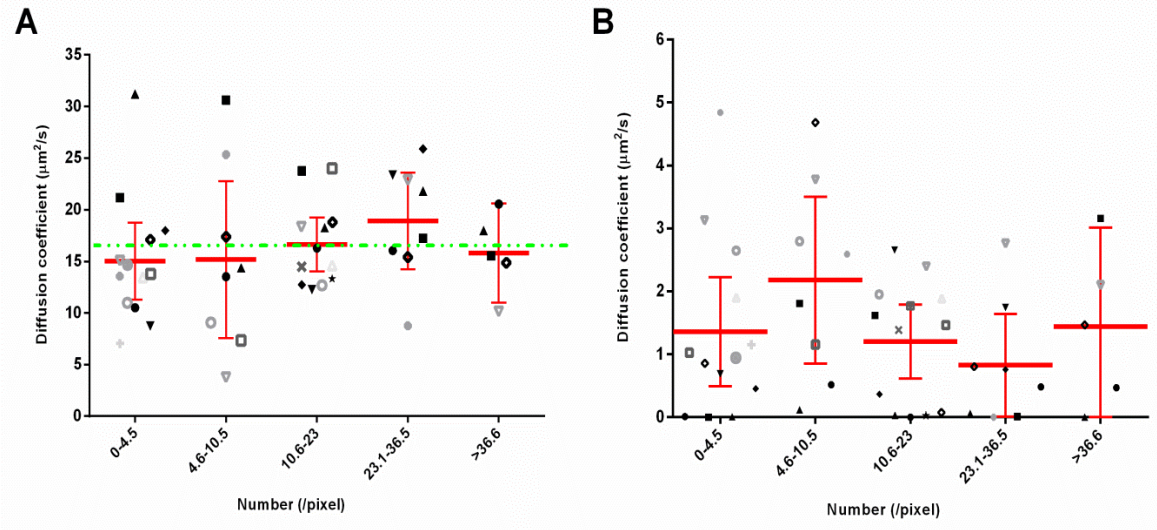

Figure 5.4 The fast (A) and slow (B) diffusion coefficients of PAGFP-Skp2 transiently expressed in HEK 293 cells. The diffusion coefficients were calculated at different ranges of molecule number per pixel with average laser power set at 10 mW. Each symbol represents an individual cell that was measured 3-5 times from low molecule number per pixel to high. The green dotted line depicts the theoretical diffusion value of 16.8 μm^2/s for freely diffusing PAGFP-Skp2 and error bars represent the standard deviation of each data group.

5.2.5 A Comparison of Diffusion Coefficient between EGFP-Skp2 and PAGFP-Skp2

Finally, the effect that the time-delay between transfection and RICS measurement had on the freely diffusing diffusion coefficient was explored. The fast diffusion coefficients of EGFP-Skp2 and PAGFP-Skp2 were measured by RICS analysis at 24, 48, and 72 hour post-transfection at the previously selected optimal laser power was 10 mW. Cells expressing enough PAGF-Skp2 for measurement occurred at around 24 hours post-transfection, and therefore experiments were initially performed at 24 hours post-transfection. Also, for the case of PAGFP-Skp2 the number of photoactivated molecules per pixel was made to be within the 10.6-23 range that was determined as optimal in the analysis presented in the previous section. The average fast diffusion coefficients of PAGFP-Skp2 at different post-transfection times were

essentially identical to the estimated value of 16.8 μm^2 /s. However, the fast diffusion coefficients of EGFP-Skp2 were distant to the estimated value for all post-transfection times (Fig. 5.5). The variances among the fast diffusion coefficients were not significantly different, as determined by ANOVA analysis for both PAGFP-Skp2 ($F_{[2,42]}$=0.71; p=0.4956)and EGFP-Skp2 ($F_{[2,46]}$=1.56;p=0.221) (Fig. 5.5B). Interestingly, for the case of slow diffusion coefficient the variances were also not significantly different for both PAGFP-Skp2 ($F_{[2,42]}$=0.12;p=0.884) and EGFP-Skp2 ($F_{[2,46]}$=2.784;p=0.0722) (Fig. 5.6B). In addition, differences in the mean values for 10 cells measurements were compared pair wise for the different time points and a marginally significant difference was only found at 48 hours post-transfection (Fig. 5.6A). Since the slow diffusion coefficient is only an apparent one, possibly incorporating binding-unbinding interactions with other protein complexes and cellular structures, its values will be cell-specific and a standard value reported in the literature does not exist. Therefore, a comparison of slow diffusion coefficients between EGFP-Skp2 and PAGFP-Skp2 cannot be achieved.

Interestingly, the EGFP-Skp2 fast diffusion coefficients were lower than the fast PAGFP-Skp2 diffusion coefficients by 40-60 %. In contrast, the diffusion coefficient difference between PAGFP and EGFP (Fig. 5.2) was ~30%. The diffusion coefficient difference for PAGFP-Skp2 compared to EGFP-Skp2 was larger than that for PA-GFP compared to EGFP due to the effect of the bound fraction for the case of Skp2. Specifically, the larger relative difference for the case of Skp2 was caused by the altered ratio of slow species to fast species present in the cell. The observed trend was that the slow to fast component ratio increased in cells with higher expression levels as more protein settled onto immobile structures. For proteins that are over-expressed this slower component is not physiologically relevant. The proposed methods drastically reduce the slow to fast component ratio because the activated volume (region of interest) was kept as small as possible (0.256 µm X 0.256 µm, see Methods) so that the chance for the slow species of PAGFP-Skp2 passing through the activation volume would be less than that of the fast species.

It should be noted that not only the photoactivation method presented in this work is capable of eliminating the immobile background, but pre-bleaching can eliminate some of the immobile background also. However, pre-bleaching requires repeated exposure of the cell at high powers as part of the immobile fraction typically persists even after repeated bleaching attempts, which ends up also reducing the mobile fraction of the protein and can result in thermal damage in the cell. On the contrary the proposed method only uses a very small ROI in which the immobile background can be photoactivated, which limits the immobile background contamination during RICS and N&B analysis.

5.3 Conclusion

In this study, an approach combining RICS and N&B analysis with use of PA-GFP as a tool to tune the fluorescent protein concentration in a cell was used to attain optimal quantification of molecular diffusion coefficients. Specifically, in this approach the photoactivated concentration of PA-GFP or of PA-GFP tagged protein was increased in a step-wise fashion by repeated exposure of a user-selected ROI with a fixed activation power of 2 mW at the focal spot at 765 nm. After each photoactivation step the molecular diffusion coefficient and concentration were determined by RICS and N&B analysis respectively. Thus, with measurements performed in this step-wise fashion the molecular diffusion coefficient was determined for a wide range of concentrations and the optimal range, leading to the highest diffusion coefficient accuracy, could be identified. The results show that for any time points post-transfection the measured molecular diffusion coefficients were significantly closer to the estimated value for freely diffusing protein in the cell, which was lower than that in aqueous solutions by a factor 4. At the same time the optimal photoactivated protein concentration for diffusion coefficient quantification was determined to be in the vicinity of 300 nM range for the microscopy setup and cell lines used in this work. Furthermore, the results of this work also

reveal that the determined diffusion coefficient variances were more uniform for the case of PA-GFP compared to EGFP (Section 5.2.2).

A potential advantage of the proposed photoactivation method was the improved control of the magnitude of the fluorescent protein immobile fraction as the photoactivation area was kept small and was comparable to the focal volume size. Given that immobile proteins would be exposed more than mobile proteins as the beam was scanned, the small size of the activation area limited the amount of immobile protein becoming fluorescent during the photoactivation step. On the other hand for the case of EGFP and EGFP-tagged proteins the amount of immobile fraction increased as the protein concentration increased and settled onto cellular structures. A significant immobile fraction form over-expressed fluorescent proteins was also seen for the stable transfection cell lines. Even though the pre-bleach method could be used to eliminate the immobile fraction in the above cases, pre-bleaching would have to be implemented over the entire imaging ROI which would eliminate a large portion of the mobile fraction in addition to the immobile fraction, which resulted in dramatic reduction of the fluorescence intensity. Furthermore, even after severe pre-bleaching a small immobile fraction persisted and could not be completely removed.

It was interesting to observe that there was a ~30% difference diffusion coefficient difference between PAGFP and EGFP (Fig. 5.2), which increased to 40-60 % when comparing the diffusion coefficients of PAGFP-Skp2 to EGFP-Skp2. This difference is attributed to the presence of an immobile or slowly moving fluorescent protein fraction that was removed from the signal in the photoactivation approach by persisted in the EGFP case. This signal from the low mobility proteins resulted in lower diffusion coefficients determined by RICS analysis, even when a two-component model was used to facilitate the removal of the slower component. The contamination of the fast diffusion coefficient by slowly moving or immobile protein is a potential limitation of the RICS method. Even though the photoactivation approach used in this work appeared to alleviate this problem these results may be of limited utility if the reason for

removing the immobile or slower protein fraction was photobleaching. Specifically, the results shown in Fig. 5.1E are consistent with an interpretation where photobleaching and inadvertent photoactivation at 920 nm, the imaging wavelength, compensate for each other to maintain an approximately constant free mobile fraction concentration while the slower protein fraction is preferentially removed. This limitation is thought to originate from the small but finite photoactivation cross-section of PA-GFP at 920 nm, which also required fairly high two-photon excitation powers to be imaged with our two-photon setup. This difficult issue of avoiding inadvertent photoactivation of PA-GFP during imaging needs to be addressed in future work.

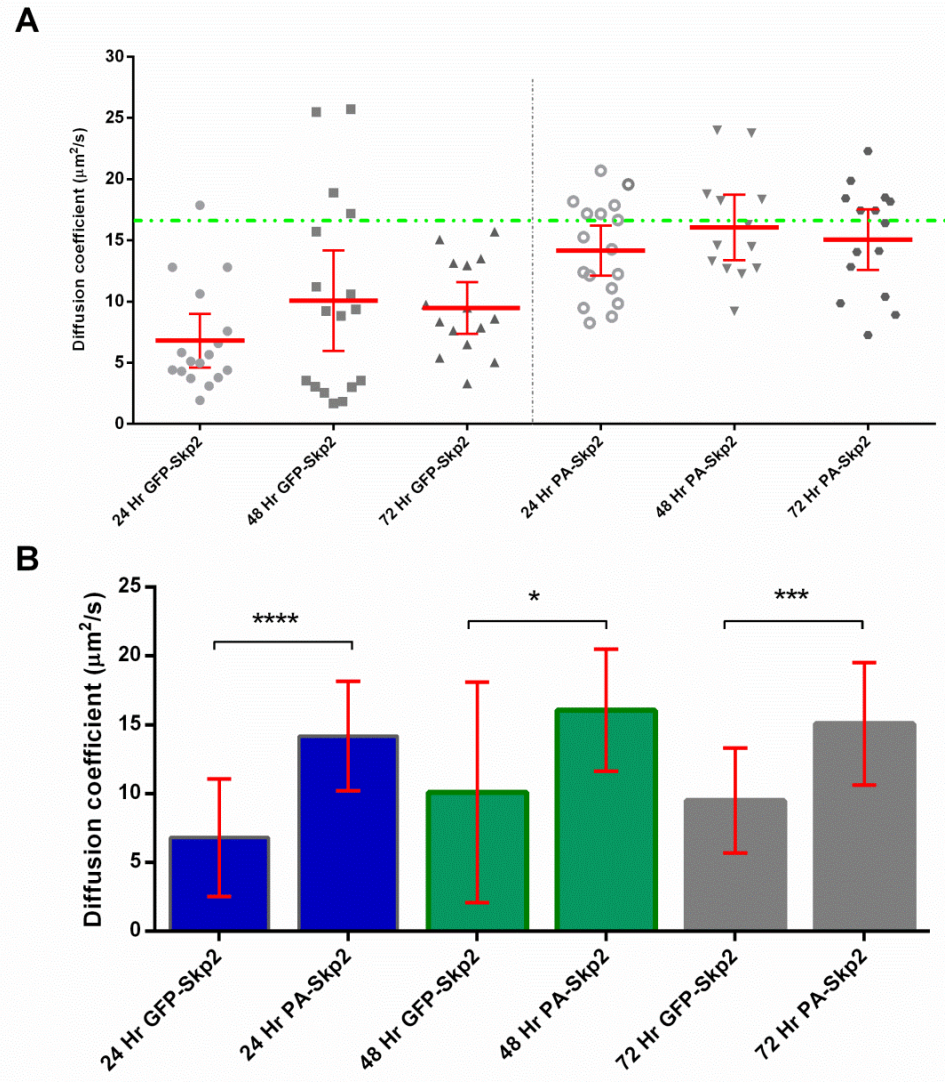

Figure 5.5 A comparison between the fast diffusion coefficients of EGFP-Skp2 and PAGFP-Skp2. (A) HEK 293 cells were transiently transfected with the EGFP-Skp2 or PAGFP-Skp2 plasmid and the diffusion coefficient was measured using RICS analysis at 24, 48 and 72 hours post-transfection. Each data point represents an independent measurement at the different cell. The green dotted line depicts the estimated value for PAGFP-Skp2 of 16.8 $\mu m^2/s$ and the error bars represent the standard deviation of each data group. (B) Statistical significance of pair-wise differences between the fast diffusion components of PAGFP-Skp2 and EGFP-Skp2. Significant differences are indicated by the asterisks ($p_{24hr}=1.05\times10^{-5}$, $p_{48hr}=0.0226$, $p=0.001$).

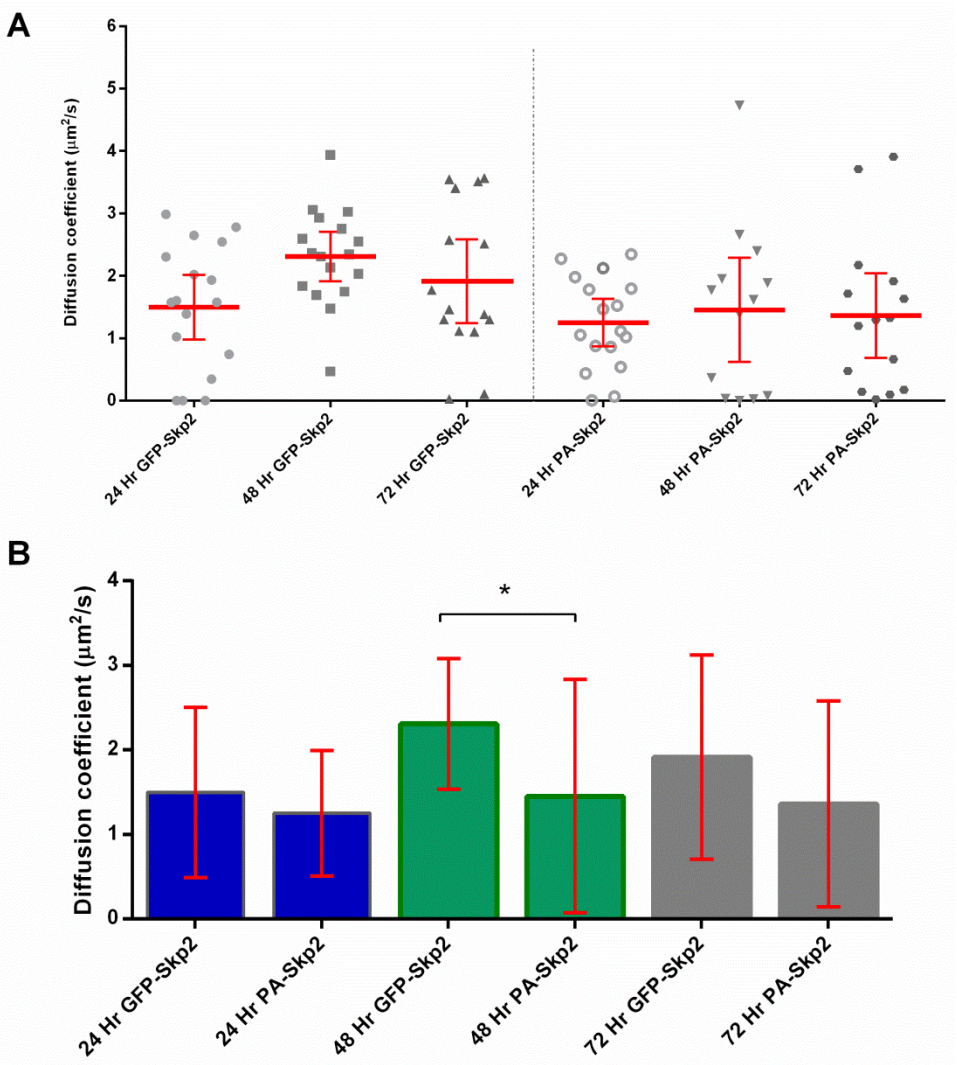

Figure 5.6 A comparison between the slow diffusion coefficients of EGFP-Skp2 and PAGFP-Skp2**.** (A) HEK 293 cells were transiently transfected with the EGFP-Skp2 or PAGFP-Skp2 plasmid and the diffusion coefficient was measured using RICS analysis at 24, 48 and 72 hours post-transfection. Each data point represents an independent measurement at the different cell. The error bars represent the standard deviation of each data group. (B) Statistical significance of pair-wise differences between the fast diffusion components of PAGFP-Skp2 and EGFP-Skp2. The error bars represent the standard deviation of each data group. Significant differences are indicated by the asterisk (p_{48hr}=0.0396, p_{48hr}=0.0226, p_{72hr}=0.001).

CHAPTER 6

CONCLUSION AND FUTURE WORK

The conclusions from the results found along with suggestions for extensions to this work, are discussed individually by chapter in the subsections here below.

6.1 The interaction between AR and DAB2IP

In this work, a dose-dependent and time-dependent nuclear translocation was observed in presence of DHT by using N&B analysis. For lower concentrations of DHT, the dynamic rate of AR nuclear translocation was slower. Most importantly, when HEK 293 cells stably expressed both AR and DAB2IP, DAB2IP was capable of blocking AR nuclear translocation upon DHT treatment which implies that DAB2IP could suppress AR transcriptional activity in order to regulate AR target gene expression. Furthermore, AR mutants frequently occur at castration resistant prostate cancers, and mutants at the Serine 81 and 650 phosphorylation sites have attracted a lot of attention as these have been associated with AR chromatin binding regulating transcription and AR nuclear export, respectively. For the case of mutation of Serine 81, DAB2IP was found to fail blocking the nuclear translocation of ARS81D, a mutant with constitutive phosphorylation at the Ser-81 site, and also failed to inhibit ARS81D transcriptional activity. In addition, ARS650D, a mutant with constitutive phosphorylation at the Ser-650 site was found to fail at translocating from the cytoplasm to nucleus in the presence of DHT. As a result no DAB2IP interaction with AR650D was observed in this work. Whether DAB2IP can directly interact with wild-type AR or mutant AR remains unknown. To address this issue, the next step in future work is to construct an mCherry tagged DAPB2IP protein. In a two-photon microscopy system, cross-correlation RICS (cc-RICS) analysis or cross-correlation FCS in combination with GFP-AR and mCherry-DAB2IP can be used to investigate the interaction

between DAB2IP and AR in the living cell. In addition, the molecular kinetics of DAB2IP and AR in the presence of different levels of androgen also can be determined using cc-RICS analysis.

6.2 The Role of DAB2IP in Radiation Therapy

Whether DAB2IP is involved in DNA repair remains unclear to date. To address this issue, experiments were performed to investigate the functional role of DAB2IP upon IR treatment. The results of this work reveal that DAB2IP can repress IR-induced autophagy in order to increase the radiosensitivity, and in combination with NU7441 can further enhance anti-tumor activity due to suppression of autophagy. In addition, whether DAB2IP can be involved in DNA repair by relocating at DSB sites could not be answered in this work. That co-localization of DAB2IP and γH2AX was not observed, at least not within the sensitivity of detection limits of the immunofluorescence technique used, which implies that DAB2IP may not directly relocate at DSB sites. Nevertheless, DAB2IP nucleocytoplasmic transportation upon IR-induction was found in this work. In Western blot measurement, DAB2IP-EGFP nuclear levels were found to gradually increase until 2 hours post IR-induction, an observation that is compatible with the current hypothesis that DAB2IP may be involved in DNA DSB repair through nuclear transport. Therefore, this result is also a preliminary experiment for the kinetics of DAB2IP in response to DNA damage. The next step for future work is the quantification of DAB2IP kinetic parameters by RICS analysis in the two-photon system available in Dr. Alexandrakis' lab. Specifically, in Western blot analysis the protein fraction could have been contaminated by the cytoplasmic fraction obtained from the nucleus and cytosol extraction kit, and the contamination levels could vary from samples to sample which could have caused variation in the apparent DAB2IP nuclear levels quantified by this method. Direct quantification of the DAB2IP concentration and its diffusion coefficient in living cells using RICS analysis could alleviate this problem.

6.3 A Method for the Improved Quantification of a Protein's Diffusion Coefficient by Control of Fluorescent Protein Concentration through Photoactivation

An approach combining RICS and N&B analysis with use of PA-GFP as a tool to tune the fluorescent protein concentration in a cell was used to attain optimal quantification of molecular diffusion coefficients. The photoactivated concentration of PA-GFP or PA-GFP tagged proteins was increased by repeated exposure of a user-selected ROI with an activation power of 2 mW at 765 nm. Molecular diffusion coefficients and concentrations were determined by RICS and N&B analysis, respectively, after each photoactivation step. Therefore, the optimal photoactivated concentration could be identified from a wide range of concentrations. The optimal photoactivated concentration in this work was determined to be in the vicinity of ~300nM which resulted in a measured diffusion coefficient of PA-GFP that was significantly closer to the estimated value of 23.5 $\mu m^2/s$ than equivalent measurements in cells transiently expressing EGFP for any time point post-transfection. In comparison, the measurements in cells expressing EGFP produced ~30% lower diffusion coefficients compared to the PA-GFP measurements, and the determined diffusion coefficient variances were also more uniform for the case of PA-GFP. In addition, the proposed photoactivation method could improve control of the magnitude of the fluorescent protein immobile fraction as the photoactivation area was kept small and was comparable to the focal volume size. The small size of the activation area limited the amount of immobile protein becoming fluorescent during the photoactivation step. Therefore, the diffusion coefficient difference between EGFP-Skp2 and PAGFP-Skp2 was increased to 40-60% compared the ~30% difference between EGFP and PA-GFP. The spatial correlation function due to fast dynamics could be contaminated by the presence of an immobile or slowly moving fluorescent protein fraction, which resulted in the observed diffusion coefficient difference between EGFP and PA-GFP or EGFP-Skp2 and PAGFP-Skp2. However, these results may be of limited utility if the reason for removing the immobile or slower protein fraction was photobleaching during the imaging step. If photobleaching and inadvertent photoactivation

occurred at 920 nm during RICS measurements, a constant free mobile fraction concentration could have been maintained while a slower protein fraction was also being removed at the same time. Therefore, avoiding inadvertent photoactivation of PA-GFP during RICS measurements will be the next question to be solved. In future work, the recombinant PA-GPF protein will be used in combination with super-continuum generated two-photon excitation to control the wavelength range and excitation powers which could limit the bleaching of photoactivated slow-moving or immobile PA-GFP protein in the cell while permitting adequate fluorescence emission for image.

REFERENCES

Abbotts R, Madhusudan S (2010) Human AP endonuclease 1 (APE1): from mechanistic insights to druggable target in cancer. *Cancer Treat Rev* **36:** 425-435

Akakura K, Bruchovsky N, Goldenberg SL, Rennie PS, Buckley AR, Sullivan LD (1993) Effects of intermittent androgen suppression on androgen-dependent tumors. Apoptosis and serum prostate-specific antigen. *Cancer* **71:** 2782-2790

Akiyama T (2000) Wnt/beta-catenin signaling. *Cytokine Growth Factor Rev* **11:** 273-282

Albota MA, Xu C, Webb WW (1998) Two-Photon Fluorescence Excitation Cross Sections of Biomolecular Probes from 690 to 960 nm. *Appl Opt* **37:** 7352-7356

Annibale P, Vanni S, Scarselli M, Rothlisberger U, Radenovic A (2011) Quantitative photo activated localization microscopy: unraveling the effects of photoblinking. *PLoS One* **6:** e22678

Apel A, Herr I, Schwarz H, Rodemann HP, Mayer A (2008) Blocked autophagy sensitizes resistant carcinoma cells to radiation therapy. *Cancer Res* **68:** 1485-1494

Bacia K, Schwille P (2003) A dynamic view of cellular processes by in vivo fluorescence auto- and cross-correlation spectroscopy. *Methods* **29:** 74-85

Bae H, Guan JL (2011) Suppression of autophagy by FIP200 deletion impairs DNA damage repair and increases cell death upon treatments with anticancer agents. *Mol Cancer Res* **9:** 1232-1241

Baritaki S, Chapman A, Yeung K, Spandidos DA, Palladino M, Bonavida B (2009) Inhibition of epithelial to mesenchymal transition in metastatic prostate cancer cells by the novel proteasome inhibitor, NPI-0052: pivotal roles of Snail repression and RKIP induction. *Oncogene* **28:** 3573-3585

Bates M, Huang B, Zhuang X (2008) Super-resolution microscopy by nanoscale localization of photo-switchable fluorescent probes. *Curr Opin Chem Biol* **12:** 505-514

Bohrer LR, Chen S, Hallstrom TC, Huang H (2010) Androgens suppress EZH2 expression via retinoblastoma (RB) and p130-dependent pathways: a potential mechanism of androgen-refractory progression of prostate cancer. *Endocrinology* **151:** 5136-5145

Bolla M, Van Tienhoven G, Warde P, Dubois JB, Mirimanoff RO, Storme G, Bernier J, Kuten A, Sternberg C, Billiet I, Torecilla JL, Pfeffer R, Cutajar CL, Van der Kwast T, Collette L (2010) External irradiation with or without long-term androgen suppression for prostate cancer with high metastatic risk: 10-year results of an EORTC randomised study. *Lancet Oncol* **11:** 1066-1073

Bolos V, Peinado H, Perez-Moreno MA, Fraga MF, Esteller M, Cano A (2003) The transcription factor Slug represses E-cadherin expression and induces epithelial to mesenchymal transitions: a comparison with Snail and E47 repressors. *J Cell Sci* **116:** 499-511

Brazda P, Szekeres T, Bravics B, Toth K, Vamosi G, Nagy L (2011) Live-cell fluorescence correlation spectroscopy dissects the role of coregulator exchange and chromatin binding in retinoic acid receptor mobility. *J Cell Sci* **124:** 3631-3642

Brinkmann AO, Trapman J (2000) Genetic analysis of androgen receptors in development and disease. *Adv Pharmacol* **47:** 317-341

Brown CM, Dalal RB, Hebert B, Digman MA, Horwitz AR, Gratton E (2008) Raster image correlation spectroscopy (RICS) for measuring fast protein dynamics and concentrations with a commercial laser scanning confocal microscope. *J Microsc* **229:** 78-91

Bryant HE, Schultz N, Thomas HD, Parker KM, Flower D, Lopez E, Kyle S, Meuth M, Curtin NJ, Helleday T (2005) Specific killing of BRCA2-deficient tumours with inhibitors of poly(ADP-ribose) polymerase. *Nature* **434:** 913-917

Bubendorf L, Kononen J, Koivisto P, Schraml P, Moch H, Gasser TC, Willi N, Mihatsch MJ, Sauter G, Kallioniemi OP (1999) Survey of gene amplifications during prostate cancer progression by high-throughout fluorescence in situ hybridization on tissue microarrays. *Cancer Res* **59:** 803-806

Capasso LL (2005) Antiquity of cancer. *Int J Cancer* **113:** 2-13

Carrano AC, Eytan E, Hershko A, Pagano M (1999) SKP2 is required for ubiquitin-mediated degradation of the CDK inhibitor p27. *Nat Cell Biol* **1:** 193-199

Chaudhary S, Pak JE, Gruswitz F, Sharma V, Stroud RM (2012) Overexpressing human membrane proteins in stably transfected and clonal human embryonic kidney 293S cells. *Nat Protoc* **7:** 453-466

Chen H, Toyooka S, Gazdar AF, Hsieh JT (2003) Epigenetic regulation of a novel tumor suppressor gene (hDAB2IP) in prostate cancer cell lines. *J Biol Chem* **278:** 3121-3130

Chen H, Tu SW, Hsieh JT (2005) Down-regulation of human DAB2IP gene expression mediated by polycomb Ezh2 complex and histone deacetylase in prostate cancer. *J Biol Chem* **280:** 22437-22444

Chen S, Gulla S, Cai C, Balk SP (2012) Androgen receptor serine 81 phosphorylation mediates chromatin binding and transcriptional activation. *J Biol Chem* **287:** 8571-8583

Chen Y, Muller JD, Ruan Q, Gratton E (2002) Molecular brightness characterization of EGFP in vivo by fluorescence fluctuation spectroscopy. *Biophys J* **82:** 133-144

Chen Y, Muller JD, So PT, Gratton E (1999) The photon counting histogram in fluorescence fluctuation spectroscopy. *Biophys J* **77:** 553-567

Chen Y, Sawyers CL, Scher HI (2008) Targeting the androgen receptor pathway in prostate cancer. *Curr Opin Pharmacol* **8:** 440-448

Chudakov DM, Matz MV, Lukyanov S, Lukyanov KA (2010) Fluorescent proteins and their applications in imaging living cells and tissues. *Physiol Rev* **90:** 1103-1163

Costarella CE, Stallone JN, Rutecki GW, Whittier FC (1996) Testosterone causes direct relaxation of rat thoracic aorta. *J Pharmacol Exp Ther* **277:** 34-39

Cowen D, Salem N, Ashoori F, Meyn R, Meistrich ML, Roth JA, Pollack A (2000) Prostate cancer radiosensitization in vivo with adenovirus-mediated p53 gene therapy. *Clin Cancer Res* **6:** 4402-4408

Cunha GR, Young P (1991) Inability of Tfm (testicular feminization) epithelial cells to express androgen-dependent seminal vesicle secretory proteins in chimeric tissue recombinants. *Endocrinology* **128:** 3293-3298

Curtin NJ (2012) DNA repair dysregulation from cancer driver to therapeutic target. *Nat Rev Cancer* **12:** 801-817

D'Amico AV (2002) Radiation and hormonal therapy for locally advanced and clinically localized prostate cancer. *Urology* **60:** 32-37; discussion 37-38

Daido S, Yamamoto A, Fujiwara K, Sawaya R, Kondo S, Kondo Y (2005) Inhibition of the DNA-dependent protein kinase catalytic subunit radiosensitizes malignant glioma cells by inducing autophagy. *Cancer Res* **65:** 4368-4375

Dauty E, Verkman AS (2004) Molecular crowding reduces to a similar extent the diffusion of small solutes and macromolecules: measurement by fluorescence correlation spectroscopy. *J Mol Recognit* **17:** 441-447

Dauty E, Verkman AS (2005) Actin cytoskeleton as the principal determinant of size-dependent DNA mobility in cytoplasm: a new barrier for non-viral gene delivery. *J Biol Chem* **280:** 7823-7828

de Vere White R, Meyers F, Chi SG, Chamberlain S, Siders D, Lee F, Stewart S, Gumerlock PH (1997) Human androgen receptor expression in prostate cancer following androgen ablation. *Eur Urol* **31:** 1-6

Dehm SM, Schmidt LJ, Heemers HV, Vessella RL, Tindall DJ (2008) Splicing of a novel androgen receptor exon generates a constitutively active androgen receptor that mediates prostate cancer therapy resistance. *Cancer Res* **68:** 5469-5477

Dehm SM, Tindall DJ (2006) Molecular regulation of androgen action in prostate cancer. *J Cell Biochem* **99:** 333-344

Denk W, Strickler JH, Webb WW (1990) Two-photon laser scanning fluorescence microscopy. *Science* **248:** 73-76

Diaspro A, Chirico G, Collini M (2005) Two-photon fluorescence excitation and related techniques in biological microscopy. *Q Rev Biophys* **38:** 97-166

Digman MA, Brown CM, Sengupta P, Wiseman PW, Horwitz AR, Gratton E (2005) Measuring fast dynamics in solutions and cells with a laser scanning microscope. *Biophys J* **89:** 1317-1327

Digman MA, Dalal R, Horwitz AF, Gratton E (2008) Mapping the number of molecules and brightness in the laser scanning microscope. *Biophys J* **94:** 2320-2332

Digman MA, Gratton E (2009) Analysis of diffusion and binding in cells using the RICS approach. *Microsc Res Tech* **72:** 323-332

Digman MA, Wiseman PW, Horwitz AR, Gratton E (2009) Detecting protein complexes in living cells from laser scanning confocal image sequences by the cross correlation raster image spectroscopy method. *Biophys J* **96:** 707-716

Dill KA, Ghosh K, Schmit JD (2011) Physical limits of cells and proteomes. *Proc Natl Acad Sci U S A* **108:** 17876-17882

DiTullio RA, Jr., Mochan TA, Venere M, Bartkova J, Sehested M, Bartek J, Halazonetis TD (2002) 53BP1 functions in an ATM-dependent checkpoint pathway that is constitutively activated in human cancer. *Nat Cell Biol* **4:** 998-1002

Donjacour AA, Cunha GR (1993) Assessment of prostatic protein secretion in tissue recombinants made of urogenital sinus mesenchyme and urothelium from normal or androgen-insensitive mice. *Endocrinology* **132:** 2342-2350

Dote H, Toyooka S, Tsukuda K, Yano M, Ota T, Murakami M, Naito M, Toyota M, Gazdar AF, Shimizu N (2005) Aberrant promoter methylation in human DAB2 interactive protein (hDAB2IP) gene in gastrointestinal tumour. *Br J Cancer* **92:** 1117-1125

Dote H, Toyooka S, Tsukuda K, Yano M, Ouchida M, Doihara H, Suzuki M, Chen H, Hsieh JT, Gazdar AF, Shimizu N (2004) Aberrant promoter methylation in human DAB2 interactive protein (hDAB2IP) gene in breast cancer. *Clin Cancer Res* **10:** 2082-2089

Drobizhev M, Makarov NS, Tillo SE, Hughes TE, Rebane A (2011) Two-photon absorption properties of fluorescent proteins. *Nat Methods* **8:** 393-399

Edwards J, Krishna NS, Grigor KM, Bartlett JM (2003) Androgen receptor gene amplification and protein expression in hormone refractory prostate cancer. *Br J Cancer* **89:** 552-556

Eger A, Stockinger A, Schaffhauser B, Beug H, Foisner R (2000) Epithelial mesenchymal transition by c-Fos estrogen receptor activation involves nuclear translocation of beta-catenin and upregulation of beta-catenin/lymphoid enhancer binding factor-1 transcriptional activity. *J Cell Biol* **148:** 173-188

Fabbro M, Henderson BR (2003) Regulation of tumor suppressors by nuclear-cytoplasmic shuttling. *Exp Cell Res* **282:** 59-69

Fabbro M, Rodriguez JA, Baer R, Henderson BR (2002) BARD1 induces BRCA1 intranuclear foci formation by increasing RING-dependent BRCA1 nuclear import and inhibiting BRCA1 nuclear export. *J Biol Chem* **277:** 21315-21324

Fabbro M, Schuechner S, Au WW, Henderson BR (2004) BARD1 regulates BRCA1 apoptotic function by a mechanism involving nuclear retention. *Exp Cell Res* **298:** 661-673

Farmer H, McCabe N, Lord CJ, Tutt AN, Johnson DA, Richardson TB, Santarosa M, Dillon KJ, Hickson I, Knights C, Martin NM, Jackson SP, Smith GC, Ashworth A (2005) Targeting the DNA repair defect in BRCA mutant cells as a therapeutic strategy. *Nature* **434:** 917-921

Feng L, Lin T, Uranishi H, Gu W, Xu Y (2005) Functional analysis of the roles of posttranslational modifications at the p53 C terminus in regulating p53 stability and activity. *Mol Cell Biol* **25:** 5389-5395

Fernandez-Capetillo O, Chen HT, Celeste A, Ward I, Romanienko PJ, Morales JC, Naka K, Xia Z, Camerini-Otero RD, Motoyama N, Carpenter PB, Bonner WM, Chen J, Nussenzweig A (2002) DNA damage-induced G2-M checkpoint activation by histone H2AX and 53BP1. *Nat Cell Biol* **4:** 993-997

Finkelstein SE, Fishman M (2012) Clinical opportunities in combining immunotherapy with radiation therapy. *Front Oncol* **2:** 169

Fitzpatrick JA, Lillemeier BF (2011) Fluorescence correlation spectroscopy: linking molecular dynamics to biological function in vitro and in situ. *Curr Opin Struct Biol* **21:** 650-660

Ford OH, 3rd, Gregory CW, Kim D, Smitherman AB, Mohler JL (2003) Androgen receptor gene amplification and protein expression in recurrent prostate cancer. *J Urol* **170:** 1817-1821

Franken NA, Rodermond HM, Stap J, Haveman J, van Bree C (2006) Clonogenic assay of cells in vitro. *Nat Protoc* **1:** 2315-2319

Freytag SO, Stricker H, Pegg J, Paielli D, Pradhan DG, Peabody J, DePeralta-Venturina M, Xia X, Brown S, Lu M, Kim JH (2003) Phase I study of replication-competent adenovirus-mediated double-suicide gene therapy in combination with conventional-dose three-dimensional conformal radiation therapy for the treatment of newly diagnosed, intermediate- to high-risk prostate cancer. *Cancer Res* **63:** 7497-7506

Gao D, Inuzuka H, Tseng A, Chin RY, Toker A, Wei W (2009) Phosphorylation by Akt1 promotes cytoplasmic localization of Skp2 and impairs APCCdh1-mediated Skp2 destruction. *Nat Cell Biol* **11:** 397-408

Gioeli D, Black BE, Gordon V, Spencer A, Kesler CT, Eblen ST, Paschal BM, Weber MJ (2006) Stress kinase signaling regulates androgen receptor phosphorylation, transcription, and localization. *Mol Endocrinol* **20:** 503-515

Gioeli D, Ficarro SB, Kwiek JJ, Aaronson D, Hancock M, Catling AD, White FM, Christian RE, Settlage RE, Shabanowitz J, Hunt DF, Weber MJ (2002) Androgen receptor phosphorylation. Regulation and identification of the phosphorylation sites. *J Biol Chem* **277:** 29304-29314

Goldenberg SL, Koupparis A, Robinson ME (2011) Differing levels of testosterone and the prostate: a physiological interplay. *Nat Rev Urol* **8:** 365-377

Gonzalez-Polo RA, Boya P, Pauleau AL, Jalil A, Larochette N, Souquere S, Eskelinen EL, Pierron G, Saftig P, Kroemer G (2005) The apoptosis/autophagy paradox: autophagic vacuolization before apoptotic death. *J Cell Sci* **118:** 3091-3102

Gordon V, Bhadel S, Wunderlich W, Zhang J, Ficarro SB, Mollah SA, Shabanowitz J, Hunt DF, Xenarios I, Hahn WC, Conaway M, Carey MF, Gioeli D (2010) CDK9 regulates AR promoter selectivity and cell growth through serine 81 phosphorylation. *Mol Endocrinol* **24:** 2267-2280

Gregory CW, Johnson RT, Jr., Mohler JL, French FS, Wilson EM (2001) Androgen receptor stabilization in recurrent prostate cancer is associated with hypersensitivity to low androgen. *Cancer Res* **61:** 2892-2898

Haustein E, Schwille P (2003) Ultrasensitive investigations of biological systems by fluorescence correlation spectroscopy. *Methods* **29:** 153-166

Haustein E, Schwille P (2007) Fluorescence correlation spectroscopy: novel variations of an established technique. *Annu Rev Biophys Biomol Struct* **36:** 151-169

Heemers HV, Tindall DJ (2007) Androgen receptor (AR) coregulators: a diversity of functions converging on and regulating the AR transcriptional complex. *Endocr Rev* **28:** 778-808

Heinlein CA, Chang C (2002) Androgen receptor (AR) coregulators: an overview. *Endocr Rev* **23:** 175-200

Henderson JN, Gepshtein R, Heenan JR, Kallio K, Huppert D, Remington SJ (2009) Structure and mechanism of the photoactivatable green fluorescent protein. *J Am Chem Soc* **131:** 4176-4177

Hess ST, Girirajan TP, Mason MD (2006) Ultra-high resolution imaging by fluorescence photoactivation localization microscopy. *Biophys J* **91:** 4258-4272

Hippert MM, O'Toole PS, Thorburn A (2006) Autophagy in cancer: good, bad, or both? *Cancer Res* **66:** 9349-9351

Hu R, Dunn TA, Wei S, Isharwal S, Veltri RW, Humphreys E, Han M, Partin AW, Vessella RL, Isaacs WB, Bova GS, Luo J (2009) Ligand-independent androgen receptor variants derived from splicing of cryptic exons signify hormone-refractory prostate cancer. *Cancer Res* **69:** 16-22

Jemal A, Murray T, Ward E, Samuels A, Tiwari RC, Ghafoor A, Feuer EJ, Thun MJ (2005) Cancer statistics, 2005. *CA Cancer J Clin* **55:** 10-30

Jenster G, Trapman J, Brinkmann AO (1993) Nuclear import of the human androgen receptor. *Biochem J* **293 (Pt 3):** 761-768

Kaier W GC (1961) Two-photon excitation in CaF_2:Eu^{2+}. *Phys Rev Lett***:** 229-231

Kalwarczyk T, Tabaka M, Holyst R (2012) Biologistics--diffusion coefficients for complete proteome of Escherichia coli. *Bioinformatics* **28:** 2971-2978

Kaprealian T, Weinberg V, Speight JL, Gottschalk AR, Roach M, 3rd, Shinohara K, Hsu IC (2012) High-dose-rate brachytherapy boost for prostate cancer: comparison of two different fractionation schemes. *Int J Radiat Oncol Biol Phys* **82:** 222-227

Kastan MB, Lim DS (2000) The many substrates and functions of ATM. *Nat Rev Mol Cell Biol* **1:** 179-186

Kim SA, Sanabria H, Digman MA, Gratton E, Schwille P, Zipfel WR, Waxham MN (2010) Quantifying translational mobility in neurons: comparison between current optical techniques. *J Neurosci* **30:** 16409-16416

Koivisto P, Kononen J, Palmberg C, Tammela T, Hyytinen E, Isola J, Trapman J, Cleutjens K, Noordzij A, Visakorpi T, Kallioniemi OP (1997) Androgen receptor gene amplification: a possible molecular mechanism for androgen deprivation therapy failure in prostate cancer. *Cancer Res* **57:** 314-319

Kong Z, Raghavan P, Xie D, Boike T, Burma S, Chen D, Chakraborty A, Hsieh JT, Saha D (2010a) Epothilone B confers radiation dose enhancement in DAB2IP gene knock-down radioresistant prostate cancer cells. *Int J Radiat Oncol Biol Phys* **78:** 1210-1218

Kong Z, Xie D, Boike T, Raghavan P, Burma S, Chen DJ, Habib AA, Chakraborty A, Hsieh JT, Saha D (2010b) Downregulation of human DAB2IP gene expression in prostate cancer cells results in resistance to ionizing radiation. *Cancer Res* **70:** 2829-2839

Kousteni S, Bellido T, Plotkin LI, O'Brien CA, Bodenner DL, Han L, Han K, DiGregorio GB, Katzenellenbogen JA, Katzenellenbogen BS, Roberson PK, Weinstein RS, Jilka RL, Manolagas SC (2001) Nongenotropic, sex-nonspecific signaling through the estrogen or androgen receptors: dissociation from transcriptional activity. *Cell* **104:** 719-730

Kouzarides T (2007) Chromatin modifications and their function. *Cell* **128:** 693-705

Lapointe J, Li C, Higgins JP, van de Rijn M, Bair E, Montgomery K, Ferrari M, Egevad L, Rayford W, Bergerheim U, Ekman P, DeMarzo AM, Tibshirani R, Botstein D, Brown PO, Brooks JD, Pollack JR (2004) Gene expression profiling identifies clinically relevant subtypes of prostate cancer. *Proc Natl Acad Sci U S A* **101:** 811-816

Lee AK (2006) Radiation therapy combined with hormone therapy for prostate cancer. *Semin Radiat Oncol* **16:** 20-28

Lee JG, Kay EP (2008) Involvement of two distinct ubiquitin E3 ligase systems for p27 degradation in corneal endothelial cells. *Invest Ophthalmol Vis Sci* **49:** 189-196

Lee MN, Tseng RC, Hsu HS, Chen JY, Tzao C, Ho WL, Wang YC (2007) Epigenetic inactivation of the chromosomal stability control genes BRCA1, BRCA2, and XRCC5 in non-small cell lung cancer. *Clin Cancer Res* **13:** 832-838

Lichtman JW, Conchello JA (2005) Fluorescence microscopy. *Nat Methods* **2:** 910-919

Lin HK, Chen Z, Wang G, Nardella C, Lee SW, Chan CH, Yang WL, Wang J, Egia A, Nakayama KI, Cordon-Cardo C, Teruya-Feldstein J, Pandolfi PP (2010) Skp2 targeting suppresses tumorigenesis by Arf-p53-independent cellular senescence. *Nature* **464:** 374-379

Lin HK, Wang G, Chen Z, Teruya-Feldstein J, Liu Y, Chan CH, Yang WL, Erdjument-Bromage H, Nakayama KI, Nimer S, Tempst P, Pandolfi PP (2009) Phosphorylation-dependent regulation of cytosolic localization and oncogenic function of Skp2 by Akt/PKB. *Nat Cell Biol* **11:** 420-432

Lindzey J, Kumar MV, Grossman M, Young C, Tindall DJ (1994) Molecular mechanisms of androgen action. *Vitam Horm* **49:** 383-432

Linja MJ, Savinainen KJ, Saramaki OR, Tammela TL, Vessella RL, Visakorpi T (2001) Amplification and overexpression of androgen receptor gene in hormone-refractory prostate cancer. *Cancer Res* **61:** 3550-3555

Liu Y, Zhou K, Zhang H, Shugart YY, Chen L, Xu Z, Zhong Y, Liu H, Jin L, Wei Q, Huang F, Lu D, Zhou L (2008) Polymorphisms of LIG4 and XRCC4 involved in the NHEJ pathway interact to modify risk of glioma. *Hum Mutat* **29:** 381-389

Locke JA, Guns ES, Lubik AA, Adomat HH, Hendy SC, Wood CA, Ettinger SL, Gleave ME, Nelson CC (2008) Androgen levels increase by intratumoral de novo steroidogenesis during progression of castration-resistant prostate cancer. *Cancer Res* **68:** 6407-6415

Magde D, Elson EL, Webb WW (1974) Fluorescence correlation spectroscopy. II. An experimental realization. *Biopolymers* **13:** 29-61

Mao Z, Bozzella M, Seluanov A, Gorbunova V (2008) Comparison of nonhomologous end joining and homologous recombination in human cells. *DNA Repair (Amst)* **7:** 1765-1771

Marchenko ND, Hanel W, Li D, Becker K, Reich N, Moll UM (2010) Stress-mediated nuclear stabilization of p53 is regulated by ubiquitination and importin-alpha3 binding. *Cell Death Differ* **17:** 255-267

Markova E, Schultz N, Belyaev IY (2007) Kinetics and dose-response of residual 53BP1/gamma-H2AX foci: co-localization, relationship with DSB repair and clonogenic survival. *Int J Radiat Biol* **83:** 319-329

Min J, Zaslavsky A, Fedele G, McLaughlin SK, Reczek EE, De Raedt T, Guney I, Strochlic DE, Macconaill LE, Beroukhim R, Bronson RT, Ryeom S, Hahn WC, Loda M, Cichowski K (2010)

An oncogene-tumor suppressor cascade drives metastatic prostate cancer by coordinately activating Ras and nuclear factor-kappaB. *Nat Med* **16:** 286-294

Mooradian AD, Morley JE, Korenman SG (1987) Biological actions of androgens. *Endocr Rev* **8:** 1-28

Mullan PB, Quinn JE, Harkin DP (2006) The role of BRCA1 in transcriptional regulation and cell cycle control. *Oncogene* **25:** 5854-5863

Oefelein MG, Feng A, Scolieri MJ, Ricchiutti D, Resnick MI (2000) Reassessment of the definition of castrate levels of testosterone: implications for clinical decision making. *Urology* **56:** 1021-1024

Ogier-Denis E, Codogno P (2003) Autophagy: a barrier or an adaptive response to cancer. *Biochim Biophys Acta* **1603:** 113-128

Ossato G, Digman MA, Aiken C, Lukacsovich T, Marsh JL, Gratton E (2010) A two-step path to inclusion formation of huntingtin peptides revealed by number and brightness analysis. *Biophys J* **98:** 3078-3085

Palmer AG, 3rd, Thompson NL (1987) Molecular aggregation characterized by high order autocorrelation in fluorescence correlation spectroscopy. *Biophys J* **52:** 257-270

Patel AG, Sarkaria JN, Kaufmann SH (2011) Nonhomologous end joining drives poly(ADP-ribose) polymerase (PARP) inhibitor lethality in homologous recombination-deficient cells. *Proc Natl Acad Sci U S A* **108:** 3406-3411

Patterson GH, Lippincott-Schwartz J (2002) A photoactivatable GFP for selective photolabeling of proteins and cells. *Science* **297:** 1873-1877

Patterson GH, Lippincott-Schwartz J (2004) Selective photolabeling of proteins using photoactivatable GFP. *Methods* **32:** 445-450

Paull TT, Rogakou EP, Yamazaki V, Kirchgessner CU, Gellert M, Bonner WM (2000) A critical role for histone H2AX in recruitment of repair factors to nuclear foci after DNA damage. *Curr Biol* **10:** 886-895

Pollack A, Zagars GK, Smith LG, Lee JJ, von Eschenbach AC, Antolak JA, Starkschall G, Rosen I (2000) Preliminary results of a randomized radiotherapy dose-escalation study comparing 70 Gy with 78 Gy for prostate cancer. *J Clin Oncol* **18:** 3904-3911

Pollack A, Zagars GK, Starkschall G, Antolak JA, Lee JJ, Huang E, von Eschenbach AC, Kuban DA, Rosen I (2002) Prostate cancer radiation dose response: results of the M. D. Anderson phase III randomized trial. *Int J Radiat Oncol Biol Phys* **53:** 1097-1105

Potter LK, Zager MG, Barton HA (2006) Mathematical model for the androgenic regulation of the prostate in intact and castrated adult male rats. *Am J Physiol Endocrinol Metab* **291:** E952-964

Roche Y, Zhang D, Segers-Nolten GM, Vermeulen W, Wyman C, Sugasawa K, Hoeijmakers J, Otto C (2008) Fluorescence correlation spectroscopy of the binding of nucleotide excision repair protein XPC-hHr23B with DNA substrates. *J Fluoresc* **18:** 987-995

Rogakou EP, Pilch DR, Orr AH, Ivanova VS, Bonner WM (1998) DNA double-stranded breaks induce histone H2AX phosphorylation on serine 139. *J Biol Chem* **273:** 5858-5868

Rosen EM, Fan S, Rockwell S, Goldberg ID (1999) The molecular and cellular basis of radiosensitivity: implications for understanding how normal tissues and tumors respond to therapeutic radiation. *Cancer Invest* **17:** 56-72

Rossow MJ, Sasaki JM, Digman MA, Gratton E (2010) Raster image correlation spectroscopy in live cells. *Nat Protoc* **5:** 1761-1774

Runions J, Brach T, Kuhner S, Hawes C (2006) Photoactivation of GFP reveals protein dynamics within the endoplasmic reticulum membrane. *J Exp Bot* **57:** 43-50

Sadar MD (2011) Small molecule inhibitors targeting the "achilles' heel" of androgen receptor activity. *Cancer Res* **71:** 1208-1213

Saigal CS, Gore JL, Krupski TL, Hanley J, Schonlau M, Litwin MS (2007) Androgen deprivation therapy increases cardiovascular morbidity in men with prostate cancer. *Cancer* **110:** 1493-1500

Scherr DS, Vaughan ED, Jr., Wei J, Chung M, Felsen D, Allbright R, Knudsen BS (1999) BCL-2 and p53 expression in clinically localized prostate cancer predicts response to external beam radiotherapy. *J Urol* **162:** 12-16; discussion 16-17

Schmitz MD, Padula GD, Chun PY, Davis AT (2010) Normalization of prostate specific antigen in patients treated with intensity modulated radiotherapy for clinically localized prostate cancer. *Radiat Oncol* **5:** 80

Schneider M, Barozzi S, Testa I, Faretta M, Diaspro A (2005) Two-photon activation and excitation properties of PA-GFP in the 720-920-nm region. *Biophys J* **89:** 1346-1352

Schultz LB, Chehab NH, Malikzay A, Halazonetis TD (2000) p53 binding protein 1 (53BP1) is an early participant in the cellular response to DNA double-strand breaks. *J Cell Biol* **151:** 1381-1390

Schwille P, Haupts U, Maiti S, Webb WW (1999) Molecular dynamics in living cells observed by fluorescence correlation spectroscopy with one- and two-photon excitation. *Biophys J* **77:** 2251-2265

Senior A, Gerace L (1988) Integral membrane proteins specific to the inner nuclear membrane and associated with the nuclear lamina. *J Cell Biol* **107:** 2029-2036

Seruga B, Tannock IF (2008) Intermittent androgen blockade should be regarded as standard therapy in prostate cancer. *Nat Clin Pract Oncol* **5:** 574-576

Shaner NC, Patterson GH, Davidson MW (2007) Advances in fluorescent protein technology. *J Cell Sci* **120:** 4247-4260

Shaner NC, Steinbach PA, Tsien RY (2005) A guide to choosing fluorescent proteins. *Nat Methods* **2:** 905-909

Shang Y, Myers M, Brown M (2002) Formation of the androgen receptor transcription complex. *Mol Cell* **9:** 601-610

Siegel R, Ward E, Brawley O, Jemal A (2011) Cancer statistics, 2011: the impact of eliminating socioeconomic and racial disparities on premature cancer deaths. *CA Cancer J Clin* **61:** 212-236

Snapp E (2005) Design and use of fluorescent fusion proteins in cell biology. *Curr Protoc Cell Biol* **Chapter 21:** Unit 21 24

So PT, Dong CY, Masters BR, Berland KM (2000) Two-photon excitation fluorescence microscopy. *Annu Rev Biomed Eng* **2:** 399-429

Stanbrough M, Bubley GJ, Ross K, Golub TR, Rubin MA, Penning TM, Febbo PG, Balk SP (2006) Increased expression of genes converting adrenal androgens to testosterone in androgen-independent prostate cancer. *Cancer Res* **66:** 2815-2825

Stephens DJ, Allan VJ (2003) Light microscopy techniques for live cell imaging. *Science* **300:** 82-86

Tang Y, Simoneau AR, Liao WX, Yi G, Hope C, Liu F, Li S, Xie J, Holcombe RF, Jurnak FA, Mercola D, Hoang BH, Zi X (2009) WIF1, a Wnt pathway inhibitor, regulates SKP2 and c-myc expression leading to G1 arrest and growth inhibition of human invasive urinary bladder cancer cells. *Mol Cancer Ther* **8:** 458-468

Thompson CA, Shanafelt TD, Loprinzi CL (2003) Andropause: symptom management for prostate cancer patients treated with hormonal ablation. *Oncologist* **8:** 474-487

Thompson IM, Tangen CM, Paradelo J, Lucia MS, Miller G, Troyer D, Messing E, Forman J, Chin J, Swanson G, Canby-Hagino E, Crawford ED (2009) Adjuvant radiotherapy for pathological T3N0M0 prostate cancer significantly reduces risk of metastases and improves survival: long-term followup of a randomized clinical trial. *J Urol* **181:** 956-962

Thuault S, Tan EJ, Peinado H, Cano A, Heldin CH, Moustakas A (2008) HMGA2 and Smads co-regulate SNAIL1 expression during induction of epithelial-to-mesenchymal transition. *J Biol Chem* **283:** 33437-33446

Tomioka A, Tanaka M, De Velasco MA, Anai S, Takada S, Kushibiki T, Tabata Y, Rosser CJ, Uemura H, Hirao Y (2008) Delivery of PTEN via a novel gene microcapsule sensitizes prostate cancer cells to irradiation. *Mol Cancer Ther* **7:** 1864-1870

van Duijn PW, Trapman J (2006) PI3K/Akt signaling regulates p27(kip1) expression via Skp2 in PC3 and DU145 prostate cancer cells, but is not a major factor in p27(kip1) regulation in LNCaP and PC346 cells. *Prostate* **66:** 749-760

Vorvis C, Markus SM, Lee WL (2008) Photoactivatable GFP tagging cassettes for protein-tracking studies in the budding yeast Saccharomyces cerevisiae. *Yeast* **25:** 651-659

Waltering KK, Helenius MA, Sahu B, Manni V, Linja MJ, Janne OA, Visakorpi T (2009) Increased expression of androgen receptor sensitizes prostate cancer cells to low levels of androgens. *Cancer Res* **69:** 8141-8149

Wang D, Visser NV, Veenhuis M, van der Klei IJ (2003) Physical interactions of the peroxisomal targeting signal 1 receptor pex5p, studied by fluorescence correlation spectroscopy. *J Biol Chem* **278:** 43340-43345

Wang LG, Liu XM, Kreis W, Budman DR (1999) Phosphorylation/dephosphorylation of androgen receptor as a determinant of androgen agonistic or antagonistic activity. *Biochem Biophys Res Commun* **259:** 21-28

Wang Y, Kreisberg JI, Ghosh PM (2007) Cross-talk between the androgen receptor and the phosphatidylinositol 3-kinase/Akt pathway in prostate cancer. *Curr Cancer Drug Targets* **7:** 591-604

Wang Z, Tseng CP, Pong RC, Chen H, McConnell JD, Navone N, Hsieh JT (2002) The mechanism of growth-inhibitory effect of DOC-2/DAB2 in prostate cancer. Characterization of a novel GTPase-activating protein associated with N-terminal domain of DOC-2/DAB2. *J Biol Chem* **277:** 12622-12631

Ward IM, Minn K, Jorda KG, Chen J (2003) Accumulation of checkpoint protein 53BP1 at DNA breaks involves its binding to phosphorylated histone H2AX. *J Biol Chem* **278:** 19579-19582

Wen Y, Hu MC, Makino K, Spohn B, Bartholomeusz G, Yan DH, Hung MC (2000) HER-2/neu promotes androgen-independent survival and growth of prostate cancer cells through the Akt pathway. *Cancer Res* **60:** 6841-6845

Wu CT, Chen WC, Liao SK, Hsu CL, Lee KD, Chen MF (2007) The radiation response of hormone-resistant prostate cancer induced by long-term hormone therapy. *Endocr Relat Cancer* **14:** 633-643

Wu J, Zhang X, Zhang L, Wu CY, Rezaeian AH, Chan CH, Li JM, Wang J, Gao Y, Han F, Jeong YS, Yuan X, Khanna KK, Jin J, Zeng YX, Lin HK (2012) Skp2 E3 ligase integrates ATM activation and homologous recombination repair by ubiquitinating NBS1. *Mol Cell* **46:** 351-361

Xie D, Gore C, Liu J, Pong RC, Mason R, Hao G, Long M, Kabbani W, Yu L, Zhang H, Chen H, Sun X, Boothman DA, Min W, Hsieh JT (2010) Role of DAB2IP in modulating epithelial-to-mesenchymal transition and prostate cancer metastasis. *Proc Natl Acad Sci U S A* **107:** 2485-2490

Xie D, Gore C, Zhou J, Pong RC, Zhang H, Yu L, Vessella RL, Min W, Hsieh JT (2009) DAB2IP coordinates both PI3K-Akt and ASK1 pathways for cell survival and apoptosis. *Proc Natl Acad Sci U S A* **106:** 19878-19883

Yang G, Ayala G, De Marzo A, Tian W, Frolov A, Wheeler TM, Thompson TC, Harper JW (2002) Elevated Skp2 protein expression in human prostate cancer: association with loss of the cyclin-dependent kinase inhibitor p27 and PTEN and with reduced recurrence-free survival. *Clin Cancer Res* **8:** 3419-3426

Yang J, Mani SA, Donaher JL, Ramaswamy S, Itzykson RA, Come C, Savagner P, Gitelman I, Richardson A, Weinberg RA (2004) Twist, a master regulator of morphogenesis, plays an essential role in tumor metastasis. *Cell* **117:** 927-939

Yano M, Toyooka S, Tsukuda K, Dote H, Ouchida M, Hanabata T, Aoe M, Date H, Gazdar AF, Shimizu N (2005) Aberrant promoter methylation of human DAB2 interactive protein (hDAB2IP) gene in lung cancers. *Int J Cancer* **113:** 59-66

Yu L, Tumati V, Tseng SF, Hsu FM, Kim DN, Hong D, Hsieh JT, Jacobs C, Kapur P, Saha D (2012) DAB2IP regulates autophagy in prostate cancer in response to combined treatment of radiation and a DNA-PKcs inhibitor. *Neoplasia* **14:** 1203-1212

Yu YP, Landsittel D, Jing L, Nelson J, Ren B, Liu L, McDonald C, Thomas R, Dhir R, Finkelstein S, Michalopoulos G, Becich M, Luo JH (2004) Gene expression alterations in prostate cancer predicting tumor aggression and preceding development of malignancy. *J Clin Oncol* **22:** 2790-2799

Yu ZK, Gervais JL, Zhang H (1998) Human CUL-1 associates with the SKP1/SKP2 complex and regulates p21(CIP1/WAF1) and cyclin D proteins. *Proc Natl Acad Sci U S A* **95:** 11324-11329

Zhang R, He X, Liu W, Lu M, Hsieh JT, Min W (2003) AIP1 mediates TNF-alpha-induced ASK1 activation by facilitating dissociation of ASK1 from its inhibitor 14-3-3. *J Clin Invest* **111:** 1933-1943

Zhang W, Yang J, Liu Y, Chen X, Yu T, Jia J, Liu C (2009) PR55 alpha, a regulatory subunit of PP2A, specifically regulates PP2A-mediated beta-catenin dephosphorylation. *J Biol Chem* **284:** 22649-22656

Zhou S, Lo WC, Suhalim JL, Digman MA, Gratton E, Nie Q, Lander AD (2012) Free extracellular diffusion creates the Dpp morphogen gradient of the Drosophila wing disc. *Curr Biol* **22:** 668-675

Zilfou JT, Lowe SW (2009) Tumor suppressive functions of p53. *Cold Spring Harb Perspect Biol* **1:** a001883

Zipfel WR, Williams RM, Webb WW (2003) Nonlinear magic: multiphoton microscopy in the biosciences. *Nat Biotechnol* **21:** 1369-1377

Zitzmann M, Nieschlag E (2001) Testosterone levels in healthy men and the relation to behavioural and physical characteristics: facts and constructs. *Eur J Endocrinol* **144:** 183-197

BIOGRAPHICAL INFORMATION

Shu-Fen Tseng was born in Taoyuan, Taiwan. She attended National Tsing Hua Univeristy in Hsinchu, Taiwan during 2001-2003. She received the master degree in Physics from National Tsing Hua Univeristy in June 2003. She then entered the Joint Graduate Program in Bioengineering between University of Texas at Arlington and University of Texas Southwestern Medical Center at Dallas during 2006-2013. She received her PhD in Bioengineering department from the joint program between University of Texas at Arlington and University of Texas Southwestern Medical Center at Dallas in May 2013. She was interested in Biophysical field and she focused on the researches in the DAB2IP function and the vital oncogenic proteins associated with DAB2IP through using a combination of molecular biological techniques and quantitative fluorescence microscopy methods which includes Raster Scan Image Spectroscopy (RICS) and Number and Brightness (N&B).